Two-nucleon transfer in the ^{58}Ni(p,^{3}He)^{56}Co reaction at incident energies of 80, 100 and 120 MeV

by

Johannes Jacobus van Zyl

Dissertation presented for the degree of Doctor of Philosophy in the Faculty of Science at Stellenbosch University

Supervisor: Prof. Anthony A. Cowley

Co-supervisor: Dr. Retief Neveling

December 2012

DECLARATION

By submitting this dissertation electronically, I declare that the entirety of the work contained therein is my own, original work, that I am the sole author thereof (save to the extent explicitly otherwise stated), that reproduction and publication thereof by Stellenbosch University will not infringe any third party rights and that I have not previously in its entirety or in part submitted it for obtaining any qualification.

December 2012

Abstract

The reaction ^{58}Ni($\vec{p}$,^{3}He) to a few low lying states of ^{56}Co has been investigated at three incident energies between 80 and 120 MeV, and for scattering angles from 25° to 60°. Differential cross section and analyzing power measurements are compared with distorted-wave Born approximation (DWBA) calculations in order to investigate the role of a simple one-step, direct two-nucleon transfer mechanism with a zero-range approximation in the observed angular distributions.

This investigation is strongly motivated by pre-equilibrium studies into the emission of light complex clusters after the interaction of polarized protons at incident energies between 100 and 160 MeV. Unlike these earlier inclusive reaction studies, the present project explores the cross section and analyzing power distributions for a few discrete states and the suitability of the zero-range DWBA formalism for the final step in the (p,^{3}He) pickup reaction at these incident energies.

The results strongly support this simple reaction mechanism and the theoretical calculations seem to follow the trends of the data consistently at increasing incident energy. The spectroscopic description of the data is also consistent with the known spin assignments for most of the states. Despite the shortfalls in the optical potentials and especially in the description of the bound state, the simple, simultaneous pickup model is indeed able to account for the angular distributions observed in the measured cross sections and analyzing powers.

Opsomming

Die reaksie ^{58}Ni($\vec{p}$,^{3}He) na diskrete, lae liggende energietoestande van ^{56}Co is ondersoek by drie verskillende invalsenergieë tussen 80 en 100 MeV en verstrooiingshoeke tussen 25° en 60°. Differensiële kansvlak en analiseervermoë metings is gedoen en vergelyk met berekeninge wat van 'n vervormde-golf Born benadering (DBWA) gebruik maak. Die rol van 'n eenvoudige enkel-stap, direkte twee-nukleon optel meganisme, met 'n nul-reikwydte veralgemening, in die waargenome hoekverdelings word ondersoek.

Hierdie navorsing spruit uit vorige voorewewigsreaksie studies waar die interaksie van gepolariseerde protone, met invalsenergieë tussen 100 en 160 MeV, die uitgee van ligte, komplekse bondels tot gevolg het. Die huidige projek ondersoek, anders as in die vorige inklusiewe reaksie studies, die kansvlak en analiseervermoë van 'n paar diskrete toestande en die gepastheid van die nul-reikwydte DWBA formalisme vir die beskrywings van die finale stap in die (p,^{3}He) optel reaksie by hierdie invalsenergieë.

Die berekenige ondersteun streng hierdie reaksie beskrywing en veral die tendense van die data met toenemende invalsenergie. Tot 'n groot mate stem die spektroskopiese passings goed ooreen met die bekende hoekmomentum toekennings vir die meeste van die toestande. Binne die leemtes van onder andere die optiese potensiale en veral onduidelikhede in die beskrywing van die gebonde toestand, is die eenvoudige, gelyktydige optel model inderdaad 'n sinvolle beskrywing van die waargenome hoekverdelings.

Acknowledgments

- To my promoter and friend Prof Anthony Cowley, thank you for your advice, your guidance and support! I appreciate the way in which you treated me as an equal physicist even though I am still very inexperienced. I truly learn something every time we speak.

- To Dr Retief Neveling for your patient guidance, support and hard work to ensure that this project succeeds. Thanks for sticking with me during those long hours at the lab!

- To my colleagues at iThemba LABS and Stellenbosch University, specifically Dr Zinhle Buthelezi, Dr Siegfried Förtsch, Dr Justin Mabiala, Joel Mira, Dr Paul Papka, Dr Ricky Smit, Dr Deon Steyn, Cobus Swartz and Dr Iyabo Usman, who so diligently helped me during the long weekend shifts taking data and managing the experiment, thank you. Without your help this thesis would not be possible.

- To the staff and students at the Physics Department, Stellenbosch University, thank you for your support. Thank you especially to Stanley February, Tinus Botha, Dr Shaun Wyngaardt, Prof Runan de Kock and Dr Anton Stander for your continued friendship and understanding. Anton, thank you for taking the reigns of the first year course while I was writing up this thesis, I owe you one! Thank you also to Heleen Randall for helping me with all my conference arrangements, my course management and finances!

- I thank the Physics Department, Stellenbosch University, for the financial support and for allowing me the time to further my career.

- Thank you to my family and friends for your whole-hearted support and understanding. Thank you especially to my wife Frieda for allowing me the space and long hours of ”absence” to complete this milestone in my life.

O store Gud, när jag den verld beskådar
Som du har skapat med ditt allmaktsord,
Hur der din visdom leder lifvets trådar,
Och alla väsen mättas vid ditt bord;

Då brister själen ut i lofsångsljud:
O store Gud!
O store Gud!

- Carl Gustaf Boberg (1859-1940)

Contents

List of Figures

List of Tables

Chapter 1

Introduction and Motivation

Nuclear reactions involving the emission of light composite ions from target nuclei after being bombarded by polarized protons of medium energy (around 100 MeV) have been studied extensively over the past decade [Cow96, Cow97, Cow07b, Cow10]. These inclusive $(\vec{p}, \alpha)$ and $(\vec{p},{}^3\mathrm{He})$ reactions are considered as being pre-equilibrium processes that are quite successfully interpreted by *statistical multistep* theories like the statistical multistep direct (MSD) model of Feshbach, Kerman and Koonin (FKK) [Fes80].

In the multistep formalism, the final step following a few possible intra-nuclear proton-nucleon collisions is considered to be either an α-particle knockout, as in the case of the (p, α) reaction, or a pickup of a proton-neutron pair, in the case of the $(p,{}^3\mathrm{He})$ reaction. In this context, a one-step $(p,{}^3\mathrm{He})$ process means an immediate pickup of a proton-neutron pair, a two-step reaction proceeds via an initial collision between the incident proton and a nucleon in the target nucleus, followed by a pickup to produce the emitted ^{3}He-particle, written as $(p, p',{}^3\mathrm{He})$. Similarly, in a three-step reaction the incident proton undergoes two inelastic collisions before the final pickup of the proton-neutron pair, i.e. $(p, p', p'',{}^3\mathrm{He})$. The final step, after the multistep stage, is described theoretically in terms of the distorted-wave Born approximation (DWBA).

The results of these studies indicate a strong and sensitive correlation between the

proposed multistep mechanism and the measured spin-observables. In fact, measured observables like analyzing power can be used as a tool to probe the dominant reaction mechanism involved [Spa00]. It must be pointed out that these earlier multistep studies were *inclusive* reaction studies which measured the angular distributions over a large excitation energy region from zero to the maximum for a specific beam energy, and in energy bins of a few MeV. As such, these investigations were not able to identify the influence from separate discrete states to the total analyzing power. The focus of the present project is to investigate the role of the DWBA in the description of the direct pickup process in the $(p,^3\mathrm{He})$ reaction to discrete states at excitation energies below 10 MeV.

1.1 The Direct Reaction

Broadly we can categorize nuclear reactions into two extreme regimes, namely *compound nucleus* formation and *direct reactions* [Sat90]. These are distinguished by the mechanisms involved. During compound nucleus formation the projectile and target join together and share the energy amongst the constituents. With enough energy some particles or clusters of particles can evaporate from the compound system with generally isotropic angular distributions. These are relatively "slow" reactions taking in the order of 10^{-16} s to decay and reach thermal equilibrium.

In direct reactions, on the other hand, the projectile interacts with only individual nucleons or clusters and mostly in the surface (periphery) of the target. These are more glancing interactions that take place in the time it takes the projectile to cross the nuclear diameter, which is $\sim 10^{-22}$ s. Inelastic direct reactions, for example, are very effective in exciting collective states or rotational modes on deformed nuclei. Particle transfer interactions such as $(p,^3\mathrm{He})$ and (p,t) *pickup* reactions or (d,p) *stripping* reactions, and (p,α) *knockout* reactions fall within the realm of direct reactions.

Direct reactions are especially important in the excitation of discrete, low-lying states

of nuclei and can give valuable information on the shell model and shell model wave functions. The excitation of the discrete states in ^{56}Co investigated in the present study is treated as a direct reaction mechanism. Direct reactions generally display cross section angular distributions that are strongly forward peaked and oscillatory in much the same way as optical diffraction patterns. The shape of these distributions very often reveals information about the angular momentum transferred during the interaction [Gle83]. Two-nucleon transfer reactions can give information on pairing correlations, though only relative magnitudes can be modeled reliably, since a full analysis would require the inclusion of sequential processes.

In the gray area between these two extremes are so-called *pre-equilibrium* or pre-compound reactions where particles can be emitted before statistical equilibrium is reached but after the typical direct stage. The *multistep* formalism already mentioned successfully describes reactions in the pre-equilibrium region.

1.2 The Role of the Analyzing Power

The sensitivity of observables like cross section and analyzing power to the reaction mechanism is well-known [Gle83, Bon89]. The shape of the cross section as a function of scattering angle can be related to the specific orbital angular momentum of the residual nuclear state and as such is used frequently as a spectroscopic tool in nuclear structure studies. The availability of analyzing power data from experiments with polarized beams has further sparked investigations into not only nuclear shell structure studies, but also the nature of the reaction mechanism involved. Using polarized protons, the analyzing power, which has a strong total angular momentum dependence [Bro83], has been shown to be very useful when the cross section has a rather smooth, featureless trend seen at increasing incident energies.

An investigation done, for example, by Bonetti *et al.* [Bon89] on the ^{58}Ni(p, α) reac-

tion at 72 MeV used analyzing powers to successfully distinguish whether the reaction involves a triton-pickup or α-knockout, with clear sign differences between the two possible processes, while the cross sections could be explained equally well by both mechanisms. The multistep studies done by Cowley *et al*. [Cow00, Cow07b] pointed out that not only do the angular distributions of the analyzing power reveal the tell-tail signs of the contributions of the different steps, but the differential cross section gives confirmation of the dominant reaction mechanism, as also noted by Hodgson and Běták [Hod03].

Large absolute analyzing power values are thought to be indicative of single-step direct processes seen at the highest emission energies and more forward scattering angles, while higher order steps seem to dominate at the lower emission energies where the excitation is greater and relatively small analyzing powers close to zero are measured. This is because contributions from higher order steps tend to average out the spin characteristics of the incident proton.

Still, accurate experimental analyzing power measurements are sparse. These experiments pose added practical difficulties since it requires polarized beams and the reaction cross sections tend to decrease quite drastically for increasing incident energies [Cow12]. In this present project we present new angular distributions of both the differential cross section and analyzing power for a few discrete, low lying states in the ^{58}Ni($\vec{p}$,^{3}He)^{56}Co reaction. It is hoped that these new measurements, especially the analyzing power, will fill some of the gaps in studies where such spin-dependent data is still lacking, like global optical potential studies which include spin-observables.

1.3 The (p,^{3}He) Reaction

Historically, the usefulness of studying a two-nucleon transfer reaction like (p,^{3}He) as opposed to simpler single nucleon transfer reactions lies firstly in the ability to excite states not easily accessible with only single particles [Gle65], and secondly in the sensitivity

of the angular distributions to the particular orbital angular momentum transferred in the reaction, since the cross section will exhibit coherence between the angular momentum shared by the two-nucleon pair [Gle83].

These reactions therefore provide a strong test of the nuclear wave functions calculated from the nuclear model [Gle83]. However, relatively few studies on $(p,^3\text{He})$ reactions exist as they are inherently difficult because of the low cross sections and complexity of the transferred $JLST$ configurations. Uncertainties in the optical model parameters for ^{3}He-particles aggravate the problem [Bro83].

Evidence exists to support the importance of including other competing processes for a more complete calculation of the cross sections and analyzing powers, like sequential transfer processes [Sat83]. The equivalent sequential pickup for the $(p,^3\text{He})$ reaction would include, for example, the (p,d)-$(d,^3\text{He})$ intermediate steps. It has been shown in (p,t) and (d,α) reactions at low bombarding energies between 15 - 25 MeV [Cok74, Kun81, Iga82] that a coherent sum of the simultaneous and sequential transfer processes can improve the angular distribution fits in a consistent manner. Analyzing power calculations at especially the very forward angles differ significantly for the one-step and two-step calculations, since the different processes may interfere constructively or destructively giving substantially different angular distributions. The analyzing power is therefore a valuable tool in reaction mechanism studies. However, some doubt remains whether including contributions from these higher-order steps are alone the solution for an accurate description of experimental data [Fen80].

The importance of firstly evaluating proper first-order, finite range DWBA calculations which correctly addresses the properties of the nuclear structure cannot be overlooked. It was, for example, shown in reactions such as (p,t) that the cross section is rather sensitive to the form of the triton wave function and correct nuclear overlap functions, which highlights the importance of a correct treatment of the nuclear structure features [Iga82]. We have also seen in $(p,^3\text{He})$ and (p,α) reactions described in terms of a statistical multistep formalism the influence of higher order steps on the analyzing power

angular distributions. At the low excitation energies the one-step process clearly dominates.

A simple direct reaction description remains therefore the first order litmus test for the dominant reaction mechanism and should necessarily bare evidence of competing processes. These known difficulties in the analysis of complex reactions like $(p,^3\mathrm{He})$ further motivate a thorough understanding of the significance of the direct pickup process.

1.4 Aims of this Project

It is the aim of this project to explore the role of the zero-range distorted-wave Born approximation (DWBA) for the $(p,^3\mathrm{He})$ reaction at 80 - 120 MeV incident energies. An analysis of the cross section and analyzing power angular distributions may shed more light on poorly understood features observed in existing inclusive reaction studies due to the complex nature of the reaction.

The studies have shown that there is a strong decrease in the analyzing powers as the incident energy of the projectile is increased. This seems to be in agreement with the multistep model, where one can imagine that the deeper penetration can result in greater excitations and other reaction channels. It is, however, not clear why this decreasing analyzing power trend appears even at the lowest excitation energies, where one would rather expect the more direct, single-step process to dominate the reaction and display higher average analyzing power values [Cow07a]. A possible explanation is that the measured inclusive analyzing power is the fortuitous result of the contributions from different discrete states. It has also been suggested by Cowley *et al.* [Cow10] that this *quenching* of the analyzing power at larger incident energies may be a consequence of the competition between the incident energy dependence of the direct reaction and the multistep mechanism.

To this end we have investigated the low excitation region in the reaction $^{58}\mathrm{Ni}(\vec{p},^3\mathrm{He})^{56}\mathrm{Co}$

experimentally with the aid of a high resolution magnetic spectrometer at incident energies of 80, 100 and 120 MeV. The ^{58}Ni-target was chosen as representative of the mass region of earlier (p,^{3}He) studies, and because of the readily available structure information of the low excited states in ^{56}Co [Bel68, Bru70, Gam80, Nan81, Nan82, Sha84]. Bruge and Leonard [Bru70], for example, has done a similar study on ^{58}Ni at 45 MeV. Experimentally, the ^{58}Ni target is stable and can be produced as a relatively pure solid state target.

Differential cross section and analyzing power angular distributions for a few discrete states have been compared to macroscopic DWBA calculations, treating the (p,^{3}He) reaction as a single-step pickup of a bound proton-neutron pair. Although a one-step pickup may not be the dominant reaction mechanism, as indeed the importance of sequential processes have been reported [Fen80, Kun81, Iga82], albeit dubious, the single-step pickup is necessarily the simplest method if one wishes to investigate the importance of a particular reaction mechanism. Hence we attempt to understand how well the simple two-nucleon pickup description can reproduce experimental angular distributions at medium incident energies. Good agreement, qualitatively or quantitatively, between the experimental angular distributions and such a one-step direct description will help us to understand the importance of the direct process in the more complex multistep reaction.

1.5 Overview of Thesis

The next chapter, Chapter 2, is devoted to the experimental setup at the accelerator facility and explains the techniques and methods used to obtain the experimental data. In Chapter 3 we discuss the data analysis and particle identification methods used to produce the final excitation energy spectra. In Chapter 4 we expound the underlying DWBA formalism that describes the reaction model. We give a brief outline of the numerical code that was used and the key ingredients required, such as the optical potentials. The results of the analysis are presented in Chapter 5 together with the theoretical calculations

fitted to the data. A final set of the ”best” results for the different states are presented in Chapter 6. In the last chapter we summarize the outcomes of this project as it pertains to the initial proposal. The Appendix contains the final experimental cross section and analyzing power values in table form and a few derivations and aspects that needed further elaboration.

Chapter 2

Experimental Details

In order to investigate the differential cross section and analyzing power angular distributions of the low lying energy region at different incident energies, an experiment measuring the (p,^{3}He) reaction on a solid ^{58}Ni target has recently been carried out with the K600 Magnetic Spectrometer at iThemba LABS (Laboratory for Accelerator Based Sciences) near Faure, South Africa. Data were gathered for spectrometer angles of 25°, 30°, 35°, 40°, 45°, 50° and 60° at incident beam energies of 80, 100 and 120 MeV. A weekend of beam time was allocated for each of the incident energies, specifically, the weekend of 1 to 4 October 2010 for the 100 MeV beam, the 80 MeV experiment was conducted between 8 and 11 October 2010, and the 120 MeV experiment was done partially between 10 to 12 June 2011 and 30 September to 3 October 2011. The polarized proton beams were provided by an atomic beam ion source and the degree of polarization was measured throughout the experiment by means of a beam line polarimeter. The reaction products were detected in a focal-plane detector array just after the magnetic spectrometer and identified using standard time-of-flight techniques. The details of each of these experimental elements are discussed further throughout this chapter.

2.1 Accelerator Facility

The main accelerator facility at iThemba LABS hosts two solid pole injector cyclotrons (SPC1 and SPC2) and the main Separated Sector Cyclotron (SSC) capable of accelerating the polarized protons to a maximum kinetic energy of 200 MeV. The layout of the accelerator facility is shown in Figure 2.1. The polarized protons are generated from hy-

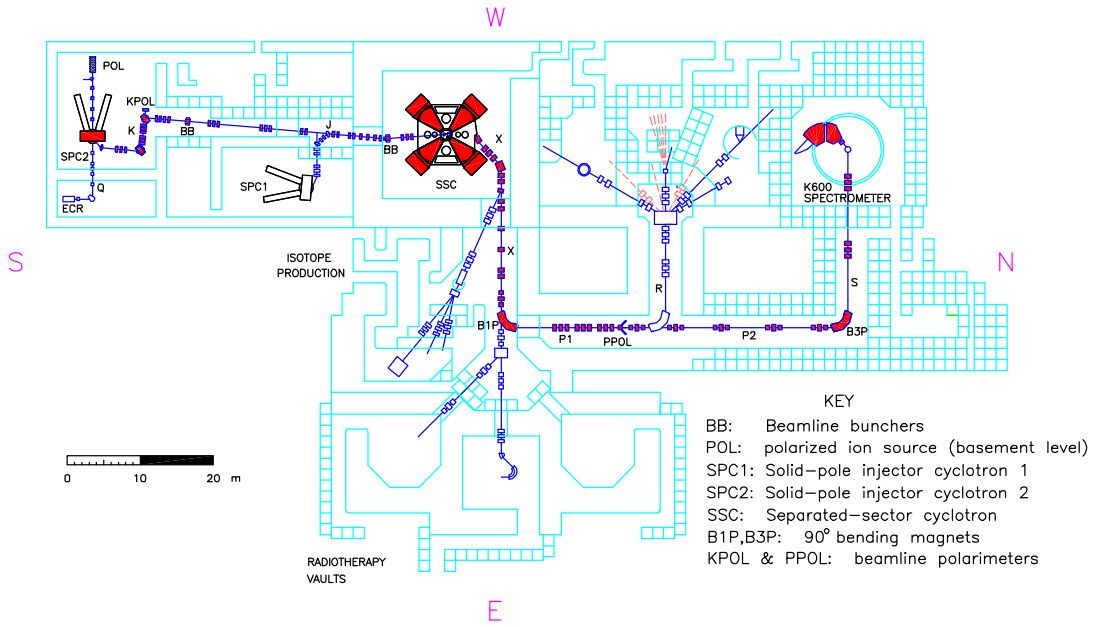

Figure 2.1: Schematic view of the accelerator beam line at iThemba LABS. The ion source is located in the basement level below the labeled SPC2 cyclotron on the far left.

drogen gas in the atomic beam ion source below SPC2, which can supply protons of up to 8 MeV to the SSC. The direction of polarization is switched at the ion source from ”up” to ”down” with respect to the acceleration plane every 10 seconds. This allows for the measurement of the scattering asymmetry between left and right while keeping the detector on one side only. In this context a beam of particles, polarized in the ”up” direction and scattering to the left is equivalent to a beam polarized in the ”down” direction and scattering to the right, i.e. $\sigma^{\uparrow}(\theta_{left}) = \sigma^{\downarrow}(\theta_{right})$.

2.2 Polarization

The degree of beam polarization in the direction normal to the scattering plane was measured regularly throughout the experiment by means of a beam line polarimeter (PPOL in Figure 2.1) located in the P-section of the beam line before the last 90° bending magnet.

At the start of each experimental weekend, as part of the beam setup, the beam polarization was optimized by means of a helium gas polarimeter, the K-line polarimeter, located in the low energy K-line next to the second 90° bending magnet after the SPC2 injector cyclotron (KPOL in Figure 2.1). This polarimeter consists of a helium gas target cell at atmospheric pressure and two 150 μm thick Si detectors mounted at a fixed angle of 110° to the left and right of the incident beam direction. The relatively large ^{4}He$(p,p)^4$He cross section at beam energies below 10 MeV allows for a more effective polarization setup as opposed to the P-line polarimeter.

2.2.1 General Formalism

The scattering plane is largely determined by the polarization direction relative to the beam. For a horizontal scattering plane detector setup, the direction of the polarization vectors of the projectiles are therefore chosen to be perpendicular to the detector scattering plane. Figure 2.2 illustrates the general scattering geometry. Following the recommendations of the Madison convention [Bar71], the positive z-axis is chosen along the incident beam direction and the scattering plane is defined by $\hat{z} \times \hat{z}'$. The polarization direction is then in the $\hat{n}$-direction perpendicular to the scattering plane. The two detectors on the right and left of the beam represents the basic setup of the polarimeters.

The polarization in the up or down direction is determined from the known analyzing power (A_y) for the elastic (p,p) reaction on either ^{12}C or ^{40}Ca (in the case of the P-line polarimeter) or ^{4}He (for the K-line) for a given detector angle, and is defined by

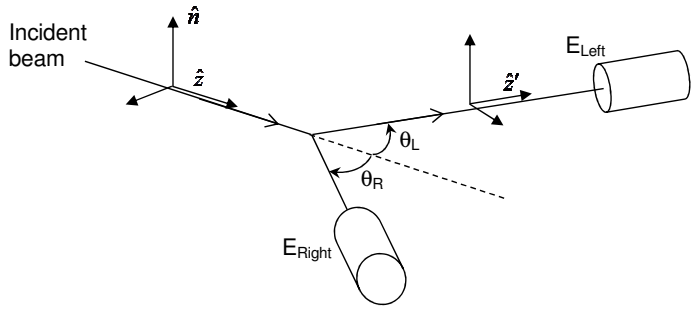

Figure 2.2: Schematic representation of the scattering setup in the polarimeter. The incident beam direction is in the positive $\hat{z}$-direction, and "up" and "down" polarization refers here to the positive and negative $\hat{n}$-direction.

$$p^{\uparrow(\downarrow)} = \left(\frac{1}{A_y}\right) \frac{L^{\uparrow(\downarrow)} \cdot unpol - R^{\uparrow(\downarrow)}}{L^{\uparrow(\downarrow)} \cdot unpol + R^{\uparrow(\downarrow)}}\,, \tag{2.1}$$

where $L^{\uparrow(\downarrow)}$ and $R^{\uparrow(\downarrow)}$ refer to the number of counts in the elastic peak in the left and right detector when the beam polarization was either up ($\uparrow$) or down ($\downarrow$). The $unpol$ factor is the ratio R_{unpol}/L_{unpol} where R_{unpol} and L_{unpol} represent the number of counts in the right and left detector for an unpolarized beam. The factor therefore corrects for the possible asymmetry in the right and left detector setup or beam direction.

The average polarization in the case where $p^{\uparrow} = p^{\downarrow} = p$ is expressed as [Hae74]

$$p = \frac{1}{A_y}\left(\frac{r-1}{r+1}\right) \tag{2.2}$$

with

$$r = \sqrt{\frac{L^{\uparrow}R^{\downarrow}}{L^{\downarrow}R^{\uparrow}}}\,,$$

where A_y is the known (experimental) analyzing power for the specific energy and angle.

The statistical uncertainty associated with the average polarization calculated by (2.2), assuming that the error in A_y is negligible, is given by

$$\frac{\delta p}{p} = \frac{r}{r^2 - 1}\sqrt{\frac{1}{L^{\uparrow}} + \frac{1}{R^{\downarrow}} + \frac{1}{L^{\downarrow}} + \frac{1}{R^{\uparrow}}}\,. \tag{2.3}$$

For the present analysis we assume that the error calculated in (2.3) also applies to $p^{\uparrow}$ and $p^{\downarrow}$ in (2.1).

2.2.2 P-line Polarimeter

At regular intervals during the experiment the beam polarization was measured in the P-line polarimeter. It consists of two similar NaI(Tl) scintillator detectors positioned at equal angles to the left and right of the beam direction. Figure 2.3 shows a schematic view of the polarimeter in the P-line. A list of analyzing power values used for the determination of the beam polarizations is given in Table 2.1.

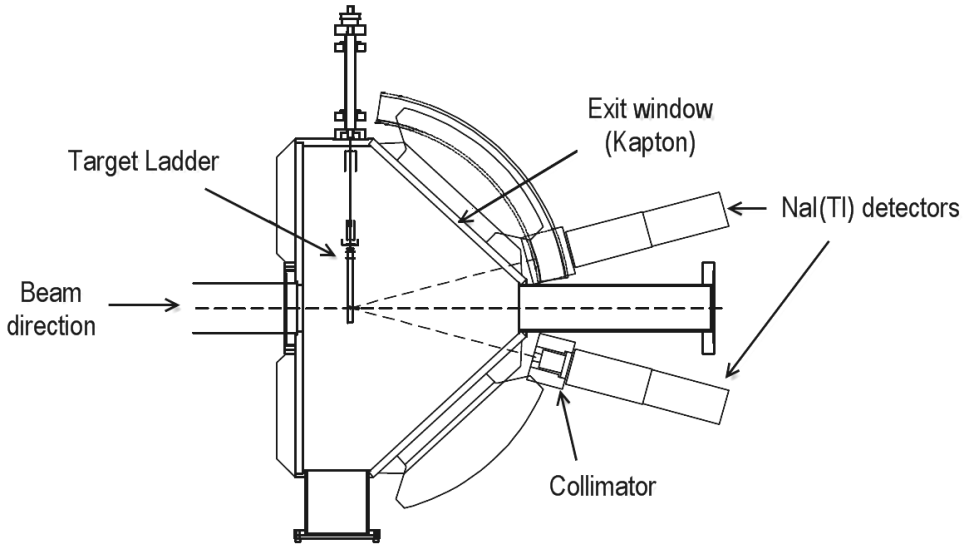

Figure 2.3: Schematic view of the P-line polarimeter consisting of two symmetrical NaI detectors down stream of the target.

E (MeV)	Target	θ_{lab}	A_y	Ref.
80	^{40}Ca	50.3°	0.915	[Sch82]
100	^{12}C	40.0°	0.74	[Cow00]
120	^{12}C	46.3°	0.922	[Mey83]

Table 2.1: Analyzing power values taken from the references used in the determination of the beam polarization for the three incident beam energies. The analyzing power for the 100 MeV beam was determined at iThemba LABS during the (p, α) experiment cited in the reference.

The carbon target used for the polarization measurements during the 100 and 120 MeV experiments is one or two layers of a C_2H_4 polyethylene film (commercial GLAD® Wrap) which contains practically no oxygen as opposed to the otherwise contaminated solid carbon targets. This is important since the ground state of ^{16}O in the ^{16}O(p, p') reaction is very close to the elastic peak of ^{12}C and is not completely resolved by the NaI detectors. The energy spectrum for the ^{12}C$(p, p')^{12}$C reaction, showing the ground and first few excited states of ^{12}C, is given in Figure 2.4.

Polarization values for the three weekends are plotted in Figure 2.5. The average beam polarization was generally between about 65% and 75% with a difference between up and down polarization on average about 15%. The experimental analyzing powers for the $(p,^3$He) study for each scattering angle were calculated from the average of the polarization values taken just before, just after and during the experimental runs.

2.3 The K600 Magnetic Spectrometer

Horizontal spatial separation of ejectiles from different excited states of ^{56}Co is achieved through the use of the high resolution K600 Magnetic Spectrometer at iThemba LABS. The K600 spectrometer is characterized in terms of its magnetic rigidity R which enables this spectrometer to discriminate reaction products with different charge to momentum ratios. This property is discussed in a some more detail in section 2.3.1. A schematic

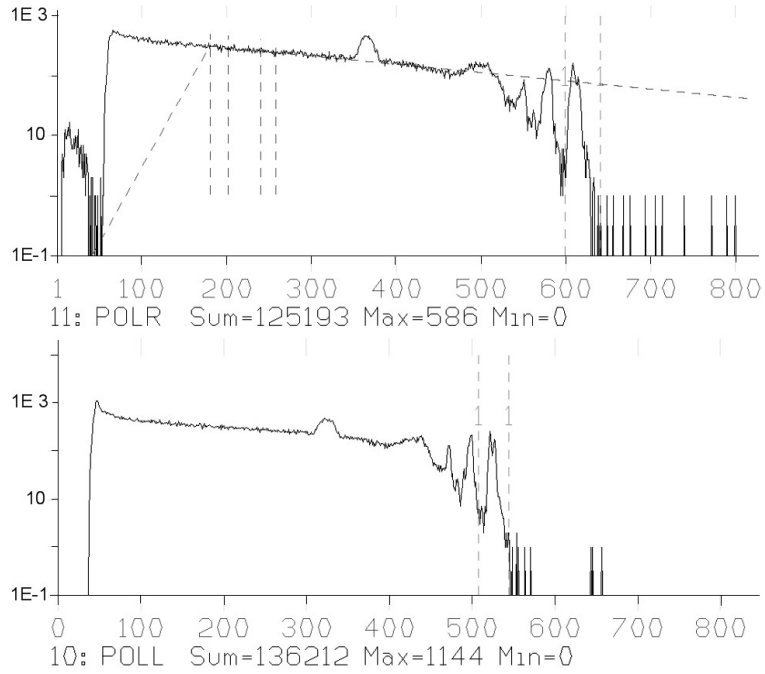

Figure 2.4: Energy spectra for the right (top) and left (bottom) NaI(Tl) detectors in the P-line polarimeter for the reaction ^{12}C$(p, p')^{12}$C for the 100 MeV beam at 40° scattering angle. Visible in the spectra are the three prominent peaks which are the ground state and first two excited states in ^{12}C at 4.4 MeV and 9.64 MeV. The software gate is set around the elastic peak to the very right.

view of the K600 spectrometer can be seen in Figure 2.6

The main spectrometer magnets are the two dipoles D1 and D2, and the quadrupole magnet Q just after the scattering chamber, as seen on the diagram. The Q magnet is used for the focusing of the scattered particles in the vertical direction. Two trim coils, the H- and K-coils, which are pole-face current windings situated inside the dipole magnets, are used for kinematic corrections of reaction products at the focal-plane. Specifically, the K-coil can be used for first-order position corrections as a function of focal-plane angle, so-called $(x|\theta)$ corrections, while the H-coil can correct second-order aberrations, or $(x|\theta^2)$ corrections. The spectrometer can be operated in three possible momentum dispersion modes, a low, medium and high mode. For the present experiment the medium dispersion mode was used which has a momentum acceptance given by P_{max}/P_{min} = 1.097 [Nev09].

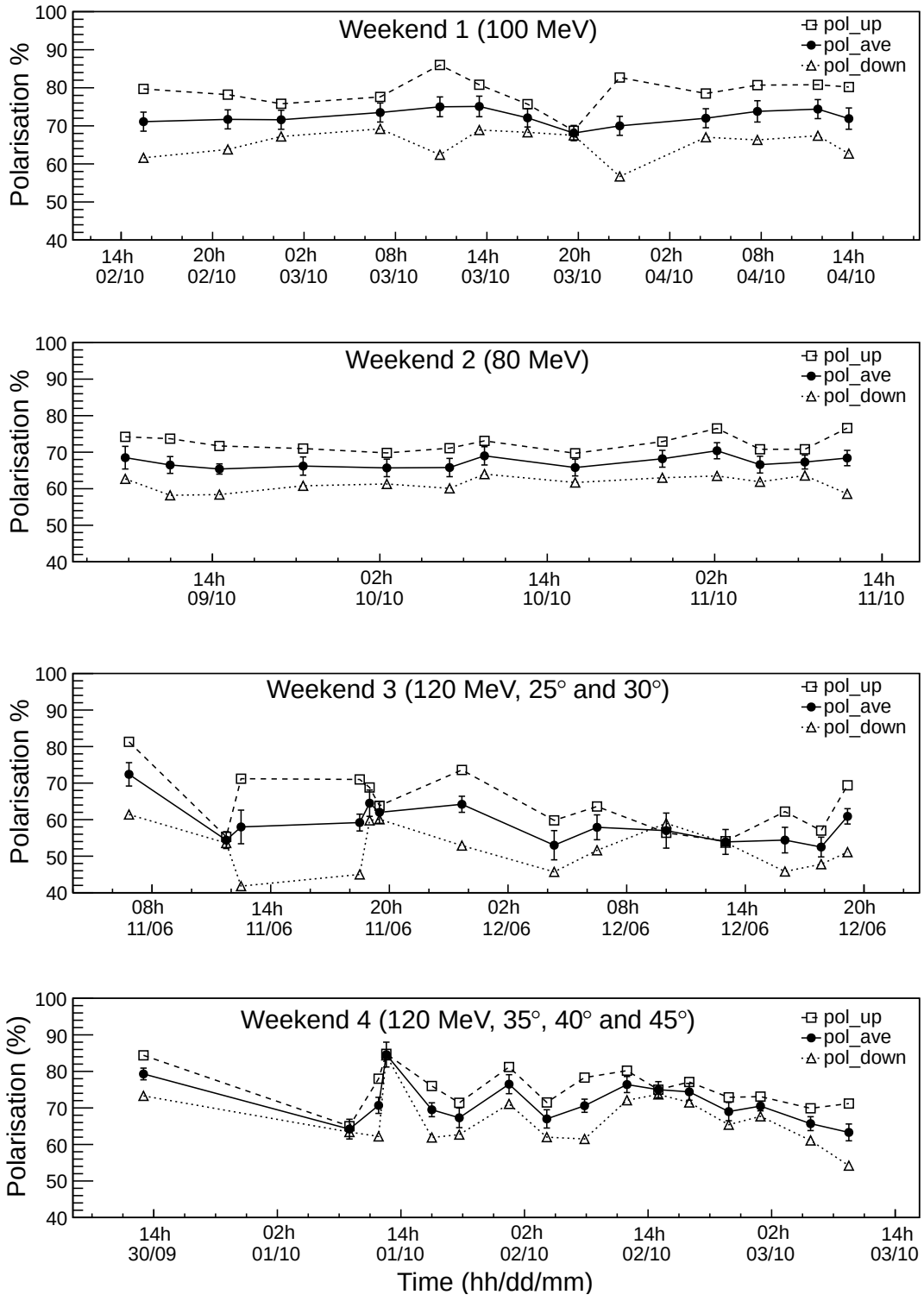

Figure 2.5: Polarization values measured throughout the experimental weekends. Values for weekend 2 were obtained from ^{40}Ca while the rest are from ^{12}C. The graphs show the average (pol_ave), up (pol_up) and down (pol_down) polarizations as discussed in the text.

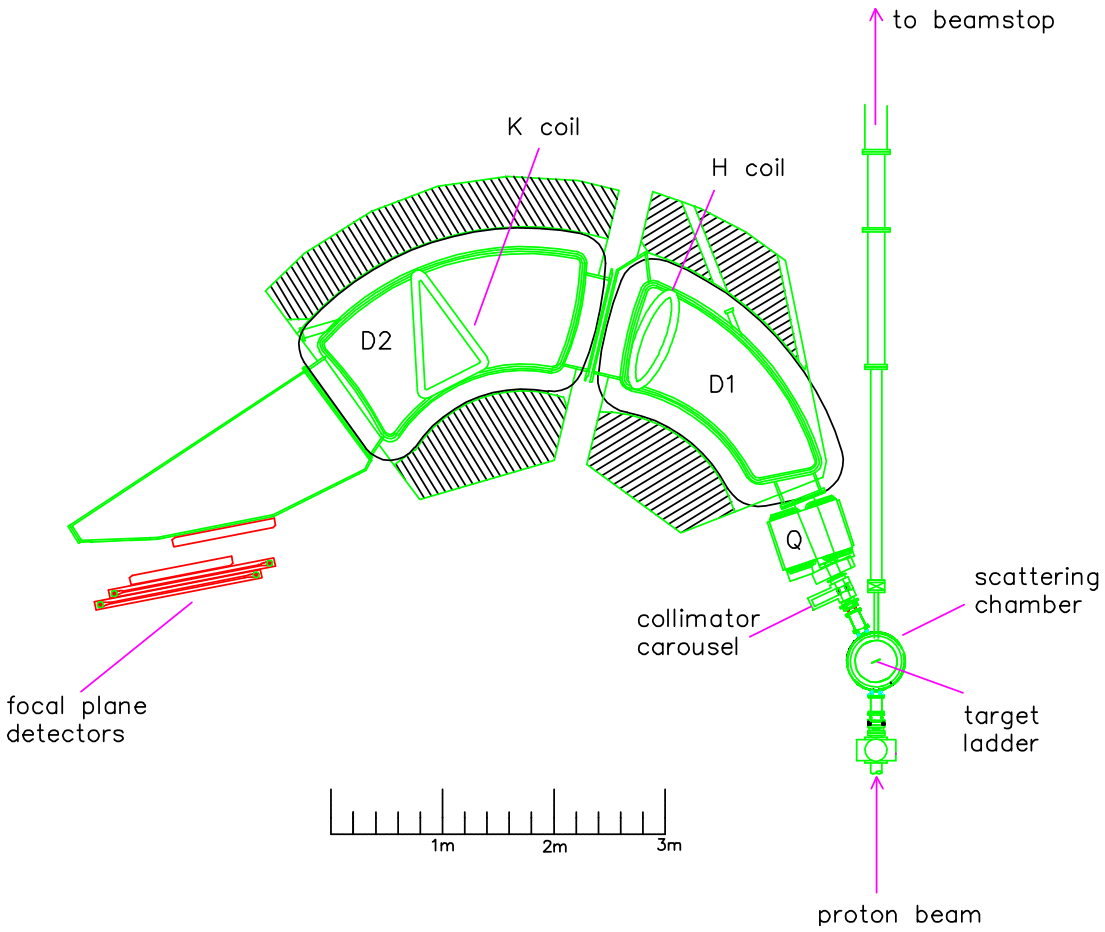

Figure 2.6: Schematic view of the K600 Magnetic Spectrometer at iThemba LABS

Just after the scattering chamber is a collimator carousel for different types of collimators. For the current experiment an 11 mm thick, 49 mm diameter brass collimator ring was used which defined a spectrometer acceptance solid angle of 3.48 msr [Nev09]. A Faraday cup beam stop, situated in the wall of the spectrometer vault, in line with the incident beam, was used during the experiment.

The spectrometer was operated in *dispersion matched* mode to achieve the optimum spatial resolution at the focal-plane. When the spectrometer and beam line is set up in *normal* or *achromatic* mode, emitted particles with a slight momentum dispersion at the target, due to the inherent small energy spread in the incident beam, will have a small horizontal spread at the focal-plane. To compensate for this position broadening, the spec-

trometer is dispersion *matched* with the incident beam line such that the incident beam is defocused at the target so that emitted particles with different momenta are bent through different paths in the spectrometer to reach the same position at the focal-plane [Fuj02].

The spectrometer can be rotated to a horizontal scattering angle of between 23.5° and about 87°, read off from a printed scale on the vault floor. The smallest printed angle increment is 0.1°, but the spectrometer can be positioned manually to within 0.05° of the desired angle.

2.3.1 Magnetic Rigidity

Following closely the notation used by [Swa10], a charged particle entering the magnetic field of the spectrometer with a velocity $\vec{v}$ experiences a force given in terms of its charge q, its velocity and the magnetic field strength $\vec{B}$ as

$$\vec{F} = q\vec{v} \times \vec{B}\,. \tag{2.4}$$

This force will cause a centripetal acceleration, bending the path of the particle through the spectrometer and allows for each species of emitted particles to be discriminated at the focal-plane. Comparing this force with the general formula for a centripetal force gives

$$qvB = \frac{mv^2}{r} \Rightarrow rB = \frac{p}{q}\,, \tag{2.5}$$

where p is the momentum of the particle and r the radius of curvature of the path through the spectrometer. We define the quantity rB as the *magnetic rigidity* R of the particle, i.e.

$$R = \frac{p}{q}\,. \tag{2.6}$$

Taking the non-relativistic expression for the momentum of the particle, $\sqrt{2mE}$, the rigidity can be expressed as

$$R = \frac{\sqrt{2mE}}{q} = \sqrt{2K}\,, \tag{2.7}$$

where K is the energy constant or K-value associated with the particular magnetic spectrometer, given by

$$K = \frac{mE}{q^2}\,, \tag{2.8}$$

where m is measured in atomic mass units, q in units of proton charge and E in MeV.

Different particles with the same rigidity will therefore be bent through the spectrometer to the same position on the focal-plane. These particles may have different masses, charges and energies. The K600 spectrometer at iThemba LABS is specified as having a maximum K-value of 600, i.e. it can measure protons or α particles of up to 600 MeV kinetic energy, deuterons of up to 300 MeV, etc. For the 100 MeV proton beam experiment, for example, the emitted ^{3}He-particles have energies of around 85 MeV for scattering angles above 25°, which corresponds to a K-value of about 65. A few possible, unwanted reaction products with the same K-value of 65, that will also reach the detector focal-plane, are listed in Table 2.2. Assuming the same K-value, the energy is calculated from (2.8) and the relativistic momentum from (3.4). These undesired reaction products can be filtered out according to their times to traverse the spectrometer, also listed in the table.

Particle	Energy (MeV)	Momentum (MeV)	TOF[a] (ns)
^{1}H	62.51	354.09	78.00
^{2}H	32.03	349.64	148.71
^{3}H	21.49	348.81	220.63
^{3}He	85.00	701.62	112.79
^{4}He	64.46	699.32	147.80

[a] Path length of central ray through spectrometer, d = 8.14 m.

Table 2.2: A few unwanted reaction products with the same rigidity (K = 65) as 85 MeV ^{3}He-particles. Note that similar species have similar momenta.

2.3.2 Focal-plane Detectors

Reaction products were detected with a standard focal-plane detector array consisting of a position-sensitive multiwire drift chamber (VDC), referred to as the UX drift chamber, followed by two rectangular plastic scintillators, colloquially referred to as *paddles*, used for event triggering. The focal-plane array is positioned just outside the Kapton exit window of the spectrometer at an angle of 35.75° with respect to a central track through the spectrometer [Nev09].

The UX drift chamber already mentioned above shown in Figure 2.7, consists of two wire-planes. The vertical X wire-plane has 198 earthed signal wires, 20 μm thick and spaced every 4.0 mm, and 199 field-shaping guard wires, 50 μm thick, between every signal wire. A U wire-plane consisting of 143 signal wires and 144 field shaping wires, mounted at an angle of 50° with respect to the vertical and also spaced 4.0 mm apart, is positioned upstream from the X wire-plane. The Au-plated tungsten wires of the X and U wire-planes are positioned between three 20 μm thick negative high voltage aluminum foils, 16.0 mm apart [Nev11].

The drift chamber is filled with a 90% Ar and 10% CO_2 gas mixture at atmospheric preasure and sealed by two 25 μm thick mylar films. Negative high voltages of $\sim$3500 V and $\sim$500 V were applied to the cathode foils and guard wires respectively. Charged particles entering the chambers will ionize the argon gas producing electrons that drift towards the anode signal wires. In the small region very close to the signal wires where the electric field is non-uniform and stronger, an electron avalanche occurs. For a single event, about five to nine wires will record a charge, each with a slightly different time corresponding to the drift distance of the electrons to the nearest wire. By knowing these drift times a particle track can be reconstructed and the accurate position where the particle passed through the focal-plane can be determined. A typical drift time spectrum is shown in Figure 3.8. During the 80 and 100 MeV experiments only one UX drift chamber was used, and for the 120 MeV experiment an older X wire-plane VDC was placed in

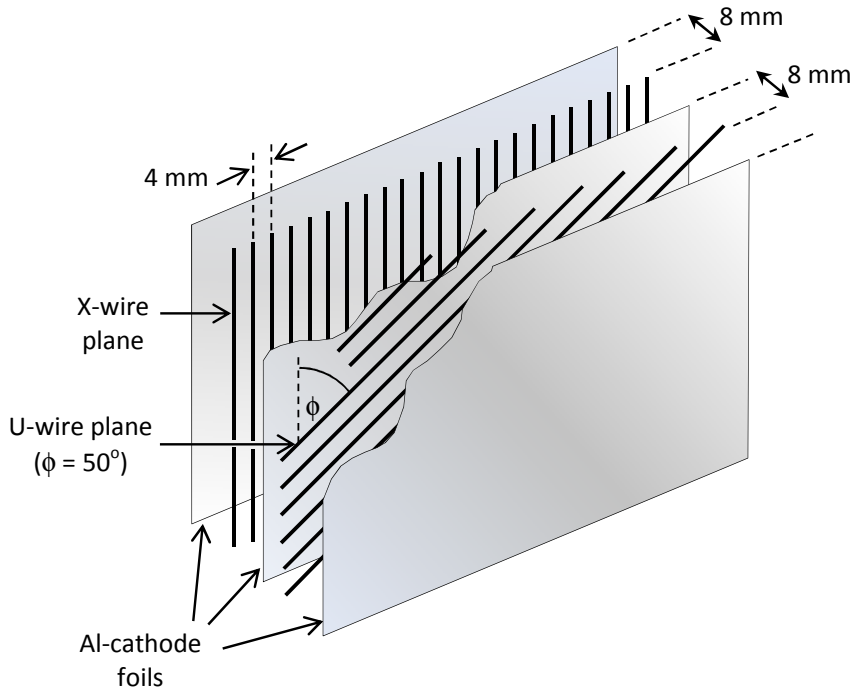

Figure 2.7: A cut-out illustration of the UX position sensitive, multiwire chamber used for focal-plane positioning showing the positioning of the signal wires and Al planes

before the newer UX VDC. A more detailed description of the specifications of the older X drift chamber and more recently constructed UX drift chamber and their operation can be found in [Ber77] and [Fis01, Swa10] respectively.

The two 122 cm $\times$ 10.2 cm plastic scintillator detectors downstream from the drift chamber are 6.35 mm and 12.7 mm thick respectively, and have standard photomultiplier tubes on either side which are operated in coincidence mode. Most of the reaction products are stopped in the first few millimeters of the first paddle, and so the two scintillators were not used as a typical $\Delta E - E$ or $\Delta E - \Delta E$ detector for particle identification. Rather, the energy loss of the particles in the first paddle was used together with time-of-flight (TOF) measurements to identify the reaction products.

2.4 Targets

A target ladder with up to six different mounted target foils is positioned at the center of the 0.524 m scattering chamber as indicated on Figure 2.6. The target ladder can be moved up or down to select different target frames, and rotated to adjust the angle between the normal of the targets and the beam direction. At each spectrometer angle θ the target angle was set to $\theta/2$ so that the relative target thickness and consequent focal-plane resolution remain a minimum. The different targets used in the experiment are listed in Table 2.3. Two thicknesses of ^{58}Ni targets were used, the thin target at θ = 25°, since at this angle the cross sections were expected to be highest, while the thick target was used for all the other angles. The ^{58}Ni targets are self-supporting nickel foils enriched to $> 98\%$, with little oxygen contamination and uniformity of better than 2%/mm [For91].

Target	Description	Thickness
^{58}Ni	thin	1.10 ± 0.08 mg cm^{-2}
^{58}Ni	thick	2.5 ± 0.1 mg cm^{-2}
^{27}Al	-	0.819 mg cm^{-2}
^{12}C	-	1.052 mg cm^{-2}
CONH	Aramid	6.0 μm
$C_{10}H_8O_4$	Mylar®	15.0 μm

Table 2.3: Target and calibration foils mounted on the target ladder.

The aluminum, carbon, Aramid and Mylar targets listed in the table were used for calibration purposes as discussed in Section 3.3. Empty frames similar to the ^{58}Ni target frames are used for periodic halo measurements, and a ”viewer”, consisting of a fluorescent ZnS covered aluminum plate is used for beam spot positioning.

2.5 Electronic Setup and Data Acquisition

The processing of signals from the detector array is done with standard NIM (Nuclear Instrumentation Module) modules and a VME (Versa Modula Europe) computer *frontend*. Most of the electronic modules for the spectrometer and detector array are stacked in the spectrometer vault behind iron shielding. The electronic setup of the current integrator, the clock and the linear and logic signals from the polarimeter detectors use standard techniques found, for example, in [For92, Nev01, Van08].

The basic signal logic for the spectrometer detectors is represented by the block diagram in Figure 2.8. Only the signal from paddle 1 was used as event trigger since the ^{3}He-particles did not reach the second paddle. A mean-timer between the signals from the two photomultiplier tubes on either side of each plastic scintillator allows for a single paddle signal that is independent of the actual position of the event in the plastic. This signal is taken as the START signal for the time-of-flight (TOF) measurement, while an RF signal from the accelerator serves as the STOP signal. A TOF Time-to-Digital Converter (TDC) digitizes the time interval between the START and STOP signals. The different beam energies, measured at the B3P bending magnet (see Figure 2.1), provided during the four experimental weekends as well as the calculated accelerator RF periods are given in Table 2.4.

Weekend	Beam energy (MeV)	RF period (ns)
1	100.44	50.854
2	80.22	56.045
3	117.21	47.068
4	118.37	47.068

Table 2.4: The different beam energies and calculated RF periods for the four experimental weekends. The calculated RF periods were provided by [Fou12].

The energy signal from the paddle is digitized by a current integrating Charge-to-

Digital Converter (QDC) after the Linear Fan. Each drift chamber signal wire is connected to a pre-amplifier card mounted on the drift chamber housing, a discriminator and one of the channels of a 128-channel multihit TDC via a 16-channel twisted-pair ribbon cable. The 198 signal wires of the X wire-plane therefore required more than one TDC module, as did the 143 wires of the U wire-plane. Drift times for each wire event are measured from the time difference between the wire TDC signal, used as the start signal, and a delayed common trigger signal from paddle 1, taken as the stop signal. In this way the shorter drift distances have long drift times, and similarly, large drift distances have short drift times, as indicated on Figure 3.8.

A Current Integrator unit (CI) measures the incident beam current at the beam stop. A full-scale CI reading, defined by the *Range* setting on the unit produces a pulse rate of 1 kHz. As an example, a current of I nA at a range setting of R nA gives an event rate of I/R kHz. The current is displayed in the data room during the experiment and the event rate recorded as a scaler count by the data acquisition system for future replay. The total collected charge during a run is used to determine the number of incident protons. An inhibited CI scaler reading, inhibited by a system *busy* signal generated by the QDC, is used to estimate the system dead time. The data acquisition dead time was generally less than 1%.

A VME frontend is used as an interface between the electronics and the data acquisition (DAQ) software. The *online* event-for-event acquisition is done by means of a recently installed network controlled MIDAS (Maximum Integration Data Acquisition System) software package ideal for fast nuclear and particle physics experiments [MID09].

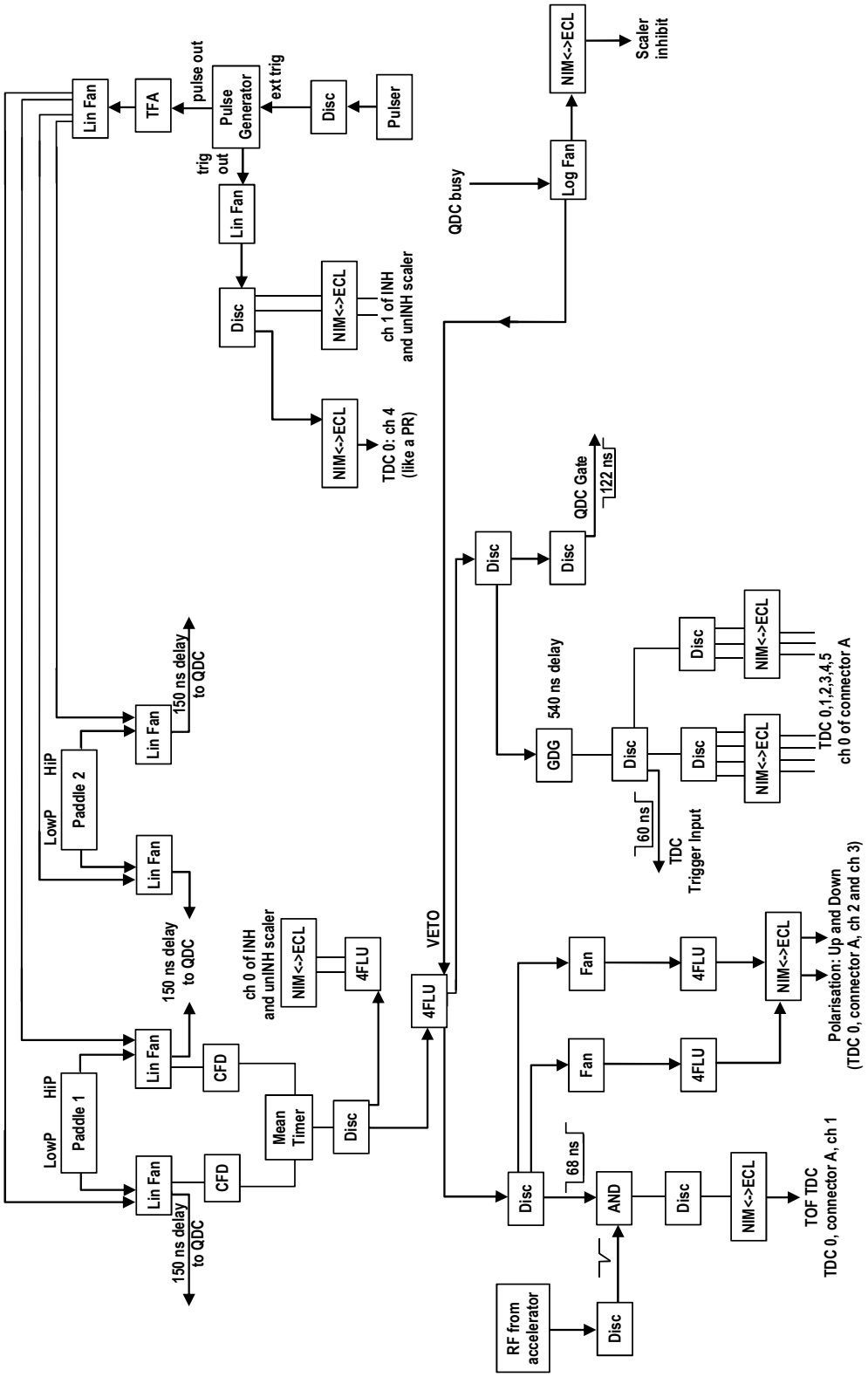

Figure 2.8: Block diagram of the electronic logic of the spectrometer detector array

2.6 Experimental Procedure

Most of the spectrometer electronics have been set up as part of the general operation of the spectrometer and only the spectrometer detector array had to be mounted and connected. At the start of each experimental weekend the spectrometer scattering chamber is pumped down to $\sim 10^{-5}$ mbar. The focal-plane drift chamber gas flow is started and left to clear the detector volume of contaminants, being careful to open the gas lines from the outlet side to avoid over-pressurizing the drift chambers. After a while the high voltage (HV) to the detector array is switched on.

The polarimeter in the P-line had to be set up with detectors, pre-amplifiers and targets. The necessary electronics for the polarimeter and current integrator were set up in the data room before the start of the experiments. Initially, the polarization is measured and optimized by use of the K-line polarimeter. To help align the beam on the target in the K600 vault, a fluorescent *mesh*, colloquially referred to as Hatanaka's mesh [Nev09], mounted 3.1 m up-stream from the target, as well as the ZnS viewer in the target ladder is used. The H- and K-coils are adjusted for the best line shape of the position vs. focal-plane scattering angle. With the ^{58}Ni or ^{12}C target in place, initial (p, p') measurements are made with the appropriate magnet field settings for protons in order to improve the focal-plane resolution by dispersion matching. The procedure involves fine adjustments to quadrupole magnet currents and beam slits along the beam line. Appropriate K600 magnet field settings for protons and helions are calculated beforehand with the code SPEXCIT [DeV09].

With an optimally tuned beam the experimental ^{3}He magnet field settings are set and initial calibration runs can be made. For every spectrometer angle data runs for ^{58}Ni(p,^{3}He) are made for a few hours. At regular intervals of about every two hours a polarization measurements is made in the P-line polarimeter. An unpolarized P-line run is also made to determine the $unpol$ parameter as introduced in Section 2.2. Beam halo is checked regularly by inserting an empty frame as target. The beam halo count rate

was generally below 30 Hz. This relatively large background is mostly due to gammas and protons which were not discarded by the DAQ during the runs, since only paddle 1 was used as event trigger. However, the ^{3}He region in the paddle 1 vs. TOF spectra was sufficiently clean. The maximum beam currents available throughout the experiment was in the order of 10 to 20 nA which corresponded to trigger rates of $\sim$300 Hz.

Chapter 3

Data Analysis

The data accumulated with the MIDAS data acquisition system during the experimental runs were analyzed off-line by means of the C++ based ROOT package developed at CERN [ROO11]. A custom analyzer code converts the raw MIDAS event files to so-called ROOT Trees. During off-line replay the analyzer reads all the stored TDC and QDC channel data, triggers and scalers. It associates wire numbers with TDC channels, fills predefined histograms and calculates, amongst many other necessary parameters, event tracks through the focal-plane.

The initial replay analysis, once the particles of interest are identified, involves setting cable offsets, constructing the lookup table for drift time to drift distance conversion, defining proper focal-plane events and resolution optimization. In the next stage focal-plane calibration and background subtraction can be performed. With clean excitation energy spectra the number of events for a particular transition and scattering angle can be measured and finally used in the calculation of the experimental differential cross section and analyzing power. These steps are discussed in more detail throughout this chapter.

3.1 Particle Identification

3.1.1 Time-of-flight

The ^{3}He-particles are identified from the relative time-of-flight (TOF) measured between the paddle signal and the accelerator RF. The absolute TOF of a particle is calculated in the usual way from its relativistic velocity v and the path length d through the spectrometer, given by

$$t = \frac{d}{v} = \frac{d}{c\sqrt{1 - \left(\frac{m_0c^2}{E+m_0c^2}\right)^2}}, \tag{3.1}$$

where the path length of the central ray d = 8.14 m, E is the kinetic energy of the particle and m_0c^2 its rest mass energy.

The calculated TOF for particles with the same rigidity as the ^{3}He-particles reaching the focal-plane (FP) are given in Table 2.2. Given the time period between particle bundles from the accelerator as shown in Table 2.4, a TOF window can be determined. Corresponding TOF spectra, showing the energy deposited in paddle 1 as a function of the time-of-flight, are presented in Figure 3.1 for the three incident beam energies. Clear loci associated with the different particles can be seen. The ^{3}He-particles are the isolated distributions indicated by the red ellipses. A software gate is drawn around this locus and used to generate ^{3}He-position spectra like the examples in Figure 3.7.

3.1.2 Background

The removal of background was treated in several ways. As mentioned in Section 2.6, the beam halo in the ^{3}He region of the TOF spectra was negligible. Target related background, on the other hand, comprised mostly of high energy protons and gamma rays, and event ”misalignments” in the QDC and TDC registers. These sporadic misalignments resulted in paddle QDC events being registered with unrelated TOF values, and were observed

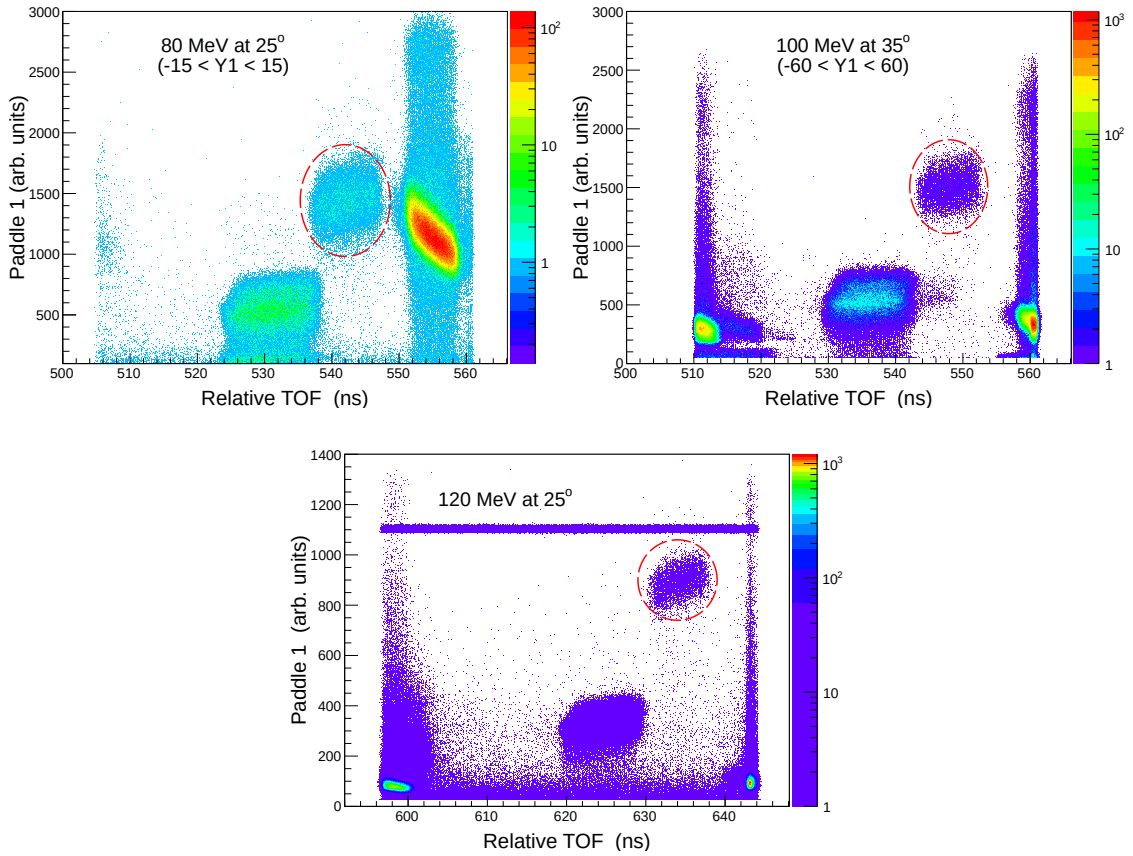

Figure 3.1: Paddle 1 vs. time-of-flight (TOF) spectra for the 80, 100 and 120 MeV beams showing the ^{3}He locus (red dashed ellipse). The two prominent peaks on either end of the spectra represent protons while the central, low energy peak is assumed to be α-particles, consistent with TOF calculations. The horizontal "bar" in the 120 MeV spectrum is from pulser signals. The 80 and 100 MeV spectra also show finer filtering on the vertical focal-plane, Y1.

as paddle events smeared out across the TOF axis, as demonstrated in Figure 3.2. These misaligned events are mostly high energy protons that should all be in the prominent locus on the right of the TOF spectrum between 550 and 560 ns, but instead also contribute to the ^{3}He-particle locus in the TOF spectrum. The misaligned events were removed by identifying a runtime during those problematic runs at which a misalignment first occurred and discarding all events after this runtime.

It appears that the misaligned events are mostly high energy proton events, and so, by selecting the logic condition "paddle 2 $<$ 60", i.e. all events detected in paddle 2, one can

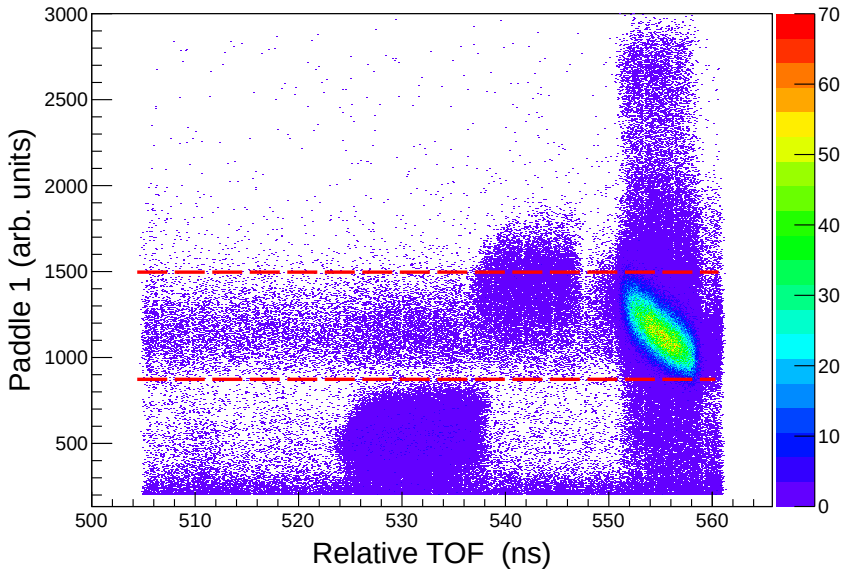

Figure 3.2: TOF spectrum of a few 80 MeV runs at 25° showing the misaligned events as a band across the TOF axis (between the red dashed lines).

further ensure the removal of these unwanted events. A spectrum of paddle 1 vs. paddle 2 is shown in Figure 3.3. High energy events that may trigger both paddle 1 and paddle 2, like protons or gamma rays, can also be removed by this cut on the paddle 1 vs. paddle 2 spectrum, since the ^{3}He reaction products do not reach paddle 2. Figure 3.4 shows those events that are discarded by the above mentioned condition on paddle 2. The effect of this cut is very small since the ^{3}He-particles are cleanly isolated in the TOF spectra, and most of the misaligned events have been taken care of during the run analyses.

Background noise caused by stray scattering and gamma rays can also be identified by inspecting the distribution of events in the vertical focal-plane. Based on the polarization direction the reaction products should largely be restricted to a narrow region in the vertical direction. The K600 quadrupole magnet was used to focus the particles of interest in the vertical direction at the focal-plane, given by the distance Y. A typical spectrum of the distribution of events in the Y-direction is shown in Figure 3.5. The ^{3}He reaction products are sharply centered around Y = 0 in a region between about Y = -20 mm and +20 mm.

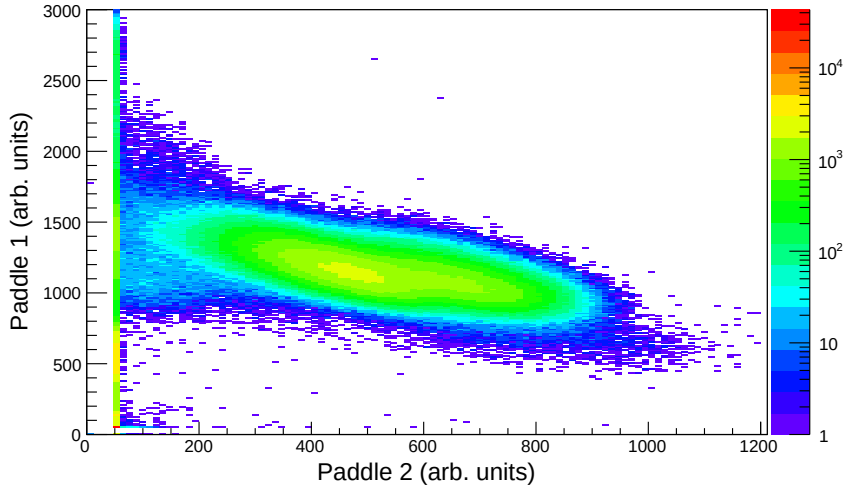

Figure 3.3: Energy spectrum of paddle 1 as a function of paddle 2 for the 80 MeV beam. The prominent locus is mainly from high energy protons.

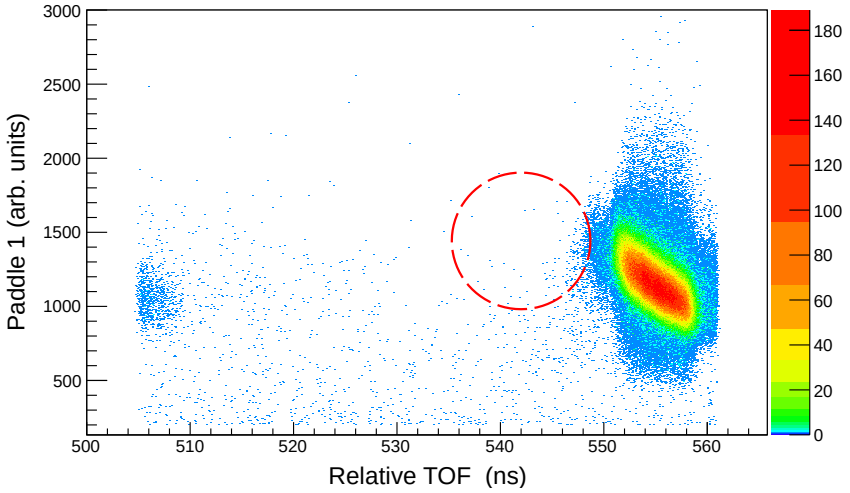

Figure 3.4: Paddle 1 vs. TOF spectrum of the 80 MeV beam at 25° showing the background due to events detected in paddle 2. The red dashed ellipse is where the ^{3}He-locus is.

The resulting TOF vs. FP position spectra for the three beam energies, including the background reduction described above, are given in Figure 3.6, and the corresponding FP position spectra in Figure 3.7. The measured energy resolution for the four weekends, largely limited by the energy loss of ^{3}He-particles in the 1.1 and 2.5 mg cm^{-2} thick ^{58}Ni targets, are listed in Table 3.1.

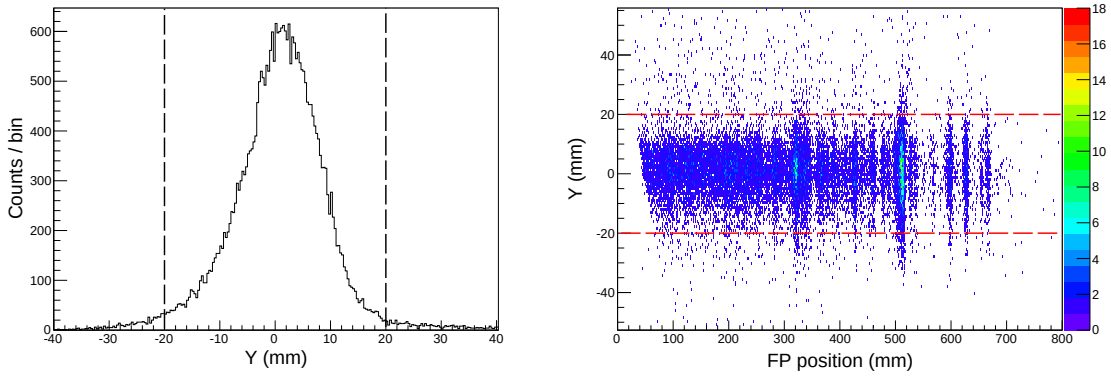

Figure 3.5: Typical spectrum of events in the vertical (Y) focal-plane (left), and a 2D spectrum of Y as a function of the horizontal position X for the 80 MeV beam at 25°. Most of the valid reaction events are concentrated between -20 and +20 mm.

Beam energy (MeV)	Angle	FWHM (mm)	keV/mm	Resolution (keV)	E_{loss} (MeV)
80	25°	5.2	14.7	76.0	70.8
100	25°	4.0	19.1	76.3	57.8
120	25°	2.4	23.2	54.5	49.8
120	35°	4.0	23.2	92.7	113.9

Table 3.1: The measured FP position resolution for the four experimental weekends at the respective beam energies. The thin (1.1 mg cm^{-2}) target was used primarily for the 25° scattering angle. The energy loss values (E_{loss}) were calculated from stopping power tables generated by the code SRIM [Zie10].

3.2 Focal-Plane Position

The position of a reaction event in the focal-plane is determined from the measured drift times, which are converted to distances for each wire triggered. For accurate time measurements it is firstly necessary to correct for possible delays in wire signals due to slight differences in cable lengths and electrical impedances.

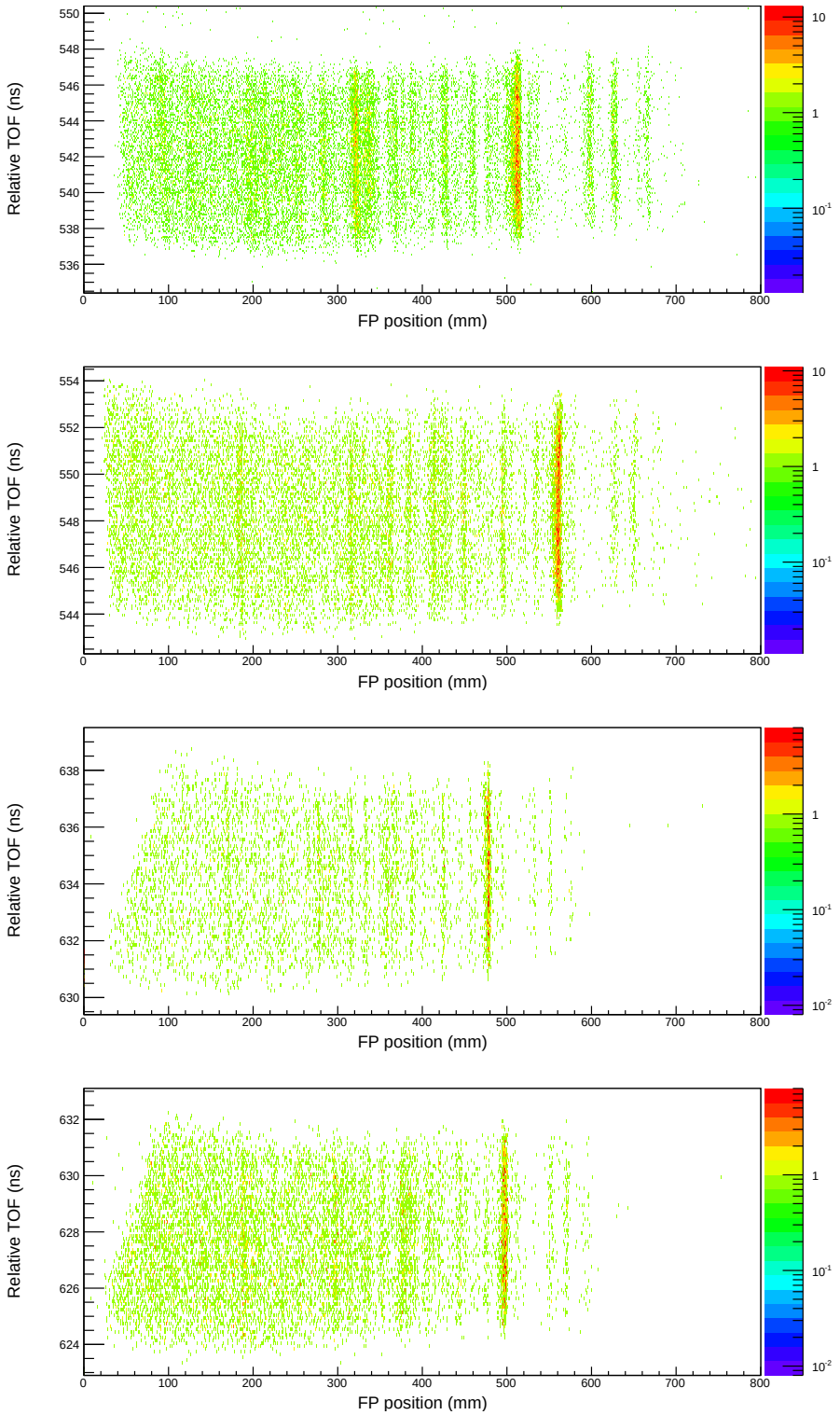

Figure 3.6: The final TOF vs. FP position spectra for the 80, 100 and two 120 MeV beam weekends (from top to bottom). The plots are for the $(p,^3\mathrm{He})$ reactions on ^{58}Ni. The first three plots from the top are for a 25° scattering angle, and the last plot for 35°.

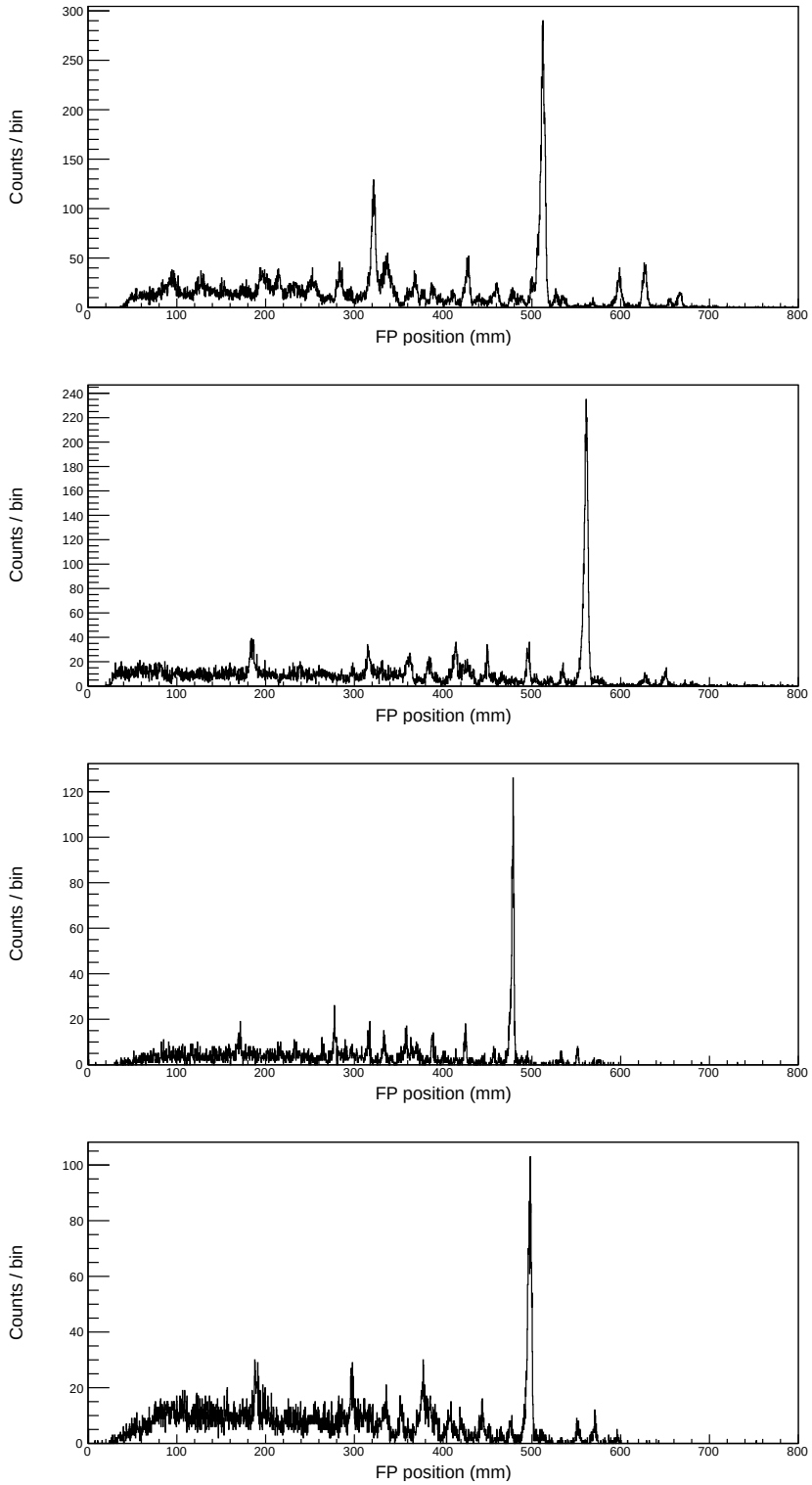

Figure 3.7: The final FP position spectra for the 80, 100 and two 120 MeV beam weekends (from top to bottom). The plots are for the (p,^{3}He) reactions on ^{58}Ni. The first three plots from the top are for a 25° scattering angle, and the last plot for 35°.

3.2.1 TDC Channel Offsets

A drift time spectrum for a typical TDC channel is shown in Figure 3.8. The large peak on the right is associated with very short drift times of cascading electrons close to the signal wire, as mentioned in Section 2.5. The time instant where the slope on the right side of this large peak is at a minimum is used as marker to align each TDC channel to some common reference by introducing an offset for each channel.

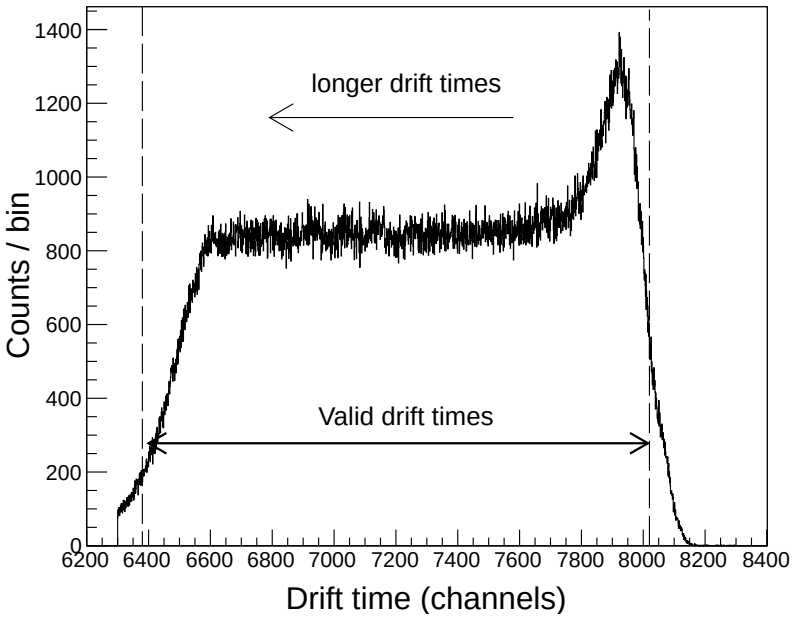

Figure 3.8: Drift time spectrum for X wire-plane showing proper drift times.

The corrected offset time spectrum for one of the TDC's assigned to the X wire-plane is given in Figure 3.9. The alignment of the TDC channels can be done visually, but to ensure consistency a subroutine was written which determines the minimum gradient of the peak on the short drift time side of the spectra in Figure 3.8 and calculates the necessary offset.

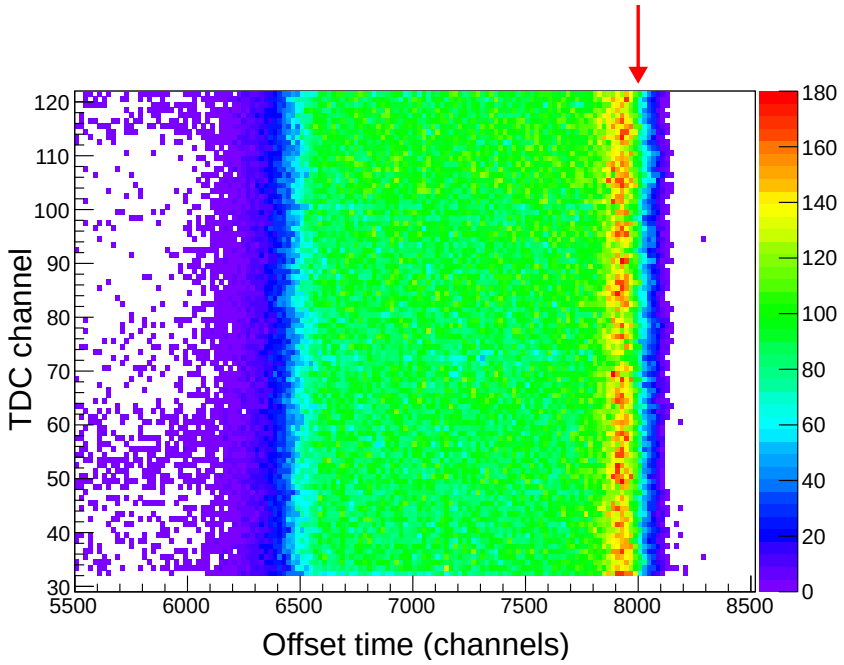

Figure 3.9: Drift time spectrum for one of the TDC's of the X wire-plane. The red arrow indicates the slopes which guides the alignment.

3.2.2 Lookup Table

Once the offsets have been set a lookup table (LUT) is generated which is used to determine the drift distance corresponding to drift time. An example of such a lookup table is given in Figure 3.10. The lookup table depicted in the figure is generated by integrating the drift times according to the integral-time-spectrum method discussed in [Ber77, Nev01] and references therein.

The determination of the exact position of an event in the focal-plane is done in the subroutine f-plane.c, and a more complete description can be found in references like [Nev01, Swa10]. A diagram of the wire-plane showing the nearest wires triggered by the passing of the particle through the focal-plane is given Figure 3.11. The distances x_i for wire i are measured from the actual point where the particle track intersects the wire-plane. A proper or *valid* focal-plane event is one which adheres to the following criteria:

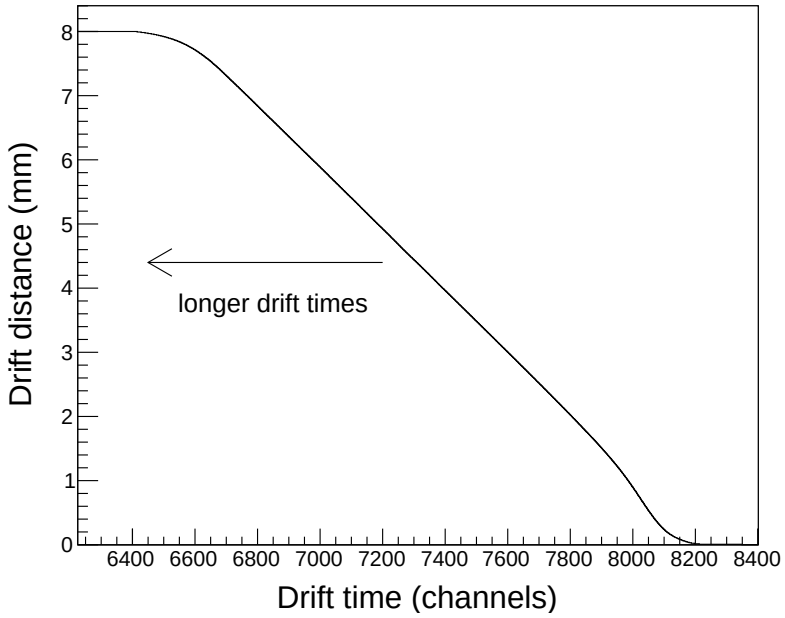

Figure 3.10: A typical lookup table relating drift times with drift distances.

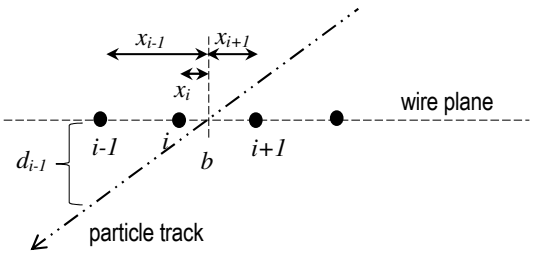

Figure 3.11: Diagram depicting the wires in the focal-plane which are triggered for a proper event.

- coincidence between signal from paddle 1 and wire chamber event,
- less that 9 wires and at least three consecutive wires fired or any three in a group of four consecutive wires,
- for practical drift distances less than 8 mm, the drift times must be within the proper range specified by the gate in the drift time spectra for each TDC channel as shown in Figure 3.8.

3.2.3 Wire-plane Position Resolution

A measure of the accuracy of the drift distances can be deduced from the position resolution, depicted by the symbol Δ, calculated as

$$\Delta = \frac{|d_{i+1} - d_{i-1}|}{2} - d_i \,, \tag{3.2}$$

where d_i is the drift distance for wire i. Ideally it should be sharply centered around zero. The measured resolution can be optimized by adjusting the global shift in the lookup table. An example of the position resolution Δ is give in Figure 3.12 on the left and the 2D resolution plot of Δ as a function of $(b - integer(b))$ on the right, where b is the actual position on the wire-plane where the particle passed through, and $integer(b)$ is the nearest signal wire position. For optimum resolution the distribution should be sharply centered around Δ = 0 as in the figure.

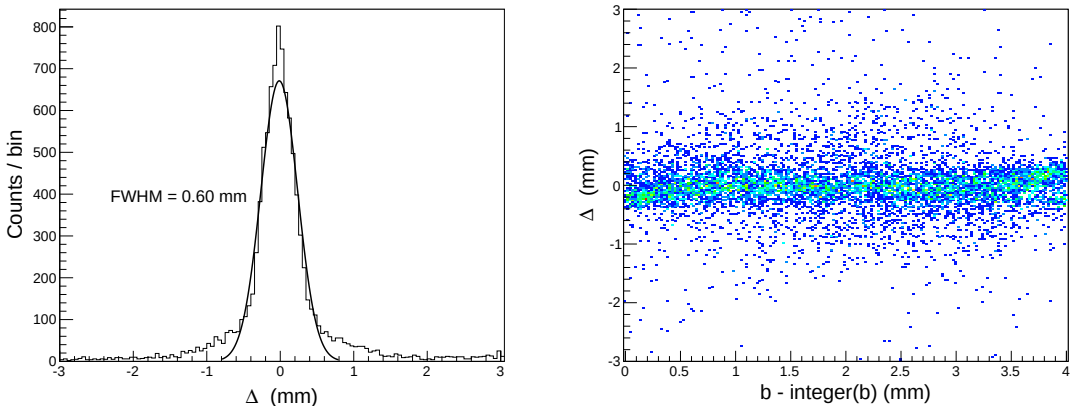

Figure 3.12: Position resolution plot of Δ (left) with FWHM indicated, and a 2D spectrum (right) of Δ vs. $(b - integer(b))$ for ^{3}He particles.

The efficiency ϵ of a drift chamber to detect incident particles of a particular species is the ratio of the number of valid events to the number of triggered events in the focal-plane [Nev01], i.e.

$$\epsilon = \frac{N_{valid}}{N_{tot}} \,, \tag{3.3}$$

where a *valid* events is defined by a set of criteria in the analyzer subroutine f-plane.c. In this context we assume the plastic scintillation detectors have a 100% efficiency. The U and X wire-planes of the UX drift chamber used in the experiment both had average efficiencies between 92% and 96%.

3.3 Calibration of the Focal-Plane

The horizontal position on the focal-plane (FP) detector is calibrated in terms of momentum using known Q-values for reactions on a few calibration targets, namely Aluminum, Mylar (COH) and Aramid (CONH). The data for the ground and excited states in reactions like ^{27}Al(p,^{3}He)^{25}Mg, ^{16}O(p,^{3}He)^{14}N and ^{12}C(p,^{3}He)^{10}B are summarized in Table 3.2. Energy calibration measurements were performed with the above mentioned calibration targets for the 100 MeV beam experiment at the 25° scattering angle only. The corresponding calibration values for the 80 and 120 MeV beams were determined from the kinematics of the ^{58}Ni(p,^{3}He)^{56}Co reaction.

The momenta of the ^{3}He-particles emitted from the reactions above for an incident energy of 100 MeV and scattering angle of 25° is calculated from the familiar relationship

$$(pc)^2 = (E')^2 + 2E'm_0c^2 \tag{3.4}$$

where E' is the kinetic energy of the emitted ^{3}He-particle at the focal-plane, pc its momentum in MeV and m_0c^2 its rest-mass energy, taken as 2809.44 MeV[1]. The resulting calibration data are listed in Table 3.2. The relationship between the particle momentum and its position on the focal-plane is parameterized by a simple second order polynomial [Nev01], given by

[1] All kinematic calculations were performed with the code CatKIN [Cat05]

$$pc = -8.37 \times 10^{-6} x_{FP}^2 + 0.0894 x_{FP} + 623.5 \tag{3.5}$$

where pc is the momentum (in MeV) and x_{FP} the position on the FP (in mm). This is shown in Figure 3.13. The fitting parameters can then be used to calculate the momenta from the measured FP peak positions of the ^{56}Co states in the ^{58}Ni-target data. With the known momentum spread of the medium dispersion plane of 1.097, the corresponding energy-position calibration for the 100 MeV beam yielded ∼20 keV/mm as in Table 3.1.

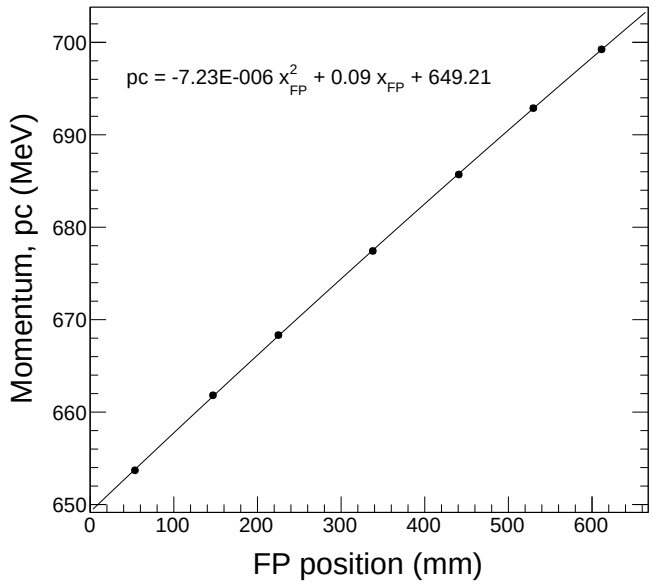

Figure 3.13: Second order polynomial fit of momentum (pc) as a function of focal-plane position (x_{FP}) for several known states of targets like Al, Mylar and Aramid.

The excitation energies (E^*) of the observed ^{56}Co states are calculated from the momentum values determined from (3.5) and the corresponding emission energies (E') using the relativistic kinematics code CatKIN [Cat05]. The results of the calibration of the FP for the ^{58}Ni-target data are summarized in Table 3.3. Based on the uncertainty of the peak centroids on the FP, the calculated excitation energy has an error of ∼40 keV. The results of the present study are compared to the recent nuclear data found in [Fir99] and

Target	Q-value (MeV)	Daughter state (MeV)	FP position (mm)	E' (MeV)	Momentum (MeV)
^{27}Al	-11.65	0.000	611.4	85.71	699.2
		1.612	529.8	84.18	692.9
		3.414	440.7	82.47	685.7
^{16}O	-15.30	0.000	337.9	80.52	677.4
		2.313	225.0	78.40	668.3
		3.948	146.8	76.90	661.8
^{12}C	-19.69	0.000	53.5	75.05	653.7

Table 3.2: Focal-plane (FP) position calibration data for the 100 MeV protons at 25° on different targets. The Q-values for the ^{58}Ni(p,^{3}He)^{56}Co reaction is -11.83 MeV.

that of Bruge and Leonard [Bru70]. We will refer to the ^{56}Co states in the rest of this study according to the energy values quoted by [Fir99]. Figure 3.14 shows the resulting excitation energy spectra of ^{56}Co for the three incident energies, 80, 100 and 120 MeV at 25°. The most prominent nuclear states identified are associated with large orbital angular momentum transfers, expected due to the favourable momentum matching conditions between the projectile and emitted particle.

Not all of the low lying states are clearly resolved. It is often necessary to analyze these peaks further by fitting multiple Gaussian curves in order to get a more accurate centroid position. This is demonstrated by Figure 3.15. The figure shows the region around the strong 2.283 MeV peak for the 100 MeV beam at 25° and 50° scattering angles. Three Gaussian curves are fitted on the peak data to reproduce the compound peak by fixing the centroid positions and the detector resolution, and letting the fitting procedure determine the optimal amplitudes for a best fit.

Ref. [Fir99]		Ref. [Bru70]	This work			
E^* (MeV)	J^π	E^* (MeV)	FP position (mm)	pc (MeV)	E' (MeV)	E^* ($\pm$ 0.04) (MeV)
0	4^+	0.000	679.0	704.4	86.96	0.00
0.15838	3^+	0.166	672.0	703.9	86.83	0.13
0.57650	5^+	0.578	650.0	702.2	86.42	0.55
0.97023	2^+	0.961	629.0	700.6	86.03	0.95
1.00913	5^+	1.001	627.0	700.4	85.99	0.99
2.28263	7^+	2.271	561.5	695.3	84.77	2.24
2.37183	6^+	2.371	558.0	695.0	84.70	2.31
2.456	0^+,1^+	2.456	554.0	694.7	84.62	2.39
2.789	-	2.734	535.0	693.2	84.27	2.75
3.060	5^+	3.048	521.0	692.1	84.00	3.02
3.544	7^+	3.587	496.0	690.2	83.53	3.50
4.441	7^+	4.432	450.0	686.5	82.66	4.39
5.081	-	5.090	414.0	683.6	81.98	5.09
5.187	1^+,2^+,3^+	5.187	407.0	683.1	81.85	5.23

Table 3.3: Focal-plane (FP) calibration for the identified states in ^{56}Co for 100 MeV and 25°.

3.4 Angular Distributions

We determine the number of reaction events for a particular excited state by integrating the selected peak areas in the position spectra for each spectrometer angle. Although many of the peaks could be successfully fitted using a ROOT Gaussian fitting routine, the poor statistics at especially the larger angles made it impossible to determine the peak areas of unresolved states consistently by deconvolution of the multi-peak fits. This is illustrated in Figure 3.15 where the compound peak on the left at 25° is accurately deconvoluted, but not the peak on the right at 50°. Instead, the integral of the whole region containing all three states was measured. When comparing the measurements to the theoretical calculations, we then also add the cross sections of the three constituent states. This is discussed in more detail in Chapter 5.

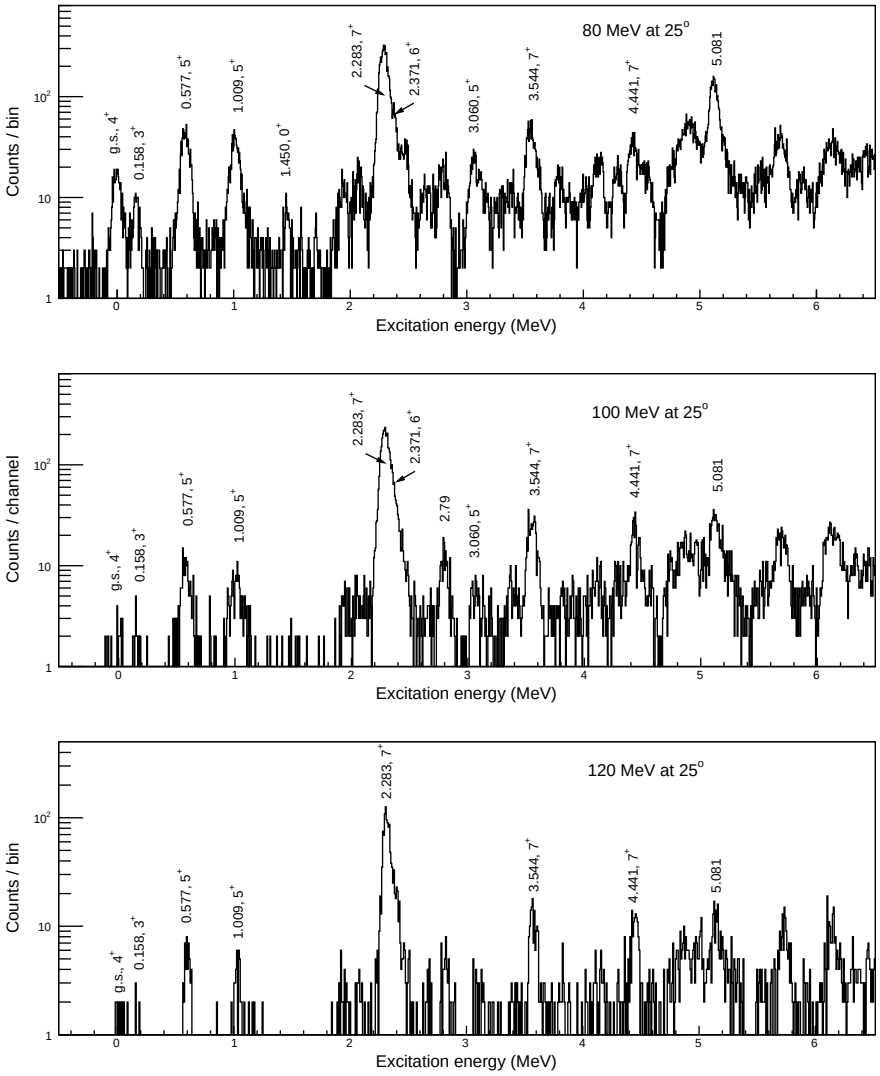

Figure 3.14: Excitation energy spectra for the ^{58}Ni(p,^{3}He)^{56}Co reaction at 25° for the three incident beam energies, 80 (top), 100 (middle) and 120 MeV (bottom) indicating the energies of a few prominent states. Each spectrum represents all the data recorded for this scattering angle.

3.4.1 Differential Cross Section

The measured differential cross section (in mb sr^{-1}) for a specific lab angle θ is determined from

$$\frac{d\sigma(\theta)}{d\Omega} = \left(\frac{10^{27}}{n}\right) \frac{N_c}{\epsilon N_0 \Delta\Omega}\,, \tag{3.6}$$

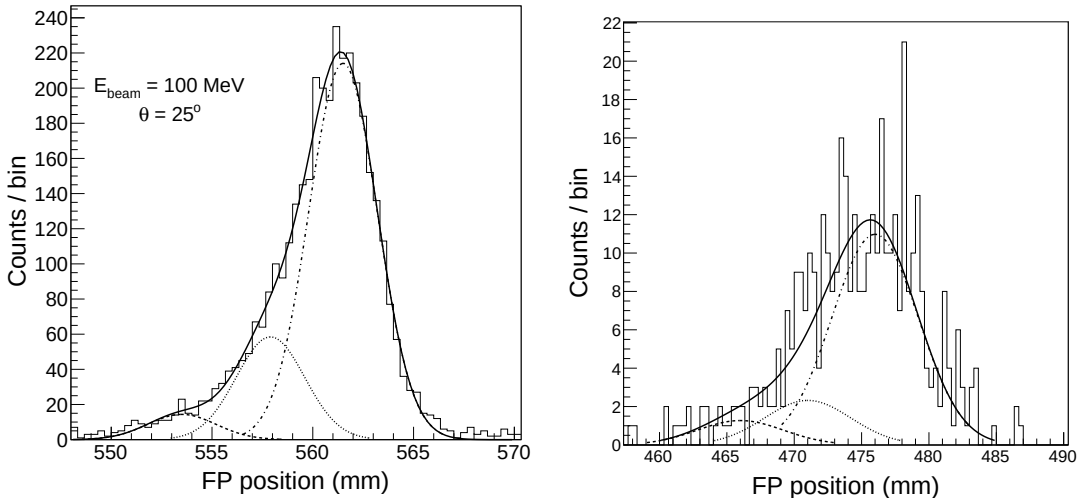

Figure 3.15: Multiple Gaussian peak fit (solid line) on the unresolved 2.283 MeV state showing the 2.456 (dot-dash), 2.372 (dot) and 2.283 MeV (dash) states for 25° (left) and 50° (right). The data are taken from the 100 MeV beam experiment.

where N_c is the background corrected integral counts in an energy peak, ϵ is the VDC detector efficiency, N_0 is the total number of incident protons, $\Delta\Omega$ is the acceptance solid angle of the spectrometer defined by the collimator (in sr), and n is the target nuclear area density.

The total incident flux N_0 is determined from the charge collected on the beam stop and is given by the Current Integrator scaler reading CI, inhibited by the DAQ *busy* signal, as

$$N_0 = \frac{CI \cdot R}{1000 \cdot q_{e^-}}, \tag{3.7}$$

where R is the *Range* setting on the CI unit [in nA] as discussed in Section 2.5. The value q_{e^-} is the electron charge given in nC, i.e. 1.602×10^{-10} nC.

The target area density n is the number of target nuclei per cm^2, and is calculated from

$$n = \frac{N_A \cdot t_\rho}{A \cdot cos(\theta_{tgt})} \,. \tag{3.8}$$

Here N_A is Avogadro's number, t_ρ is the target density-thickness [in g cm^{-2}][2]. The factor A is the atomic mass of the target [in g mol^{-1}], and θ_{tgt} is the angle between the normal to the target and the beam direction.

The *unpolarized* cross section, in the case of a polarized beam, will be compared with the theory in Chapter 5. The unpolarized cross section, as it is derived in Appendix A.1 is

$$\sigma_0 = \frac{\sigma^\uparrow p^\downarrow + \sigma^\downarrow p^\uparrow}{p^\uparrow + p^\downarrow} \,, \tag{3.9}$$

where $\sigma^\uparrow$ and $\sigma^\downarrow$ are calculated from (3.6) with $N_c^{\uparrow(\downarrow)}$ and $N_0^{\uparrow(\downarrow)}$.

By employing the assumption (A.11) in Appendix A.2, the unpolarized cross section for a particular energy state and angle is

$$\sigma_0(\theta) = \left(\frac{2 \cdot 10^{27}}{n}\right) \frac{p^\downarrow N^\uparrow + p^\uparrow N^\downarrow}{\epsilon N_0 \Delta\Omega (p^\uparrow + p^\downarrow)} \,. \tag{3.10}$$

When $p^\uparrow \approx p^\downarrow = p$, this expression reduces again to (3.6).

It was found that the effect on the cross section of introducing this approximation of the polarization was on average less that 2%, and well within the more serious errors from the low count rate and the uncertainty in target thickness. This then was the motivation to estimate the statistical error of the cross section from equation (3.6) or (A.9) instead.

[2]This is equivalent to 10^{27} g mb^{-1}, hence the factor of 10^{27} in the equation, i.e. 1 mb = 10^{27} cm^2.

3.4.2 Analyzing Power

The experimental analyzing power is calculated from relation (A.4) in Appendix A.1. In terms of the number of counts in the energy peaks when the beam is polarized in the up or down directions, and making the assumptions discussed in Appendix A.2, the experimental analyzing power is calculated from

$$A_y = \frac{N^{\uparrow} - N^{\downarrow}}{p^{\downarrow}N^{\uparrow} + p^{\uparrow}N^{\downarrow}}\,, \tag{3.11}$$

where the common factors have canceled to first order.

In general the data from many runs are chained together so that N is in fact $\sum_i N_i$. For some angles the various runs had different values for the target thickness, target angle and CI range. This then complicates the chaining process to some extent. The correct method of determining the observables is outlined in a bit more detail in Appendix A.2 and A.3.

3.5 Error Estimation

3.5.1 Systematic Errors

Systematic uncertainties in the cross section calculations are mainly from uncertainties in the target thickness, target angle and collimator solid angle. These are estimated at 5%, 1% and 0.5% respectively. The combined systematic error from these main contributors in the calculation of the cross section amounts to $\sim$5.1% when added in quadrature. In the analyzing power calculations, due to the formalism, these systematic factors cancel to first order.

3.5.2 Angular Uncertainty

The estimated error in the offset of the incident beam direction, based on the positioning of the beam on Hatanaka's mesh and the viewer in the target ladder, is at most $\sim 0.04^\circ$. The maximum error in the spectrometer angle is less than 0.05°, taken as half of the smallest 0.1° division on the angle scale. The total uncertainty associated with the scattering angle is then at most $\sim 0.06^\circ$.

3.5.3 Statistical Uncertainties

The largest contributor to the experimental error is the uncertainty in the number of counts recorded per excited state, taken as one standard deviation, i.e. the statistical error. At the low beam energies and small scattering angles the reaction cross sections are relatively large compared to the high incident energy and large angle data where the cross sections drop almost two orders of magnitude. At these low statistical yields the error is enhanced by factors like degrading peak position resolution and remnant background events not removed by PID methods. Though the statistical errors in the cross section measurements are appreciably low, they are amplified in the analyzing power values, since the yields are divided amongst the spin-up and spin-down cases.

We use standard error propagation methods [Kno89] described in Appendix A.3 where we consider the number of counts in each peak N to be a single measurement with one standard deviation given by $\sigma = \sqrt{N}$.

The statistical errors in the measured polarization values were generally about 2%. The uncertainty in the average polarization for each scattering angle is generally less than 7%. The contribution of this uncertainty to the error in the analyzing power is also within that range and is therefore not the leading cause of uncertainty in the analyzing power values. The number of counts in the energy peaks for either up or down polarization was generally between a few hundered for the low cross section states, and in the order of a

few thousand for the highest transition states. (This corresponds to a statistical uncertainty in the number of counts of between 1% and 10%.)

The total statistical error associated with the measured differential cross section of (3.6), from the error propagation methods discussed in Appendix A.3, is

$$\delta_\sigma = \sigma \sqrt{\left(\frac{B_{err}^2}{B}\right)^2 + \frac{1}{N}}\,, \tag{3.12}$$

where the B values represent factors with significant errors given by B_{err}, as discussed in Appendix A.3.1.

By far the largest contributor to the uncertainty in the analyzing power is the number of counts $N^{\uparrow(\downarrow)}$. From the derivation in Appendix A.3.2, the total statistical error in the measured analyzing power of (3.11) is

$$\delta_{A_y} = \frac{\sqrt{N^\uparrow \left(A_y p^\downarrow + 1\right)^2 + N^\downarrow \left(A_y p^\uparrow - 1\right)^2}}{\left(N^\uparrow p^\downarrow + N^\downarrow p^\uparrow\right)}\,. \tag{3.13}$$

where the error in the polarization vanishes, since it is contained in terms such as $\left(p_{err} \cdot A_y\right)^2$ which can be neglected.

Chapter 4

Theoretical Formalism

In this chapter a description is given of the theoretical model adopted to describe the present experimental measurements. We assume that the (p,^{3}He) reaction is a direct two-nucleon transfer reaction as depicted in Figure 4.1, where the projectile a picks up a proton-neutron pair or cluster x in a single step. Such a process is described by the distorted-wave Born approximation (DWBA). A computer code such as DWUCK4 [Kun93], which employs the DWBA formalism with a zero-range interaction potential between the projectile and the two-nucleon cluster, was used to compute the differential cross section and analyzing power.

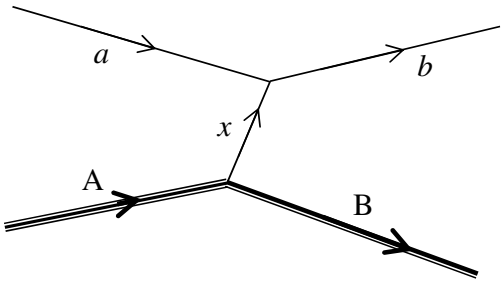

Figure 4.1: Schematic representation of the pickup reaction mechanism.

Let us define the general reaction $a + A \rightarrow B + b$, for a projectile a incident on a target

nucleus A by the expression where, for a pickup reaction, $A = B+x$, and x represents the transferred nucleon pair or cluster. The outgoing particle becomes $b = a+x$ as illustrated.

$$\underbrace{A(a}_{\alpha},\ \underbrace{b)B}_{\beta} \tag{4.1}$$

4.1 Distorted-Wave Born Approximation

In the distorted-wave Born approximation (DWBA) elastic scattering is assumed to be the dominant interaction process [Sat90]. Other reactions such as slight rearrangements or excitations are considered as comparatively weak, and are then treated as perturbations. In this sense in the DWBA the reaction proceeds directly from the initial to the final reaction channel and neglects any intermediate excitations [Gle83].

The *distorted waves* are modified by elastic scattering and its accompanying absorption effects, and are generated from complex optical model potentials. These optical potentials are usually derived from experimental elastic scattering data and are therefore ideal for such a formalism.

4.1.1 Derivation of the Cross Section

The general form of the transition amplitude $\mathbf{T}_{\beta\alpha}$ describing the interaction from the entrance channel α to the exit channel β is given by

$$\mathbf{T}_{\beta\alpha} = \left\langle e^{i\vec{k}'_\alpha\cdot\vec{r}_\alpha} \left| U_\alpha \right| \chi_\alpha^{(+)} \right\rangle \delta_{\alpha\beta} + \left\langle \chi_\beta^{(-)} \Phi_\beta \left| V_\beta - U_\beta \right| \Psi_\alpha^{(+)} \right\rangle , \tag{4.2}$$

the so-called Gell-Mann-Goldberger transformation [Gle83]. The exact solution to the many-body interaction problem Ψ_α, containing all the processes, is not accessible, but can be approximated by $\Psi_\alpha^{(+)} \cong \Phi_\alpha \chi_\alpha^{(+)}(\vec{k}_\alpha \cdot \vec{r}_\alpha)$ which describes the motion of the entrance channel in the influence of an optical potential U_α.

The DWBA then retains only the non-elastic term of the transition amplitude and so reduces to

$$\mathbf{T}_{\beta\alpha}^{DWBA} = \left\langle \chi_{\beta}^{(-)} \Phi_{\beta} \left| V_{\beta} - U_{\beta} \right| \Phi_{\alpha} \chi_{\alpha}^{(+)} \right\rangle , \tag{4.3}$$

where V is the interaction potential between nuclei A and B, U is the optical potential which generates the distorted waves, χ_{α} and χ_{β} respectively, and depends only on the relative motion in the entrance and exit channels. As such, the optical potentials are chosen to describe elastic scattering including absorption correctly, and is therefore complex. The functions Φ_{α} and Φ_{β} are the nuclear wave functions describing the internal motion of A and B and are functions only of the intrinsic coordinates.

At large distances from the scattering center, the distorted waves have the form

$$\chi_{\beta}(\vec{r}_{\beta}) \sim e^{i\vec{k}_{\alpha}\cdot\vec{r}_{\alpha}}\delta_{\alpha\beta} + f_{\alpha\beta}(\hat{k}_{\beta}, \vec{k}_{\alpha})\frac{1}{\vec{r}_{\beta}} e^{i\vec{k}_{\beta}r_{\beta}} , \tag{4.4}$$

which describes a plane wave with momentum $\vec{k}_{\alpha}$ in the entrance channel and an outgoing spherical wave with momentum $\vec{k}_{\beta}$ in the exit channel. Herein the function $f_{\alpha\beta}$ is defined as the *scattering amplitude* for the transition $\alpha \rightarrow \beta$ which appears in the general expression for the differential cross section, namely

$$\left(\frac{d\sigma}{d\Omega}\right)_{\beta\alpha} = \frac{\upsilon_{\beta}}{\upsilon_{\alpha}} \left| f_{\alpha\beta}(\vec{k}_{\beta}, \vec{k}_{\alpha}) \right|^2 , \tag{4.5}$$

and the related form in terms of the transition amplitude $\mathbf{T}_{\beta\alpha}$ as given by Satchler [Sat83]

$$\left(\frac{d\sigma}{d\Omega}\right)_{\beta\alpha} = \frac{\mu_{\alpha}\mu_{\beta}}{(2\pi\hbar^2)^2}\frac{k_{\beta}}{k_{\alpha}} \left| \mathbf{T}_{\beta\alpha}(\vec{k}_{\beta}, \vec{k}_{\alpha}) \right|^2 , \tag{4.6}$$

where the μ's are the reduced masses of the interacting pairs and appear, together with the wave numbers k as we change the notation from wave amplitudes to particle fluxes[1].

Consider the non-elastic transfer reaction represented by (4.1). The projectile a is a proton and b is the emitted ^{3}He-particle. The target and residual nuclei are related by $A = B + x$, where x is the transferred nucleon pair, which can be considered as a bound deuteron or *cluster* with quantum numbers N, L, S and J. The conservation rules for this reaction is

$$\vec{J}_A + \vec{s}_a + \vec{l}_a = \vec{J}_B + \vec{s}_b + \vec{l}_b \,. \tag{4.7}$$

Here the angular momentum of the target and residual nuclei are J_A and J_B respectively, the spins of the projectile a and emitted particle b are s_a and s_b respectively, and the relative orbital angular momentum in the entrance and exit channels are l_α and l_β respectively.

The angular momentum *transfers* are defined by

$$\vec{J}_B - \vec{J}_A = \vec{J}\,, \quad \vec{s}_a - \vec{s}_b = \vec{S}\,, \quad \vec{J} - \vec{S} = \vec{L} = \ell_\alpha - \ell_\beta \,, \tag{4.8}$$

and their respective projections related by

$$m = M_B - M_A + M_b - M_a \,. \tag{4.9}$$

where J, S and L are now the total angular momentum, intrinsic spin and orbital angular momentum carried off by the deuteron cluster.

[1]The relationship between $\mathbf{T}_{\beta\alpha}$ and $f_{\beta\alpha}$ is given by Satchler as $\mathbf{T}_{\beta\alpha} = -\frac{2\pi\hbar^2}{\mu_\beta} f_{\beta\alpha}$, where $p_\beta = \mu_\beta \upsilon_\beta$, and υ_β and υ_α are the velocities in the two channels.

Similarly, the vector-coupling relations for the isospin transfer T and 3-component N, are given by

$$\vec{T} = \vec{T}_B - \vec{T}_A = \vec{T}_a - \vec{T}_b \tag{4.10}$$

and

$$N = N_B - N_A = N_a - N_b \,. \tag{4.11}$$

When the incident beam of particles have intrinsic spin, the cross section needs to be averaged over the initial spin orientations of s_a and J_A and, since we are interested in the unpolarized cross section, summed over the final spin orientations of J_B and s_b. The differential cross section of (4.6) can then be written as

$$\left(\frac{d\sigma}{d\Omega}\right)_{\beta\alpha} = \frac{\mu_\alpha \mu_\beta}{(2\pi\hbar^2)^2}\frac{k_\beta}{k_\alpha}\frac{1}{(2J_A+1)(2s_a+1)}\sigma_{\beta\alpha}(\theta) \tag{4.12}$$

The function $\sigma_{\beta\alpha}(\theta)$ is called the *reduced cross section* [Sat83] which includes spin-orbit coupling and is given by

$$\sigma_{\beta\alpha}(\theta) = \sum_J \sum_{mM_bM_a} \times \left| \sum_{LST} C^{T_BT_AT}_{N_B,-N_AN} C^{T_bT_aT}_{N_b,-N_a,-N}\, \hat{T}^{-1} (-)^{T_A-N_A+T_a-N_a+T-N}\, t^{mM_bM_a,N}_{LSJ,T}(\theta,\phi) \right|^2 \tag{4.13}$$

where the C's are the Clebsch-Gordan coefficients[2] and the $\hat{T}$ notation implies $\sqrt{2T+1}$.

The *reduced* amplitude $t^{mM_bM_a,N}_{LSJ,T}$ in (4.13) is given by

$$t^{mM_bM_a,N}_{LSJ,T}(\theta,\phi) = \sum_{M'_bM'_a} C^{s_bs_a,S}_{M'_b,-M'_a,M'_{ba}} C^{SJ,L}_{M'_{ba}M_{BA},m'} \times (-)^{s_a-M'_a} \int d\vec{r}_\beta \int d\vec{r}_\alpha\; \chi^{(-)}_{M'_bM_b}(\vec{k}_\beta,\vec{r}_\beta)^*\, G^{m'}_{LSJ}(\vec{r}_\beta,\vec{r}_\alpha)\, \chi^{(+)}_{M'_aM_a}(\vec{k}_\alpha,\vec{r}_\alpha) \tag{4.14}$$

[2]Here we have used the notation of Glendenning [Gle83] for the Clebsch-Gordan coefficients, i.e. $C^{j_1j_2J}_{m_1m_2M} = \langle j_1m_1, j_2m_2|JM\rangle$ etc.

where $G^{m'}_{LSJ}$ represents the multipole components in the form factor describing the interaction $\alpha \rightarrow \beta$ and also depends on the isospin quantum numbers T and N. The primed numbers serve to signify the spin flips in the presences of spin-orbit coupling where $m' = M_B - M_A + M'_b - M'_a$.

The multipole components G^m_L in (4.14) behave under rotations like the conjugates of the spherical harmonic functions, Y^{m*}_L, and in the zero-range (ZR) form can be written as

$$G^{ZR,m}_{LSJ}(\vec{r}_\beta, \vec{r}_\alpha) = f_{LSJ}(r_\alpha)[i^L\, Y^m_L(\hat{r}_\alpha)]^*\, \delta(\vec{r}_\beta - \lambda\vec{r}_\alpha). \tag{4.15}$$

Bruge and Leonard [Bru70] give the differential cross section for the two-nucleon pickup reaction $a + A \rightarrow B + b$ as

$$\frac{d\sigma}{d\Omega} = \frac{\mu_a\mu_b}{(2\pi\hbar^2)^2}\frac{k_b}{k_a}\frac{(2s_b+1)}{(2s_a+1)} \times \sum_{LSJT} b^2_{ST} D^2_{ST} \left[C^{T_B T, T_A}_{N_B N, N_A}\right]^2 \sum_M \left|\sum_N g_{NLSJT} B^M_{NL}(\theta)\right|^2 \tag{4.16}$$

where the factor b_{ST} is the overlap factor involving the spin-isospin functions of the light nuclei, and D_{ST} are the interaction strengths between in the incoming proton and the center of mass of the transferred pair.

The kinematic or transfer amplitude B^M_{NL} is related to the amplitude in (4.14) and contains all the distorted wave amplitudes and details of the interacting potential. It represents the probability of transferring a structureless cluster out of an orbital state with N, J and L. A similar result is given by Glendenning [Gle65], Hardy and Tower [Har67], and Nann *et al.* [Nan74]. The nuclear structure information is contained in the structure factor g_{NLSJT} which is basically determined by the nuclear wave functions of the initial and final states [Nan74]. The structure factor contains the parentage factor connecting the target and residual nuclei.

4.1.2 The Zero-range Approximation

The DWUCK4 code employs a *zero-range approximation* for the interaction potential of the transferred nucleon pair, assuming a point-like cluster with relative S-state motion between the two nucleons. It is assumed that for light ions the interaction of the transferred particles is short range and can be replaced by a delta function, that is

$$D(\vec{r}_{ax}) = V(\vec{r}_{ax})\psi(\vec{r}_{ax}) \approx D_0\delta(\vec{r}_x - \vec{r}_a) \tag{4.17}$$

where D_0 is the strength factor in the zero-range approximation [Sat83].

The effect of this approximation is to neglect the range and size of the ^{3}He-particle wave function, and so in this sense the zero-range approximation is regarded as less accurate for two-nucleon transfer reactions than single-nucleon transfer [Ros71]. For (p,t) or (t,p) reactions the resulting zero-range angular distributions are found to be very close to those determined from proper finite-range calculations. In general the zero-range approximation tens to underestimate the absolute magnitude of the cross sections.

The validity of the zero-range approximation can to an extent be ensured by employing the *well-matching* condition, as described by e.g. Stock *et al.* [Sto67] and DelVecchio *et al.* [Del72], i.e.

$$V_p(r) + V_d(r) - V_{^3He}(r) \approx 0\,, \tag{4.18}$$

for the relationship between the proton, deuteron bound state and ^{3}He optical potentials.

In the present study we keep the geometry parameters of the bound state potential fixed, based on the optimization of de Meijer *et al.* [DeM81], which is discussed in more detail in Section 4.4, and then adjust the strength of the spin-orbit potential to satisfy (4.18).

4.1.3 Some Comments on the Validity of the DWBA

As long as non-elastic processes remain weak compared to elastic scattering, the DWBA is a good approximation. This is indeed the case if one compares the small cross sections of many reactions compared with the elastic cross section. Direct reactions like (d, p) stripping, for example, have cross sections which are largely dominated by a few surface partial waves. These are very weakly absorbed in the interior and play the dominant role in elastic scattering. Therefore, calculations for these peripheral scattering reactions are governed largely by optical potentials derived from measured elastic scattering data. On the other hand, the use of global optical potentials for reactions which could have strong absorption effects, is problematic. With increasing momentum mismatch (and L-space de-localization) the cross section is strongly affected by the lower absorbing partial waves. Scattering waves not well defined in the interior therefore suffer from this ambiguity [Sto67].

In the DWBA, by using elastic scattering optical potentials for the incident channel in pickup reactions, i.e. $V_{a,A} \approx U^{elas}_{a,A+x}$, effects like core excitations are neglected. The DWBA then disregards the non-elastic part of the interactions and assumes the projectile-residual potential to be absorbed into the proton optical potential. Making the assumption that $V_{a,A} + V_{x,A} = U^{elas}_{b}$, ignores the effects of intermediate states. These approximations imply the so-called *well-matching* condition for the optical potential given by (4.18).

4.2 Optical Potentials

The theoretical calculations of the distorted waves in the DWBA are based on phenomenological optical model potentials for the interaction of the light particles with the target and residual nucleus. These ”optical” potentials (OP) are complex functions with real and imaginary terms. The real potentials are responsible for normal refraction of the incident beam and produce shape elastic scattering, while the imaginary terms account for

the absorption of flux from the elastic channel. All the optical potentials have the same general format but with different potential parameters. The parameters are taken from global studies that attempt to reproduce a large selection of elastic scattering data over a wide range of energies and target masses, so-called *global* optical potentials.

The OP generally consists of central, real and imaginary volume terms, an imaginary surface term, and a peripheral spin-orbit term. It is written as

$$U(r) = V_C(r) \underbrace{- V_0 f_v(r) - iW_0 f_w(r)}_{volume} + \underbrace{i4a_s W_s \frac{d}{dr} f_s(r)}_{surface} + \underbrace{\left(\frac{\hbar}{m_\pi c}\right)^2 \frac{V_{so} + iW_{so}}{r} \frac{d}{dr} f_{so}(r) \left(\vec{l} \cdot \vec{s}\right)}_{surface\ spin-orbit}. \tag{4.19}$$

The radial part of the OP, the form factor $f(r)$, has a Woods-Saxon shape, given by

$$f_i(r) = \left(1 + e^{\frac{r-R_i}{a_i}}\right)^{-1}, \tag{4.20}$$

where the radius $R_i = r_i A^{1/3}$ is the mean radius of the potential well and a_i the surface diffuseness parameter for $i = \{v, w, s, so\}$. This Woods-Saxon shape is roughly similar in shape to the charge distribution in nuclei. The last term is the spin-orbit term included to account for the interplay between the intrinsic spin of the projectile s and the relative orbital angular momentum of the projectile with the target nucleus, l. The factor $(\hbar/m_\pi c)^2 = 2.00\ fm^2$ is the pion Compton-wavelength and is included so that the potentials are written in MeV.

To this a central Coulomb term $V_C(r)$ is added. It has the standard form which represents a charged sphere of radius R_C and is given by

$$V_C(r) = \begin{cases} \frac{Z_a Z_A e^2}{r} & \ldots (r \geq R_C) \\ \frac{Z_a Z_A e^2}{2R_C}\left(3 - \frac{r^2}{R_C^2}\right) & \ldots (r \leq R_C) \end{cases} \tag{4.21}$$

where Z_a and Z_A are the charge numbers of the projectile and target, and e is the elementary charge.

The global optical potentials for the ^{3}He-particles [Lia09, Pan09], although based on cross section data for many target nuclei at a wide energy range, all suffer from the same shortfall of not incorporating analyzing power data, simply because it is not available. This can cause a certain amount of ambiguity. In the words of Satchler, "*Of course, spin-orbit couplings are essential for a proper description of polarization phenomena*"[3].

4.2.1 Deuteron Bound State

In the macroscopic or cluster description the incoming proton picks up a proton-neutron pair, or deuteron[4], from some cluster shell model state with quantum numbers N, J and L. The bound state wave function of the "deuteron" in the nucleus is determined from a fixed-geometry Woods-Saxon type optical potential with a well depth adjusted to give the correct binding energy and number of nodes. The separation energy of a deuteron in the ^{58}Ni nucleus was calculated as 17.324 MeV [Cat05]. The mean radius r_0 and diffuseness parameter a are taken as 1.15 fm and 0.76 fm respectively, which have been selected to ensure that the shape of the form factors in the macroscopic and microscopic approach are almost identical [DeM81, DeM82, Sen83].

The exact spin-orbit strength in the bound state, on the other hand, is not obvious. The well-depth procedure proposed by de Meijer *et al*. [DeM82] was derived on the basis of no spin-orbit term in the bound state potential. The inclusion of spin-orbit interactions in the macroscopic calculations, which treat the contributing L-transfers incoherently, may cause deviations from an otherwise coherent microscopic calculation.

In the present study the geometry of the spin-orbit potential was chosen to be the

[3] Taken from Satchler [Sat83], page 732

[4] There is really no significant distinction being made between a deuteron and a proton-neutron pair.

same as that of the real, central potential mentioned above and the relevant strengths were further restricted by considering the well-matching prescription which minimizes the effect of finite range corrections [Sto67, Del72].

From the conservation of harmonic oscillator shell model quanta, the cluster bound state is related to those of the individual nucleons [Car84] by

$$2(N-1)+L=\sum_{i=p,n}2(n_i-1)+l_i\,, \tag{4.22}$$

where the sum is for the transferred proton and neutron occupying independent-particle shell model orbitals with n_i and l_i, and where we consider the transferred nucleon pair to have no internal relative motion. This expression, although strictly valid for harmonic-oscillator wave functions, is assumed to apply also to Woods-Saxon type wave functions [DeM82]. The number $(N-1)$ represents the number of nodes in the bound state wave function, excluding the origin and infinity.

According to Bruge and Leonard [Bru70] the lowest energy states in ^{56}Co are expected to be one-particle-one-hole states where the proton is usually picked up form the $1f_{7/2}$ shell and the neutron from any of the $2p_{3/2}$, $2p_{1/2}$ or $1f_{5/2}$ shells. These states are expected to lie below about 3.5 MeV. At higher energies two-particle-two-hole configurations like $\left[\left(\pi f_{7/2}\right)^{-1}\left(\nu f_{7/2}\right)^{-1}\left(\nu p_{3/2}\right)^{2}\right]$ are expected. These are illustrated in Figure 4.2.

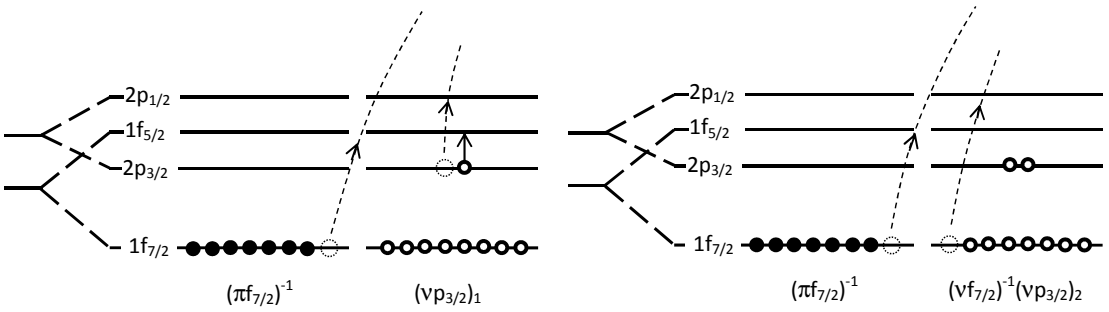

Figure 4.2: Illustration of 1-particle-1-hole (left) and 2-particle-2-hole (right) states in ^{56}Co.

If, for example, both the proton and neutron is picked up from the $1f_{7/2}$ shell, equation (4.22) gives, for n_i = 1 and l_i = 3,

$$2(N-1)+L=6\,, \tag{4.23}$$

where N can then be 1, 2, 3 and 4, corresponding to L-values of 6, 4, 2 and 0. Similarly, for transfers in which the proton-neutron pair is picked up from combinations of the $1f$ and $2p$ shells, the same result as in (4.23) is found. Table 4.1 summarizes the different combinations of N and L.

4.3 Polarization and Analyzing Power

The concept of analyzing power stems from the observed asymmetry in the scattering of projectiles with non-zero spin from target nuclei due to the *spin-orbit interaction* between the intrinsic spin of the projectile and its orbital angular momentum relative to the target.

The polarization $\vec{P}$ of an incident beam of spin-1/2 particles is defined as the normalized ensemble average of spins in terms of the statistical density matrix ρ and the Pauli spin operators $\vec{\sigma}$ as

$$\vec{P}=\frac{Tr(\rho\,\vec{\sigma})}{Tr\;\rho}\,. \tag{4.24}$$

The polarization in a particular direction, say the $\hat{n}$-direction of Section 2.2.1, of a beam of particles which can have two possible orientations, is the *difference* in the fraction of particles which have their spins aligned in that direction. As an example, consider a spin-up polarization of 0.7, which means there are 70% *more* particles in the beam with their spins aligned in the ”up” direction than in the ”down” direction. If there is the same number of particle with their spins up as there is with their spins down, then the

polarisation would be zero.

The *analyzing power* is one of many *spin transfer observables* $D_{i'j}$ which relate the i-th component of the scattered beam polarization to the j-th component of the incident beam polarization in terms of the scattering matrix M and the Pauli spin operators $\vec{\sigma}$ [Hil90], given by

$$D_{i'j} = \frac{Tr(M\sigma_j M^\dagger \sigma_i)}{Tr(MM^\dagger)}\,, \tag{4.25}$$

The analyzing power is the spin transfer observable that projects an initial spin in the $\hat{n}$-direction perpendicular to the horizontal scattering plane onto zero polarization, i.e.

$$A_y \equiv D_{0n} = \frac{Tr(M\sigma_1 M^\dagger)}{Tr(MM^\dagger)}\,, \tag{4.26}$$

The differential cross section for the scattering of nucleons with polarization $\vec{P}$ from an unpolarized target, written in terms of the polarization and analyzing power as derived by Hillhouse [Hil90], is given by

$$\sigma(\theta) = \sigma_0(\theta)\left[1 + \vec{P}\cdot A_y\hat{n}\right]\,. \tag{4.27}$$

where $\sigma_0(\theta)$ is the unpolarized cross section. Combining the expressions for scattering to an angle θ when the beam polarization vector is in the "up" (positive $\hat{n}$) direction with that for a beam polarized in the "down" direction, equations (A.2) and (A.3), gives the expression for the analyzing power A_y as

$$A_y(\theta) = \frac{\sigma^\uparrow(\theta) - \sigma^\downarrow(\theta)}{\sigma^\uparrow(\theta)p^\downarrow + \sigma^\downarrow(\theta)p^\uparrow}\,. \tag{4.28}$$

4.4 Numerical Calculations with DWUCK4

The theoretical calculations for the differential cross section and analyzing power were performed with the computer code DWUCK4 by Kunz and Rost [Kun93] which calculates the *reduced cross section* and other reaction observables from the distorted-wave Born approximation (DWBA) in a zero-range approach. In the code the cross sections are determined using different normalizations which depend on the nature of the reaction, be it inelastic scattering or particle transfer.

The reaction calculation can be done *microscopically* or *macroscopically*. In the microscopic approach the transferred proton and neutron are picked up from separately defined single particle states and the form factor determined from the sum over all possible two-particle configurations. Macroscopic calculations assume that the transferred proton-neutron pair is without internal structure and is bound in some cluster shell model state with quantum numbers N, L, S and J. In the present study the calculations were done with a macroscopic approach in order to investigate the behaviour of the simple direct process without the added complexities in defining the wave functions of the transferred nucleon pair and their correlations.

Although in principle a microscopic calculation would be more accurate, it does depend on knowledge about the individual amplitudes of the contributing configurations. However, for the bound ”deuteron” it has been found that the macroscopic and microscopic calculations give form factors similar in shape when the geometrical parameters for the Woods-Saxon type potential are chosen correctly [DeM81, DeM82]. As noted by Sens and de Meijer [Sen83], a macroscopic calculation allows one to deduce two-nucleon spectroscopic factors by adjusting the contributions of different possible L-values separately for an optimum agreement with experiment.

4.4.1 Selection Rules

For a spin-zero target nucleus, J_A = 0, so that we have, from (4.8),

$$\vec{J} = \vec{J}_B = \vec{L} + \vec{S}\,. \tag{4.29}$$

The possible intrinsic spin transfers, S are $\vec{s}_a - \vec{s}_b = 1/2 \pm 1/2 = 0$ or 1, and so the total angular momentum transfer, J is limited to L, $L \pm 1$. Since the total transferred spin has to be carried off by the deuteron cluster, its total spin is therefore also $\vec{J}$. If we assume the three nucleons in ^{3}He have zero relative angular momentum, then we also have $S + T = 1$ [Bru69, Bru70].

The parity for the final state in the reaction is just a combination of the parities of the target nucleus, that of the transferred deuteron and the contribution from the transferred orbital angular momentum which is positive only i.e.

$$\begin{aligned} \pi_f &= (+1)\cdot(+1)\cdot(-1)^{L_{tr}} \\ &= (-1)^{L_{tr}} \end{aligned} \tag{4.30}$$

We see that for a spin-0 target and transitions to positive-parity states in ^{56}Co, only even L-values are possible. This is also found from (4.23). According to Bruge and Leonard [Bru70] the selection rules for the (p,^{3}He) reaction are summarized as:

- **for odd** J: S = 1, T = 0 (the proton-neutron pair being transferred from either the same or different shells)
- **for even** J: $J = L$ and both S = 0, T = 1 and S = 1, T = 0 may contribute. When the two transferred particles are picked up from the same shell however, only S = 0, T = 1 is possible.

The possible combinations are listed in Table 4.1 for a few L-values.

J_A	S	T	L	$J = J_B^\pi$	N
0	0,1	1,0	0	$0,1^+$	4
			2	$1,2,3^+$	3
			4	$3,4,5^+$	2
			6	$5,6,7^+$	1

Table 4.1: Possible quantum number combinations allowed by the selection rules.

4.4.2 Differential Cross Sections

According to Sens and de Meijer [Sen83] the experimental differential cross section for a two-nucleon pickup reaction to a particular state can be related to the calculated cross section from a code like DWUCK4 by the expression

$$\left(\frac{d\sigma(\theta)}{d\Omega}\right)_{JT}^{exp} = \frac{2s_b+1}{2s_a+1}C \times \sum_{LSJT} b_{ST}^2 D_{ST}^2 \left\langle T_B N_B; TN | T_A N_A \right\rangle^2 \frac{2S+1}{2J+1}\sigma_{DW}^L(\theta)\,, \quad (4.31)$$

where L, S, J and T refer to the transferred nucleon pair, and the function $\sigma_{DW}^L(\theta)$ is the reduced cross section in units of fm^2 sr^{-1} calculated by the DWUCK4 code[5], similar to (4.13) for a particular L-transfer.

The interaction strengths D_{ST}^2 between in the incoming proton and the center of mass of the transferred pair are 0.30 and 0.72 for T = 0 and T = 1 respectively [Nan74] and b_{ST}^2 is an overlap factor for the spin-isospin of the proton and ^{3}He-particle, and is 0.5 for both cases of S and T [Gle65]. The square of the Clebsch-Gordan coefficients involve the coupling of the isospin of the residual nucleus B and the transferred isospin to the isospin of the target A, and their respective 3-components. It is taken as 1.0 and 2.0 for T = 0 and T = 1 respectively as outlined in Appendix B. The factor C is a normalization constant that is adjusted for a best fit to the experimental angular distributions.

[5]Where 1 fm^2 sr^{-1} = 10 mb sr^{-1}.

The different spectroscopic factors listed above for the cases where both T = 0 or T = 1 are possible, can be calculated separately. Expression (4.31) can then be written more compactly for a specific state J as

$$\left(\frac{d\sigma(\theta)}{d\Omega}\right)^{exp}_{JT} = \mathbf{N}\sum_{L}\frac{1}{2J+1}\sigma^{L}_{DW}(\theta)\,, \tag{4.32}$$

where $\mathbf{N}_{T=0}$ = 0.45C and $\mathbf{N}_{T=1}$ = 0.72C for the two values of T.

In the macroscopic approach no internal structure information for the transferred proton-neutron pair correlations is needed besides the separation energy of the transferred proton-neutron pair, and a choice of cluster shell state with N, L and S. From (4.22) it is seen that only one N-value corresponds to each L-transfer. De Meijer *et al*. [DeM82] therefore suggested that, in the absence of spin-orbit terms, it is possible to separate the structure part in (4.16) from the kinematic amplitude B^{M}_{NL} so that the cross section may be written as an incoherent sum over the different L-transfers, each with an intensity A^2_L, namely

$$\left(\frac{d\sigma(\theta)}{d\Omega}\right)^{exp}_{J} = \mathbf{N}\sum_{J}\frac{1}{2J+1}\left\{A^2_L\;\sigma^{L}_{DW}(\theta) + A^2_{L+2}\;\sigma^{L+2}_{DW}(\theta)\right\}\,, \tag{4.33}$$

where the relative intensities can be deduced from the angular distributions and σ^{L}_{DW} and σ^{L+2}_{DW} are the output from DWUCK for the specific choices of L and L + 2. The relative intensities can then be viewed as experimental two-nucleon spectroscopic factors [DeM82].

The choice of the deuteron separation energy used in the macroscopic calculations is not obvious. De Meijer *et al*. [DeM82] discuss two separation energy procedures that can be followed, the individual single-nucleon separation energy method (ISNSEM), and the deuteron separation energy method (DSEM). For a microscopic calculation, the ISNSEM assumes that the separation energies of the individual transferred nucleons depend on their quantum numbers and are given by the experimental separation energies in the A_{core} + 1

nucleus. In the DSEM the separation energy of the deuteron in the target nucleus is divided equally between the transferred neutron and proton. The latter method therefore assumes that all configurations have the same separation energy.

In the present study we consider macroscopic calculations with the deuteron separation energies for the different configurations treated in a similar way as the DSEM, taken as the ground state separation energy of a deuteron from a ^{58}Ni-nucleus plus the excitation energy of each state. As noted by [DeM82], the DSEM has no theoretical justification and the main difference between these methods is the treatment of two-body correlation effects. However, the chosen method is simple and its deviation from the microscopic approach using the ISNSEM is assumed to be small.

4.4.3 Analyzing Powers

The numerical analyzing power values are calculated in the DWUCK4 code from the expectation value of the particular spin operator, similar to (4.26). In the case where more than one state or transition contribute to the total analyzing power, the experimental A_y is related to the theoretical value through the expression

$$(A_y)_{exp} = \frac{\sum_{LSJ} \sigma^{LSJ} A_y^{LSJ}}{\sum_{LSJ} \sigma^{LSJ}} \tag{4.34}$$

where the summation runs over the particular target states with possible L, S and J, each with analyzing power A_y^{LSJ} and cross section σ^{LSJ} taken as $\sigma_{DW}^{L}(\theta)$ directly for DWUCK. This is derived in Appendix A.4.

Chapter 5

Results

The excitation energy spectra for the $(p,^3\text{He})$ reaction on ^{58}Ni is shown in Figure 5.1 for the 80 MeV beam at scattering angles 25°, 30°, 35°, 40°, 45°, 50° and 60°. The prominent states in ^{56}Co have been identified as indicated. These are the states at 0.577, 1.009, 2.283, 3.544 and 5.081 MeV. Experimentally measured results for the differential cross sections and analyzing powers at different angles and beam energies are listed in Appendix C.

The most prominent states are those associated with large orbital angular momentum transfers which can be understood from momentum matching conditions between the transferred orbital angular momentum L and the momentum difference Δl between the incident and emitted particles [Woo71, Sat83]. This momentum difference is written from classical arguments as

$$\Delta l = R\left(k_f - k_i\right) , \tag{5.1}$$

where $R = 4.65$ fm is the nuclear radius of ^{58}Ni and k_i and k_f are the wave numbers for the incident proton and emitted ^{3}He-particle. Table 5.1 lists the calculation results for the

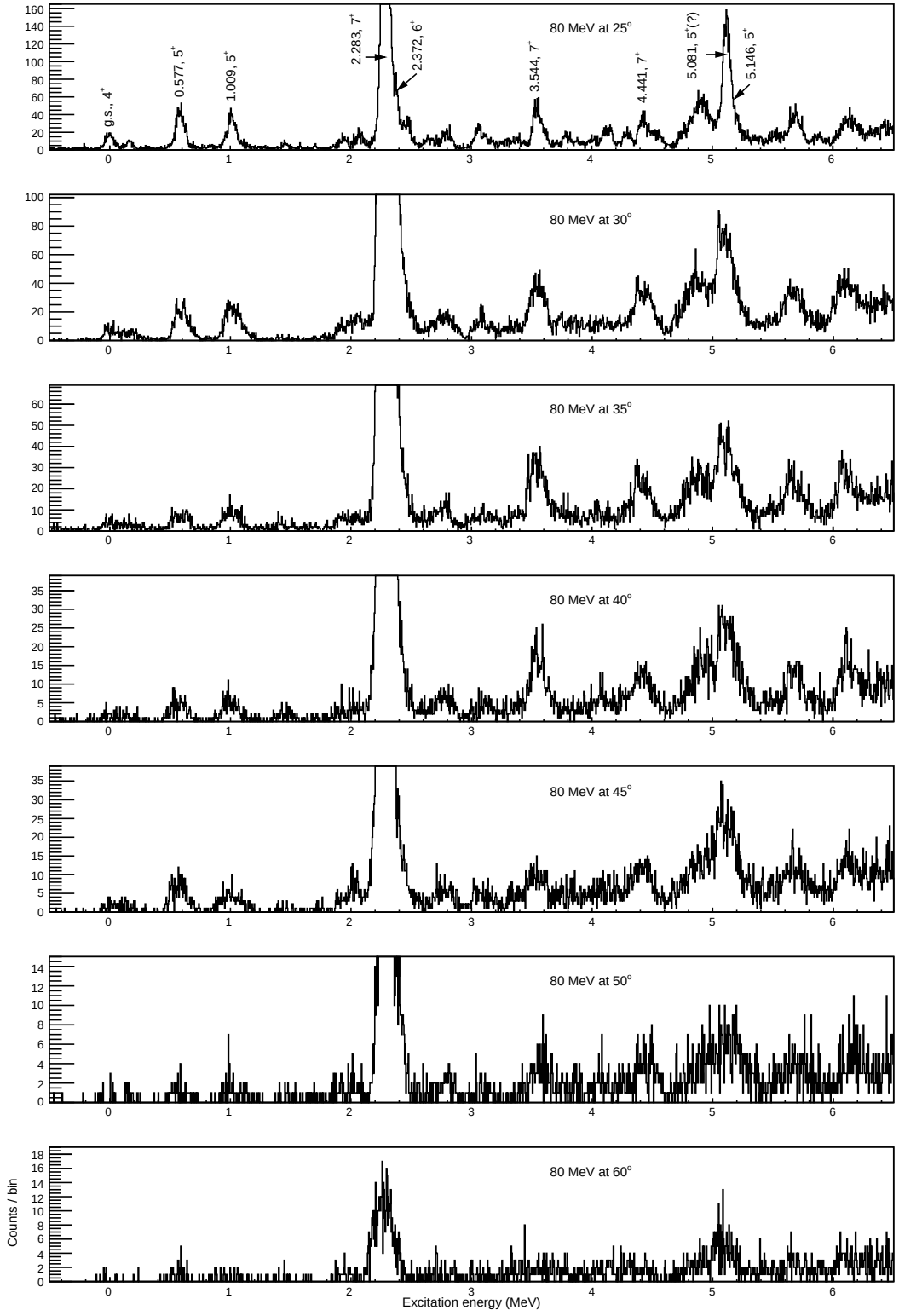

Figure 5.1: Excitation energy spectrum for the ^{58}Ni(p,^{3}He)^{56}Co reaction at 80 MeV beam energy indicating the energies (in MeV) and spins of a few prominent states.

three incident energies. Q-value for the ^{58}Ni(p,^{3}He)^{56}Co$_{(g.s.)}$ reaction is -11.83 MeV.

Particle	Energy[a] (MeV)	pc (MeV/c)	k (fm^{-1})	Δl [b]
p	80	395.63	1.96	
^{3}He	65	675.21	3.05	5.0
p	100	444.58	2.19	
^{3}He	84	756.23	3.49	6.0
p	118	485.14	2.38	
^{3}He	104	822.77	3.86	7.0

Table 5.1: Momentum difference between incident and emitted particles for the ^{58}Ni(p,^{3}He)^{56}Co (g.s.) reaction at 80, 100 and 120 MeV beam energy, calculated for a scattering angle of 25°.

Theoretical DWBA calculations of the differential cross section and analyzing power angular distributions for the states at 0.577, 1.009, 2.283, 3.544 and 5.081 MeV have been performed with the code DWUCK4 as described in Chapter 4. The theoretical results are compared with the measured observables and are plotted and discussed further throughout this chapter.

5.1 Sensitivity to the Optical Potentials

5.1.1 Different Optical Potential Sets

The optical potential parameters chosen for the distorted waves of the proton-target and ^{3}He-nucleus interactions are taken from global optical potential studies. The specific parameter sets considered in the present study are listed in Table 5.2 for the three incident energies and ground state interactions. For the proton-nucleus interaction the global parameter sets of Koning and Delaroche [Kon03] and those of Schwandt *et al.* [Sch82] were investigated. The energy dependent potential parameters of [Kon03] are derived from

elastic scattering data covering an energy range of 1 keV to 200 MeV and nuclides in the mass range of $24 \leq A \leq 209$ and include analyzing power data.

The ^{3}He-nucleus optical potential parameters found in the literature are much less consistent. The potentials considered in the present study were taken from global studies done by Liang *et al.* [Lia09] and those of Pang *et al*. [Pan09] as the most recent. Both parameter sets have been derived from a wide target mass range and energies of up to a few hundred MeV and give comparable results. Some discrepancies exist with the spin-orbit potentials, and neither authors claim much confidence in the parameterization of this particular part. Probably the biggest contributing factor to this ”shortcoming” is the lack of quality measurements of spin-dependent observables like analyzing power for ^{3}He-nucleus interactions.

The potential parameters used by Bruge and Leonard [Bru70] for the proton and ^{3}He-particles in their study at 45 MeV were also tested for comparison at the lower 80 MeV calculations, though not suitable for these higher 80 - 120 MeV beam energies. Figure 5.2 illustrates the results of the different optical potential sets investigated for the 2.283 MeV state at the 100 MeV incident energy as an example, and Figure 5.3 demonstrates the effects of the proton and ^{3}He potentials of [Bru70] on the 80 MeV incident energy data, compared to those of [Kon03] and [Lia09], also for the 2.283 MeV state. The curves were individually normalized to best fit the cross section data.

The proton-nucleus optical potential sets investigated have mostly similar parameters. At increasing incident energy the potential well depths decrease by a few MeV as is understood from kinematic considerations. Only [Bru70] and [Kon03] include surface absorption terms of $\sim$4-5 MeV. All the potential sets include a spin-orbit potential of $\sim$20 MeV, and, apart from [Bru70], all the sets have a $\sim$3 MeV imaginary spin-orbit potential. According to Koning and Delaroche [Kon03] the surface absorption term W_D is very small and tend to vanish at around 60 MeV. The imaginary part of the spin-orbit interaction only becomes important for energies above $\sim$100 MeV and is negative.

The optical potentials of [Kon03] and [Sch82] for the proton in the entrance channel give essentially the same results. The present study therefore used only the former sets for all further calculations as the most recent global set. The two global ^{3}He potential sets for the exit channel, [Lia09] and [Pan09], are also fairly consistent when one considers the sensitivity of the calculations to the parameters used for the description of the cluster bound state. The global potentials of Liang *et al*. [Lia09] were chosen for all the calculations, purely based on the slightly better description of the spin-orbit part of the potential.

5.1.2 Spin-Orbit Parameters in the Bound State Potential

An important ingredient of a phenomenological optical potential is the spin-orbit interaction. The coupling of the intrinsic spin of the projectile with its relative orbital angular momentum as it passes by the target nucleus produces a dependence on the relative orientation of its spin vector. The analyzing power clearly favours a definite spin-orbit potential for the bound state. Without this potential the analyzing power loses the characteristic oscillatory angular distributions seen, for example, in Figures 5.4, 5.5 and 5.6. It was found that the cross section and analyzing power calculations are very sensitive to the choice of bound state optical potential parameters. One must therefore be careful when choosing such parameters. These choices affect the normalization, as can be expected, but more so the overall shape of the angular distributions.

In the present analysis the bound state potential was determined by first choosing a mean radius r_0 = 1.15 fm and diffuseness parameter a = 0.76 fm such that the macroscopic and microscopic form factors are similar in shape, according to the discussion in Section 4.2.1. The strength of the real spin-orbit part is taken as proportional to the real central strength, i.e. $V_{so} = k' \times V_d$, where V_d is varied in the DWUCK code to give the correct binding energy and number of nodes for the deuteron in the target nucleus. The exact choice of the multiplication factor k' is then guided by the well-matching condition

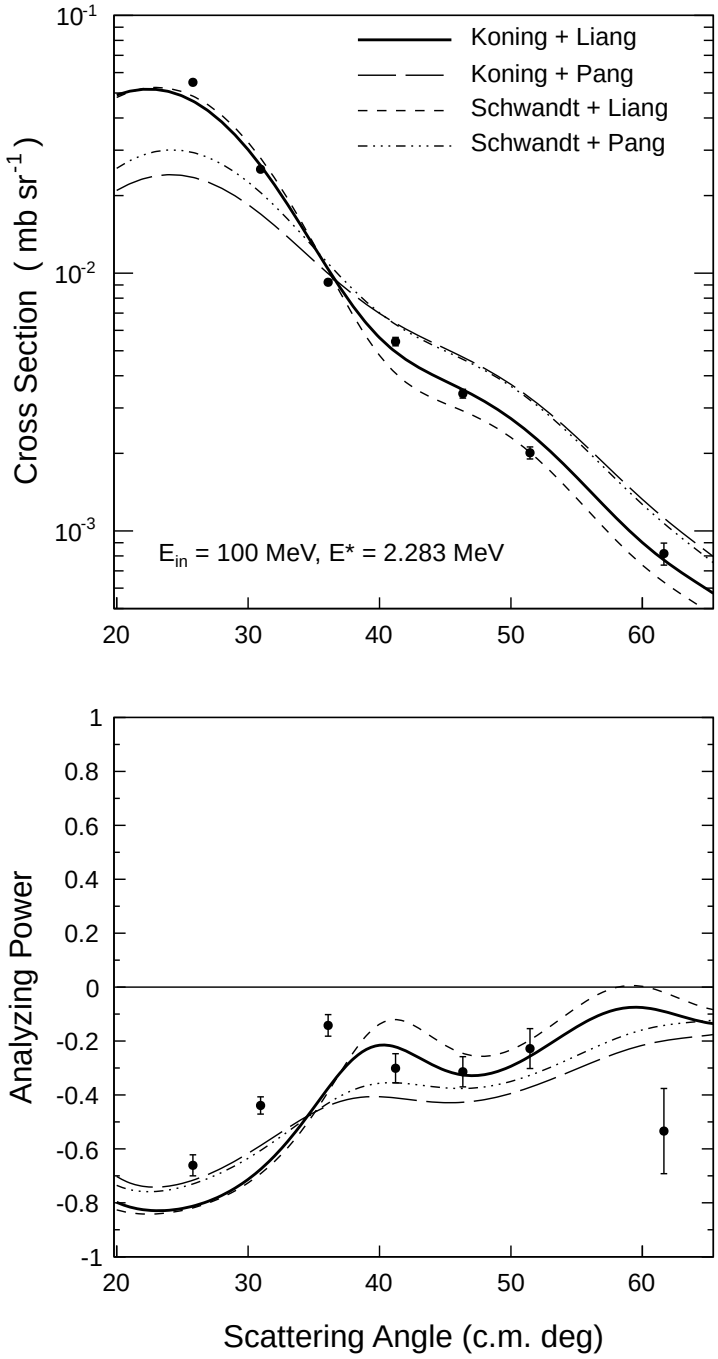

Figure 5.2: Comparison of the optical potential sets of Koning and Delaroche [Kon03], Schwandt *et al*. [Sch82], Liang *et al*. [Lia09] and Pang *et al*. [Pan09] for the ^{58}Ni(p,^{3}He) reaction to the 2.283 MeV excited state of ^{56}Co. The former two references are for the proton interactions while the latter two are for the ^{3}He particle. The two names in the label refer to the proton and ^{3}He OP sets respectively.

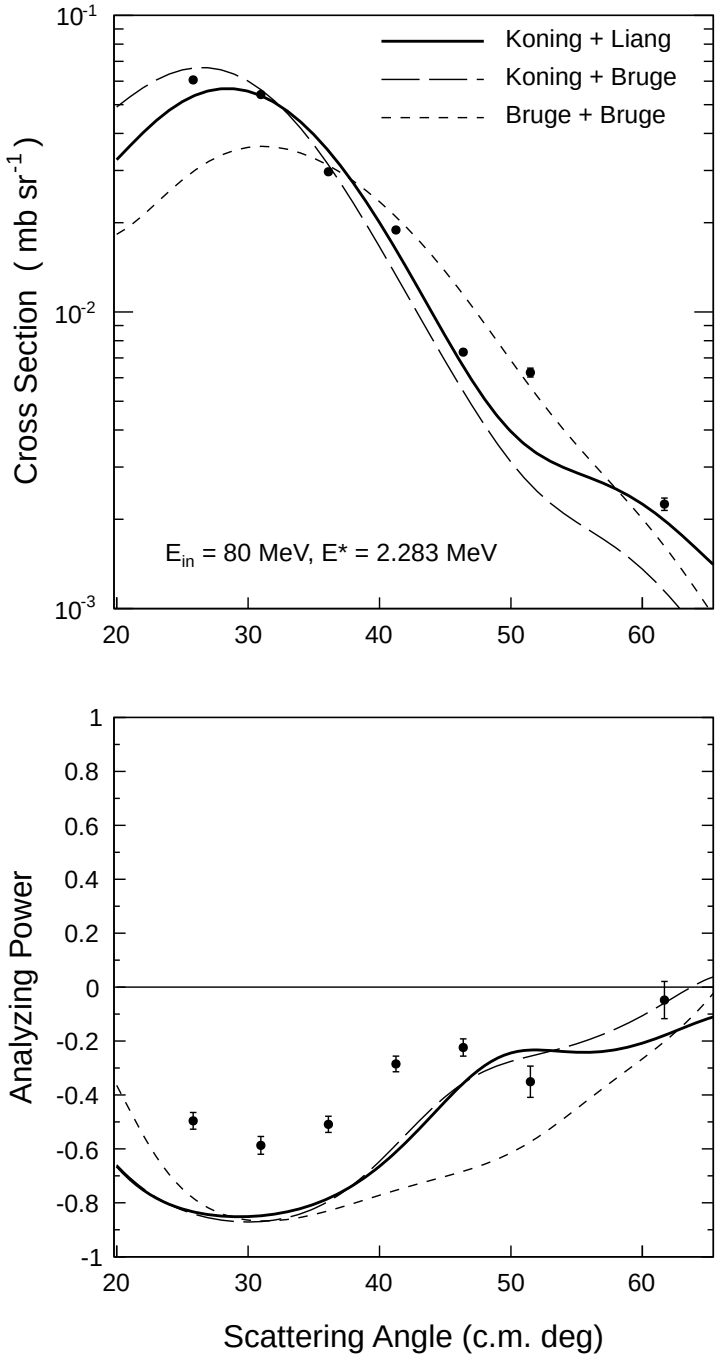

Figure 5.3: Comparison of the optical potential sets of Bruge and Leonard [Bru70] with those of Koning and Delaroche [Kon03] and Liang *et al.* [Lia09] for the ^{58}Ni(p,^{3}He) reaction to the 2.283 MeV excited state of ^{56}Co. The former two references are for the proton interactions while the latter two are for the ^{3}He particle. The two names in the label refer to the proton and ^{3}He OP sets respectively.

Interaction	Energy	Ref.	V_0	r_0	a_0	W_0	r_{w0}	a_{w0}	W_s	r_s	a_s	V_{so}	r_{vso}	a_{vso}	W_{so}	r_{wso}	a_{wso}
$p + {}^{58}$Ni	80	[Kon03]	-31.4	1.199	0.669	-8.5	1.199	0.669	5.3	1.281	0.549	-17.2	1.018	0.590	2.9	1.018	0.590
		[Sch82]	-30.9	1.205	0.700	-6.6	1.458	0.520				-20.2	1.038	0.672	2.6	1.016	0.620
		[Bru70]	-49.5	1.109	0.782	-6.5	1.477	0.495	4.1	1.477	0.495	-20.5	1.071	0.641			
^{3}He $+ {}^{56}$Co	65	[Pan09]	-112.3	1.175	0.820	-4.2	1.276	0.840	56.6	1.276	0.840	-1.6	0.948	0.130			
		[Lia09]	-110.1	1.176	0.781	-10.5	1.413	0.857	49.2	1.196	0.881	-8.4	0.736	0.969	4.6	0.736	0.969
		[Bru70]	-172.6	1.147	0.712	-20.2	1.562	0.802									
d		[DeM82]	-61.0	1.150	0.760							-70.2	1.150	0.760			
$p + {}^{58}$Ni	100	[Kon03]	-26.3	1.199	0.669	-10.0	1.199	0.669	3.4	1.281	0.549	-15.9	1.018	0.590	3.9	1.018	0.590
		[Sch82]	-27.1	1.225	0.706	-7.2	1.410	0.570				-17.4	1.038	0.648	4.3	1.016	0.620
^{3}He $+ {}^{56}$Co	84	[Pan09]	-109.7	1.175	0.820	-5.8	1.276	0.840	50.9	1.276	0.840						
		[Lia09]	-106.1	1.176	0.781	-14.7	1.413	0.857	37.8	1.196	0.881	-8.4	0.736	0.969	4.6	0.736	0.969
d		[DeM82]	-82.6	1.150	0.760							-37.2	1.150	0.760			
$p + {}^{58}$Ni	118	[Kon03]	-22.4	1.199	0.669	-11.0	1.199	0.669	2.3	1.281	0.549	-14.8	1.018	0.590	4.7	1.018	0.590
		[Sch82]	-24.3	1.243	0.712	-7.8	1.367	0.615				-15.3	1.038	0.626	5.5	1.016	0.620
^{3}He $+ {}^{56}$Co	102	[Pan09]	-107.5	1.175	0.820	-7.6	1.276	0.840	46.3	1.276	0.840	1.4	0.948	0.130			
		[Lia09]	-102.4	1.176	0.781	-18.1	1.413	0.857	26.9	1.196	0.881	-8.4	0.736	0.969	4.6	0.736	0.969
d		[DeM82]	-82.6	1.150	0.760							-37.2	1.150	0.760			

Table 5.2: Optical model potential parameters used in DWUCK4 for the 80, 100 and 120 MeV proton beams. All well depths are in MeV and lengths in fm.

given by (4.18), $V_p(r) + V_d(r) \approx V_{^3He}(r)$.

Within the constraints mentioned above, the potential strengths were therefore selected for each incident energy to give the best fit to experiment and, once optimized for a specific incident energy, it was kept fixed for all the states. Table 5.3 lists the results of a few choices of k' on the bound state central and spin-orbit potentials, illustrated for the 100 MeV incident energy. The effects of the different choices of k' on the cross section and analyzing power are demonstrated in Figures 5.4, 5.5 and 5.6.

V_{so} (MeV)	V_d (MeV)	V_p (MeV)	$V_{^3He}$ (MeV)
-146.2	-2.9		
-122.0	-22.6		
-98.4	-41.0		
-68.4	-62.2		
-45.6	-76.0		
-37.2	-82.6	-26.3	-106.3
-18.8	-94.0		
-7.0	-100.0		

Table 5.3: A comparison of the strengths of the real central V_d and spin-orbit potential V_{so} of the deuteron as determined by the DWUCK code illustrated in Figure 5.5. The calculations were made for the 2.283 MeV state at the 100 MeV beam energy with proton and ^{3}He real central potentials indicated next to the *well-matching* region described in the text. All the potentials listed are potential strengths only.

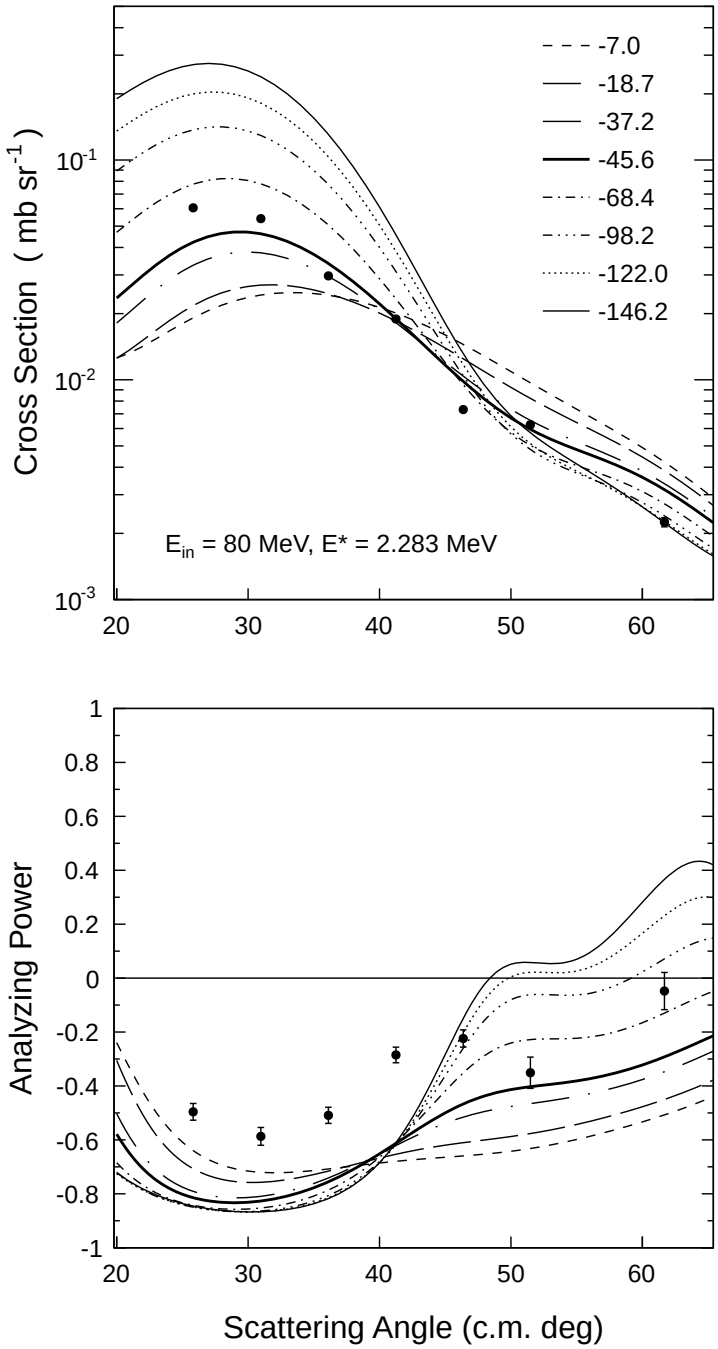

Figure 5.4: Comparison of the 80 MeV results of different choices of real spin-orbit potentials for the deuteron bound state. The different curves are labeled according to the resulting spin-orbit strengths (in MeV), where the dark solid line optimizes the well-matching condition mentioned in the text. The data are for the 2.283 MeV excited state.

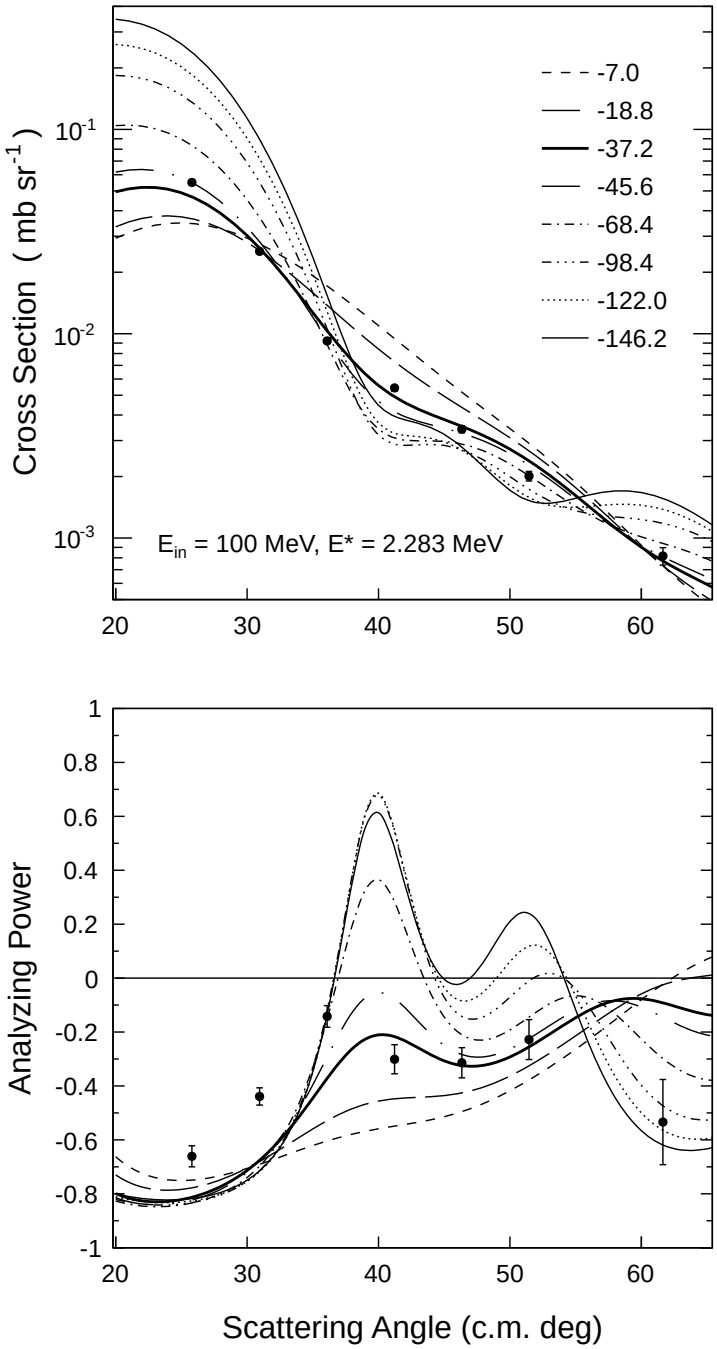

Figure 5.5: Comparison of the 100 MeV results of different choices of real spin-orbit potentials for the deuteron bound state. The different curves are labeled according to the resulting spin-orbit strengths (in MeV), where the dark solid line optimizes the well-matching condition mentioned in the text. The data are for the 2.283 MeV excited state.

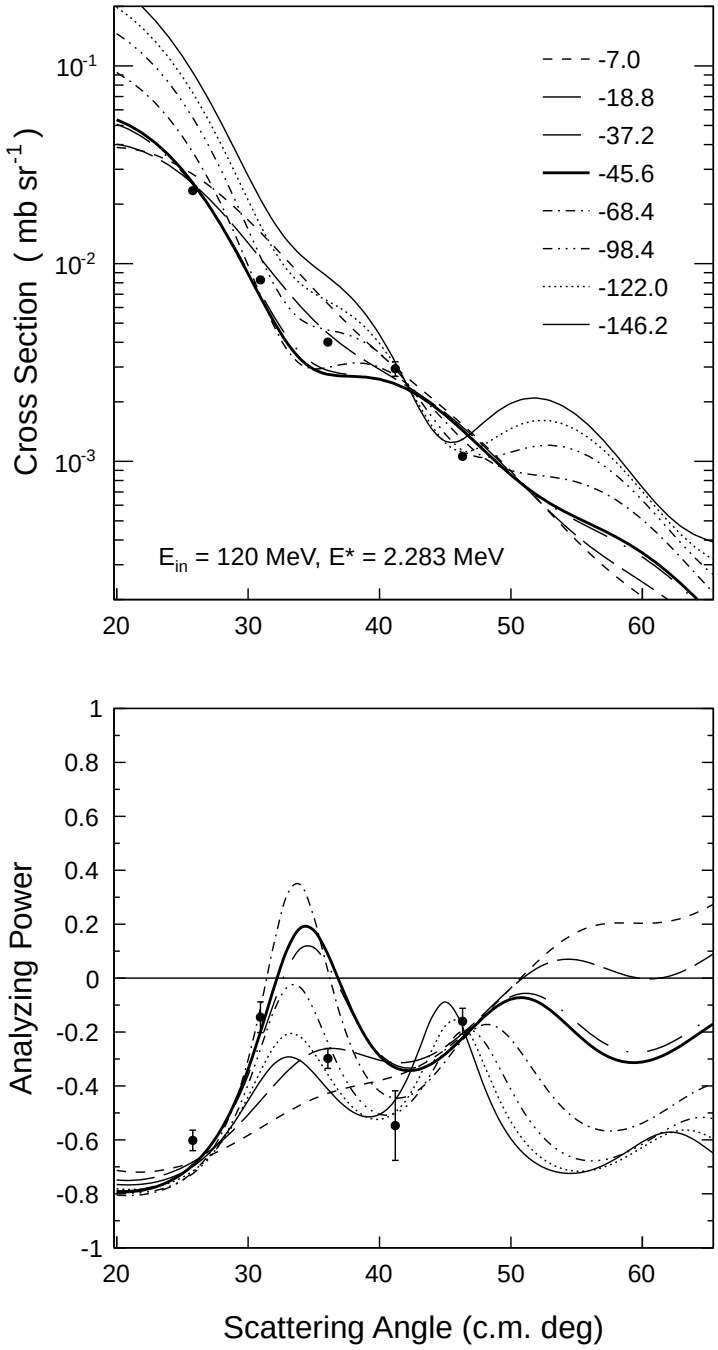

Figure 5.6: Comparison of the 120 MeV results of different choices of real spin-orbit potentials for the deuteron bound state. The different curves are labeled according to the resulting spin-orbit strengths (in MeV), where the dark solid line optimizes the well-matching condition mentioned in the text. The data are for the 2.283 MeV excited state.

5.2 Data Analysis and Fitting

The results of the DWUCK calculations were fitted to the experimentally measured cross section and analyzing power angular distributions, and the relative contributions from different possible L- and S-transfers were determined. The overall normalization factor C [see (4.31)] and extracted intensities A_L^2 and A_{L+2}^2 are listed in Table 6.1. These factors were all normalized to unity for the highest J = 7^+ transfer at an excitation energy of 2.283 MeV. The optimization of the fitting of the calculations to the data were performed with the aid of a standard χ-squared procedure, where the *goodness of fit* parameter was taken as χ^2, given by

$$\chi^2 = \sum_i \frac{(x_i - \mu_i)^2}{err_i^2}\,, \tag{5.2}$$

and where x_i is the i^{th} data point with its error err_i, and μ_i the corresponding calculated value.

The bound state potential parameters were optimized for the 2.283 MeV data at each incident energy by choosing a k'-value for which the theory best represents the angular distributions in the data, as discussed in Section 5.1.2. It can be noted that the 80 MeV data required quite a large deviation from the well-matching condition described in Section 4.1.2. This might be and indication of the inadequacy of the DWBA description in this energy range as the interior of the nucleus begins to contribute to the interaction, or the poor description of the bound state wave function.

The 2.283 MeV, 7^+ State

Of particular interest is the dominant state at 2.283 MeV. This state is strongly excited in two-nucleon transfer reactions like $(p,{}^3\mathrm{He})$ and (d,α) and has been well documented as J = 7^+ corresponding to a $(1f_{7/2})^{-2}_{\pi=\nu=7}(2p_{3/2})^2_{\pi=0,\nu=2}$ two-particle-two-hole configuration [Bru70, Hal84, Lud90, Nan81, Nan82, Sha84].

The 100 keV resolution at the focal plane limits the ability to resolve certain closely

spaced states. The peak around 2.283 MeV is a combination of a few unresolved states, amongst others, 2.283, 2.372 and 2.456 MeV, as can be seen in Figures 5.8 and 3.15, the 2.283 MeV state being the dominant transition by far. The state at 2.372 MeV have also been identified as having $L = 6$ by several authors [Sar76, Nan82]. Nann *et al.* [Nan82] suggested that this state has spin $J = 6^+$ and corresponds to the transfer of a $\left(\pi 1f_{7/2}, \nu 1f_{5/2}\right)_{J=6,T=0}$ proton-neutron pair.

Based on the poor statistics at larger angles and higher incident energies, it was not possible to deconvolute the peak in the 2.283 MeV region accurately. Figure 5.8 shows an attempted deconvolution of the 2.283 MeV peak region for the 80 MeV data. The theoretical calculations in this work has therefore been done for a combination of the 2.283 and 2.372 MeV states - the contribution of the 2.456 MeV is considered negligible based on its small L-value and its diminishing presence at the larger angles, seen in the multiple Gaussian fits. It is also clear from Figure 5.7 that both the cross section and analyzing power data are dominated by the $J = 7^+$ calculations. Figure 5.7 also serves to illustrate how the cross section is not as sensitive to the J-value as the analyzing power angular distributions, which, on average, have opposite signs for $J = 7^+$ and $J = 6^+$ for the same $L = 6$.

Nann *et al.* [Nan82] also sees similarities in the shapes of the analyzing powers of the strong 2.283 MeV state and those at 3.544 and 4.441 MeV. It has therefore been suggested that they all originate from the transfer of the proton-neutron pair from a $\left(1f_{7/2}\right)^2_{J=7,T=0}$ configuration, again with $L = 6$.

Deconvolution of the 2.283 MeV region at the 80 MeV beam energy

An attempt at a deconvolution of the three unresolved peaks in the 2.283 MeV region by means of multiple Gaussian fits, can be seen in the spectra in Figure 5.8. The resulting differential cross section and DWBA calculations are presented in Figure 5.9. The analysis confirms that the 2.283 MeV state with $J = 7^+$ dominates the total cross section, with

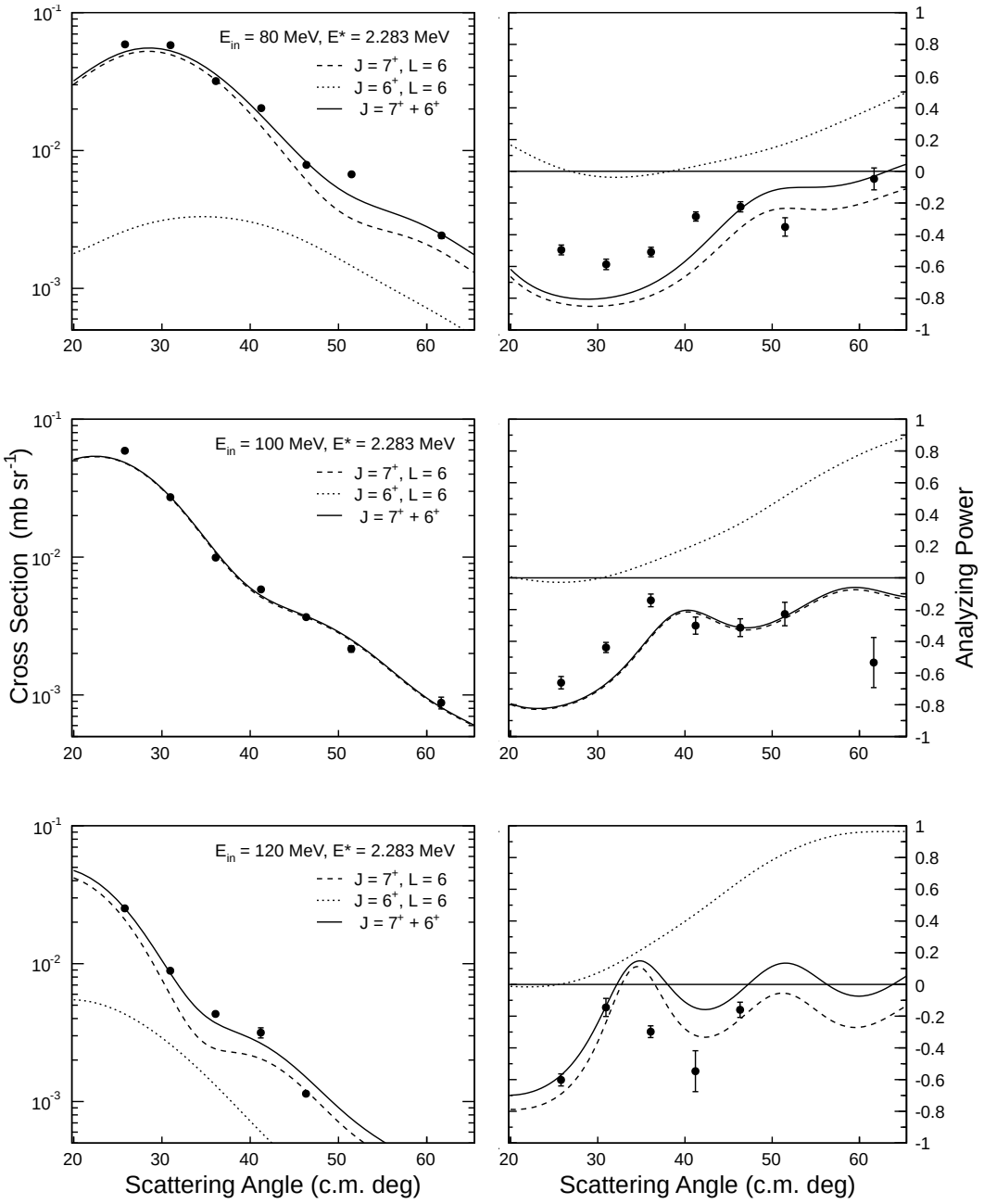

Figure 5.7: Differential cross sections (left) and analyzing powers (right) for the 2.283 MeV excited state of ^{56}Co in the ^{58}Ni(p,^{3}He)^{56}Co reaction at 80 MeV (top), 100 MeV (middle) and 120 MeV (bottom).

a normalization found to be very similar to that of the combined analysis. Also seen are the different contributions of the 2.372 MeV state at different angles. It would seem that the $J = 6^+$ description of this latter state, presumed at 2.372 MeV, is not that successful, while the $J = 1^+$ calculation appears to be fairly good. The normalization factors for the states analyzed are listed in Table 5.4.

E^* (MeV)	J^π	L; L+2	C
2.283	7^+	6	=1
2.372	6^+	6	0.08
2.456	1^+	0; 2	0.06; 0.40

Table 5.4: The resulting fitting normalization factors for the three deconvoluted states in the unresolved 2.283 MeV region. The factors are normalized to the 2.283 MeV state.

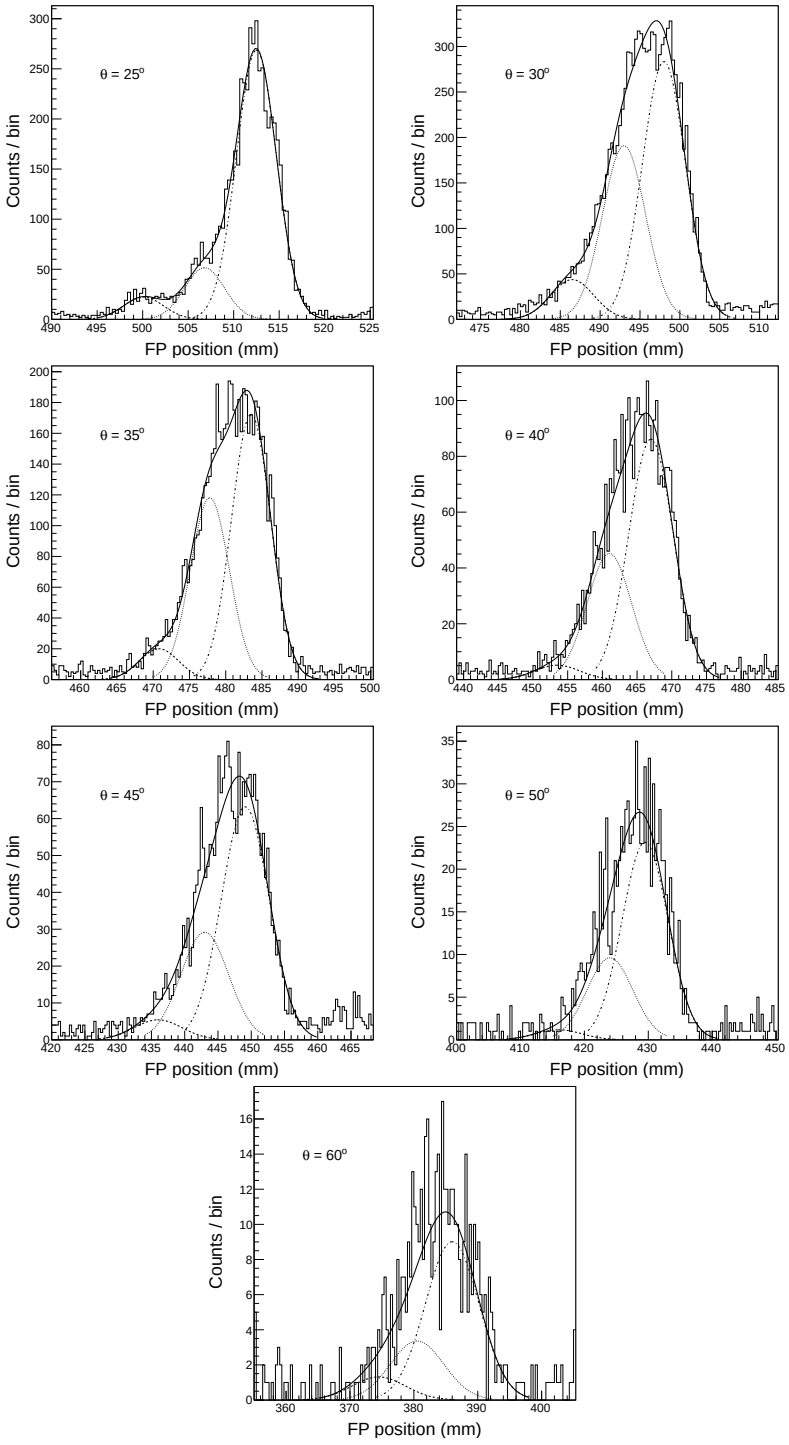

Figure 5.8: Multiple Gaussian fits on the peak in the region of 2.1 - 2.5 MeV for the 80 MeV data set for the different scattering angles. The three components from left to right in each panel are the 2.456, 2.372 and 2.283 MeV states.

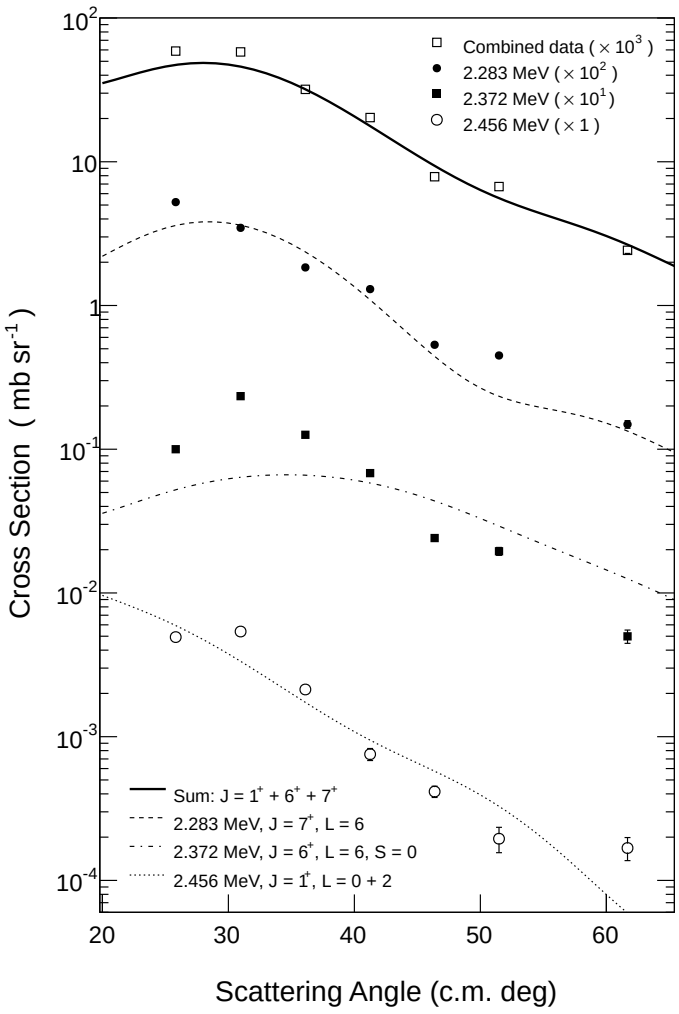

Figure 5.9: Experimental differential cross sections for the three unresolved states in the 2.283 MeV peak region for the 80 MeV beam energy, as well as DWBA calculations for the suggested states. The empty squares represent the experimental results of the whole unresolved region, as described in the text.

The 0.577 MeV, 5^+ State

Results for the excited state seen at 0.577 MeV are shown in Figure 5.10. An example of the spectrum around that region is shown in Figure 5.11. It is the only state that is cleanly separated from other states. It has been reported as a $J = 5^+$ state in many studies [Bru70, Gam80, Nan82, Lud90]. Included in the calculations are the contributions of both $L = 4$ and $L = 6$. It would seem that $L = 4$ dominates the reaction in agreement with the references which states that the proton-neutron pair is picked up with $L = 4$ from the $(\pi 1f_{7/2})^{-1}(\nu 2p_{3/2})^2$ levels. A very small addition of $L = 6$ helps to fit the cross section data slightly better over the entire incident energy range.

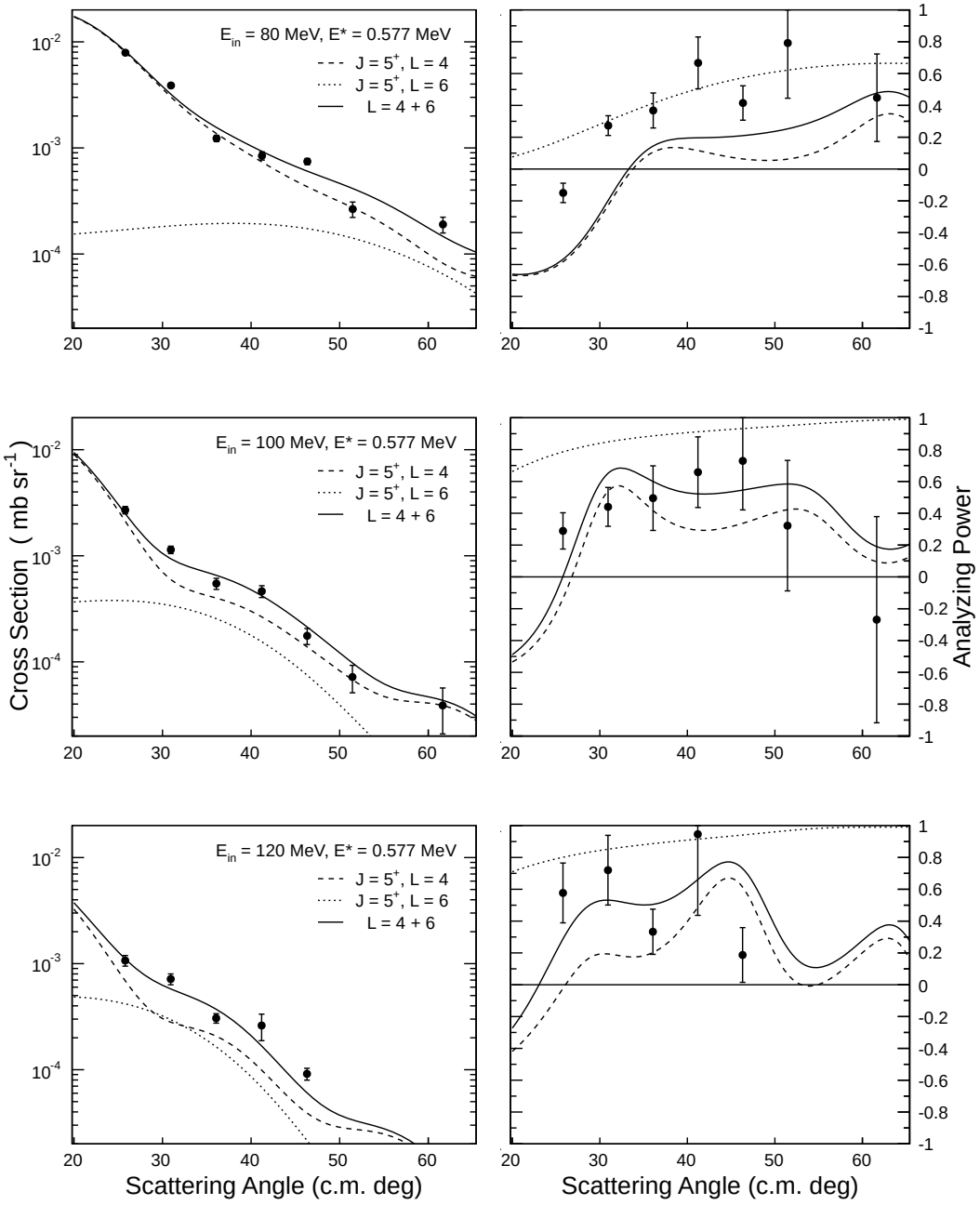

Figure 5.10: Differential cross sections (left) and analyzing powers (right) for the 0.577 MeV excited state of ^{56}Co in the ^{58}Ni(p,^{3}He)^{56}Co reaction at 80 MeV (top), 100 MeV (middle) and 120 MeV (bottom).

The 1.009 MeV, 5^+ State

The excitation energy region up to 1.2 MeV is shown in Figure 5.11 together with the results of a multiple Gaussian fit for the two prominent peaks. It was not possible to resolve the three known states at 1.115, 1.009 and 0.970 MeV which were reported by, amongst others, Bruge and Leonard [Bru70]. In the present study we considered the combined counts of the three states when comparing with the DWBA calculations.

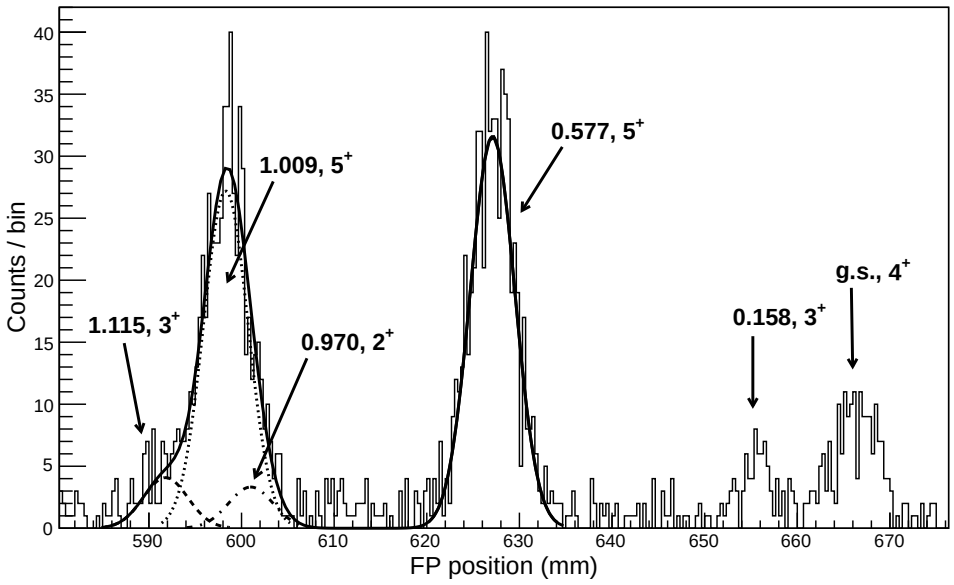

Figure 5.11: Multiple Gaussian peak fit for the peaks in the region of 0 - 1.2 MeV. The data are that of 25° and 80 MeV beam energy. The different peaks are labeled by their respective excitation energies in MeV.

The states at 0.970, 1.009 and 1.115 MeV have been identified in the study of Bruge and Leonard [Bru70] as $J = 3^+$ ($L = 2$), $J = 2^+$ ($L = 2$) and $J = 5^+$ ($L = 4$) respectively, and Gambhir [Gam80] was able to fit the cross section data of these states with $J = 2^+$ ($L = 2$), $J = 5^+$ ($L = 4$) and $J = 3^+$ ($L = 2$) spin assignments respectively, with an average contribution from both $S = 0$ and 1 transfers to the $J = 2$ state. A later work of Nann *et al.* [Nan82] saw similarities in the analyzing powers of the 1.009 Mev state with that of the 0.577 MeV state, identifying them as $J = 5^+$, $L = 4$ transitions.

It was not possible, in the present study, to determine the relative contributions of the different spin transfers of the constituent states to the peak around 1 MeV unambiguously, due to the low energy resolution and poor counting statistics. We therefore made the assumption that the 5^+ state at 1.009 MeV with $L = 4$, would be dominant at the higher incident energies, based on the momentum matching conditions (Table 5.1). This is certainly a good choice as can be seen from the excellent fit to the 100 and 120 MeV cross section data in Figure 5.12. The analyzing power angular distributions for the 100 and 120 MeV beam energies also seem to confirm this $J = 5^+$ dominance, having mostly positive values in agreement with the data. This result is indeed very promising, highlighting the importance of including analyzing powers for a complete reaction mechanism analysis.

The fitting of the 80 MeV incident energy data is much more difficult. The $J = 5^+$ state at 1.009 MeV is not as prominent here as in the 100 and 120 MeV cases. We can, however, attempt a speculative fit based on the shape of the angular distributions by making the assumptions that the 5^+ state is primarily an $L = 4$ [Gam80, Nan82] transition, that the 3^+ state at 1.115 MeV has primarily $L = 2$, as suggested by [Gam80], and assuming equal contributions from the $S = 0$ and $S = 1$ transfers for the 2^+ state at 0.970 MeV. The angular distributions of these spin assignments for the 80 MeV beam energy are also shown in Figure 5.12.

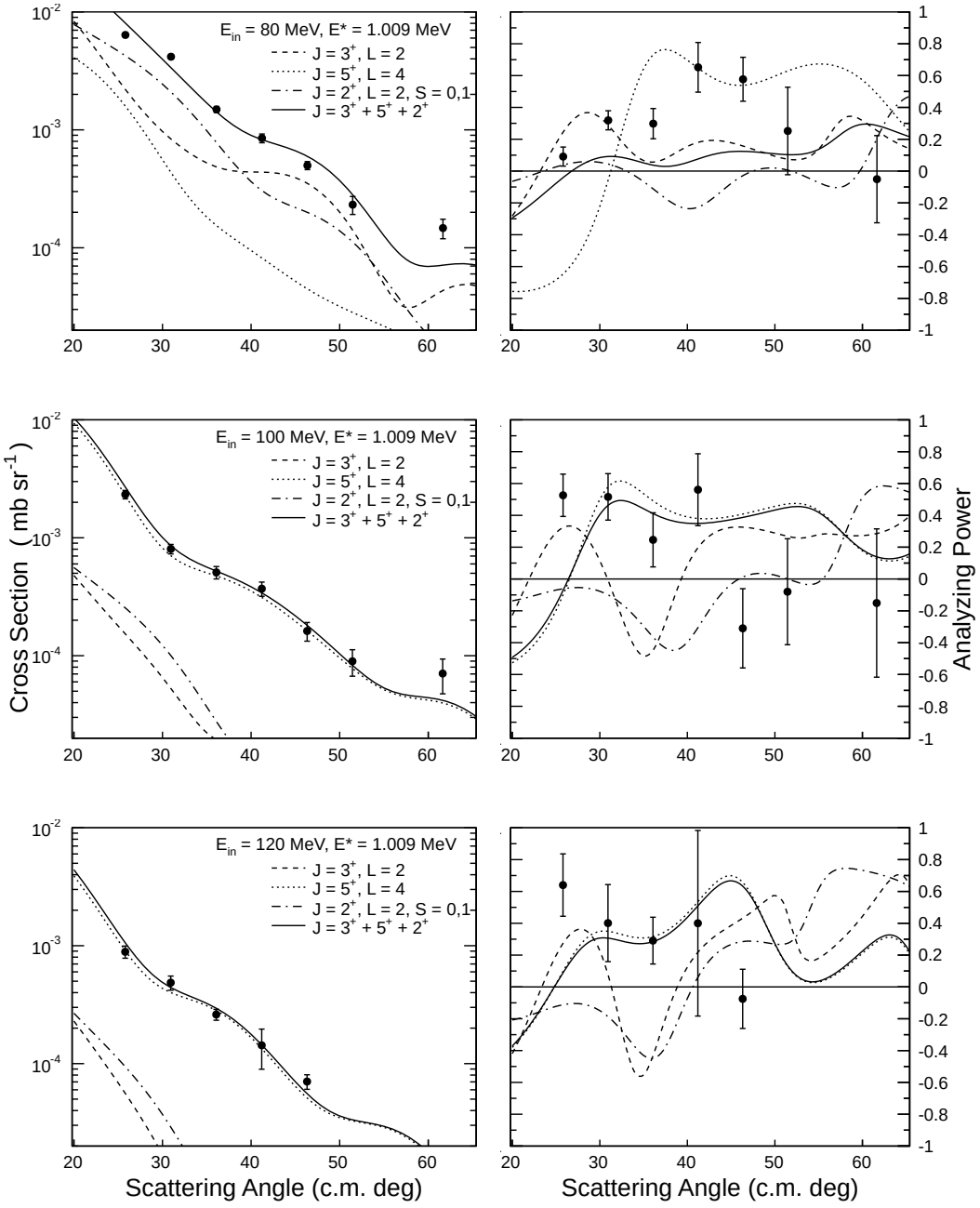

Figure 5.12: Differential cross sections (left) and analyzing powers (right) for the excited states identified around 1 MeV in ^{56}Co. DWBA calculations are included for the unresolved states at 1.115 MeV ($J = 3^+$, $L = 2$), 1.009 MeV ($J = 5^+$, $L = 4$) and 0.970 MeV ($J = 2^+$, $L = 2$, $S = 0{,}1$). The results for the 80 MeV beam is at the top, the 100 MeV in the middle, and the 120 MeV at the bottom.

The 3.544 MeV, 7^+ State

Transitions to the 3.544 MeV state have been identified by Nann *et al.* [Nan81, Nan82] as $J = 7^+$, showing characteristic $L = 6$ angular distributions, and also similar analyzing power angular distributions to that of the 2.283 MeV state. This is certainly the case for the experimental data in the present study as can be seen in Figure 5.13. The trends in the angular data over the three incident energies clearly follow the same tendency as seen in the 2.283 MeV excitation. This state is also, together with the 2.283 MeV state, the only one measured with primarily negative analyzing powers amongst those analyzed. The agreement between the $J = 7$ assignment and the data is reasonable with at least the correct change in trends at increasing incident energy. The same discrepancies between the calculations and the data seen for the 2.283 MeV state is also present in these fits.

On the other hand, Bruge and Leonard [Bru70] have measured $J = 0^+$, $L = 0$ cross section angular distributions for the states at 3.501 and 3.587 MeV (excitation energies as in the reference) at an incident energy of 45 MeV, as did Belote *et al.* [Bel68] at 7 MeV. However these latter assignments are not at all certain. It is highly unlikely that these low L states will be excited in the present reaction based on the high incident energies and consequent large momentum mismatch. Calculations for $J = 0^+$ transfer seem to confirms this, having different phases to the data at around 35°. A comparison calculation between the $J = 7^+$ and $J = 0^+$ is given in Figure 5.14.

This discrepancy is most probably due to the presence of the state at 3.599 MeV which is not resolved from the one at 3.544 MeV. Nann *et al.* provides no further information on this state, while the assignment of Bruge and Leonard does not seem likely.

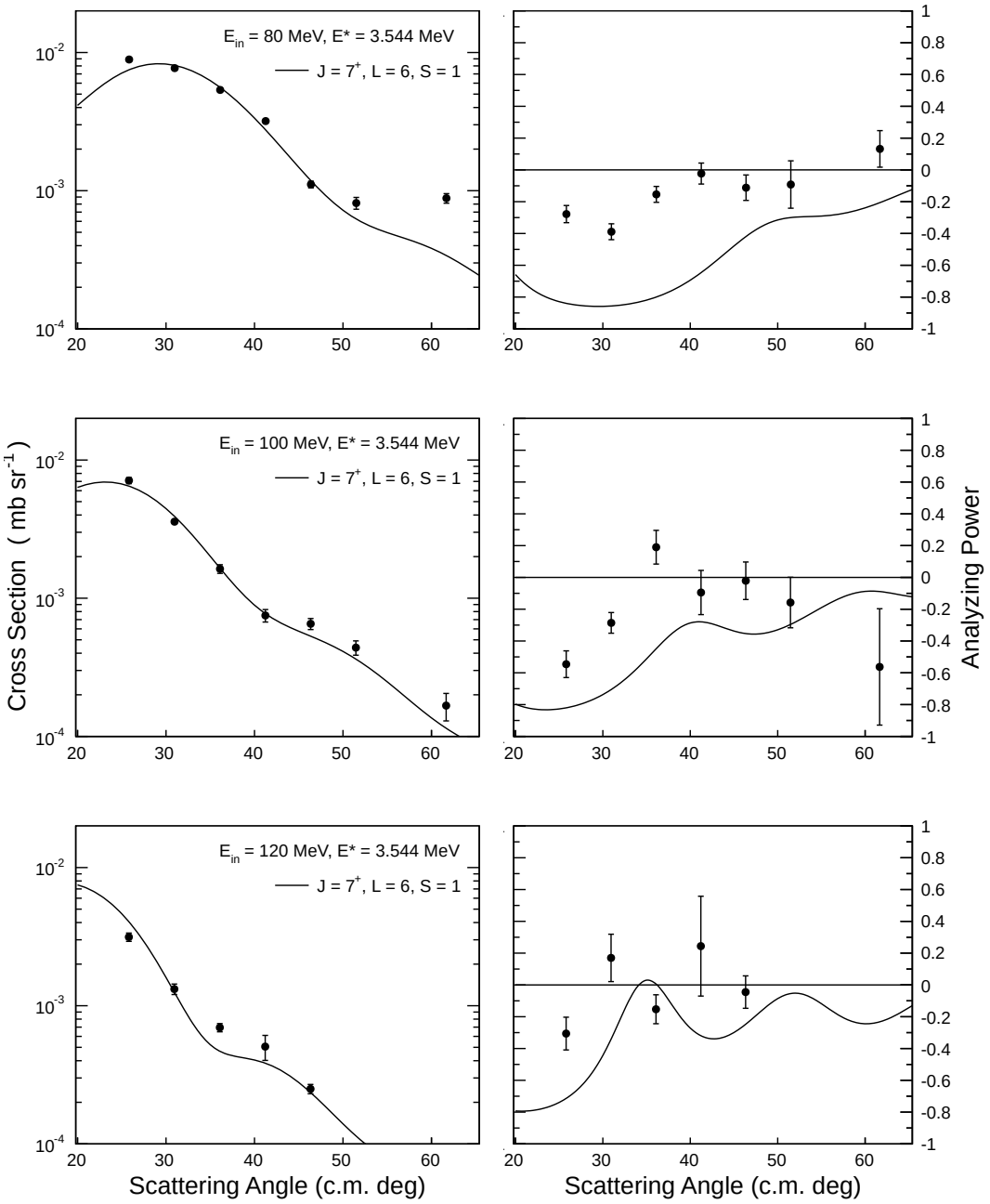

Figure 5.13: Differential cross sections (left) and analyzing powers (right) for the excited state at 3.544 MeV in ^{56}Co. The DWBA calculations are with a $J = 7^+$ spin assignment for 80 MeV (top), 100 MeV (middle) and 120 MeV (bottom) incident energies.

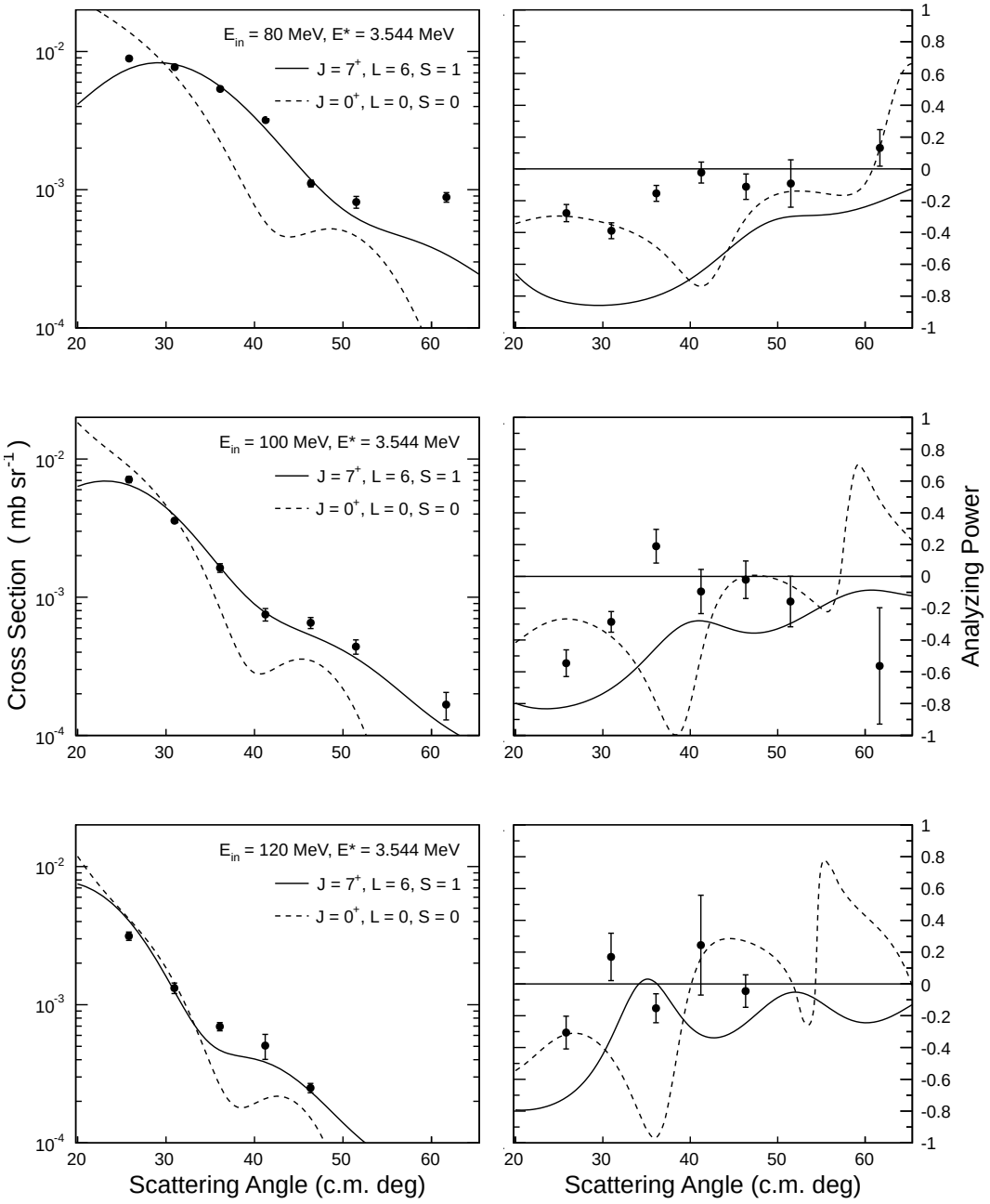

Figure 5.14: Differential cross sections (left) and analyzing powers (right) for the excited state at 3.544 MeV showing DWBA calculations for both a $J = 7^+$ and $J = 0^+$ transfer.

The 5.081 MeV, 5^+ State

The fitting of the data at 5.081 MeV excitation energy may be problematic, again because the limiting energy resolution prevents a clean separation of possibly two contributing states, one at 5.081 MeV and another at 5.146 MeV. Nann *et al.* [Nan81, Nan82] reports a strong $L = 4$ state at 5.146 MeV, but Bruge and Leonard [Bru70] does not. However, the latter authors identified two states at 5.090 and 5.178 MeV considering a $J = 2^+$ assignment. Calculations for the excited state identified at 5.081 MeV are shown in Figure 5.15 for a spin assignment of $J = 3^+$, $L = 2 + 4$, as suggested by [Bru70]. This can be compared to calculations with $J = 5^+$, $L = 4 + 6$, in Figure 5.17, as identified by [Nan82].

The $J = 3^+$ spin assignment gives rather poor cross section fits, with both $L = J \pm 1$ possibilities contributing. The analyzing power angular distributions are represented slightly better, although it appears that A_y at 80 MeV is almost too good to be true. However, by choosing different bound state potential strengths, as discussed in Section 5.1.2, very different results can be achieved. This is demonstrated in Figure 5.16 which is similar to Figure 5.15, but with the spin-orbit potential strength of the bound state adjusted to give a real central strength of $V_d \approx$ -60 MeV. This is about 20 MeV away from the ideally proposed well-matching condition implemented to give the fits in Figure 5.15, that is, $V_d \approx$ -80 MeV. The biggest difference is in the contribution of the $L = 4$ transfer. With this choice of bound state potential the cross section calculations can be made to fit the data much better.

Calculations done for a $J = 5^+$ assignment with $L = 4 + 6$ (Figure 5.17) seem to give slightly better angular distributions, though also rather sensitive to the choice of the bound state spin-orbit potential. The angular distributions of Figure 5.17 were produced with a bound state potential depth of approximately -60 MeV.

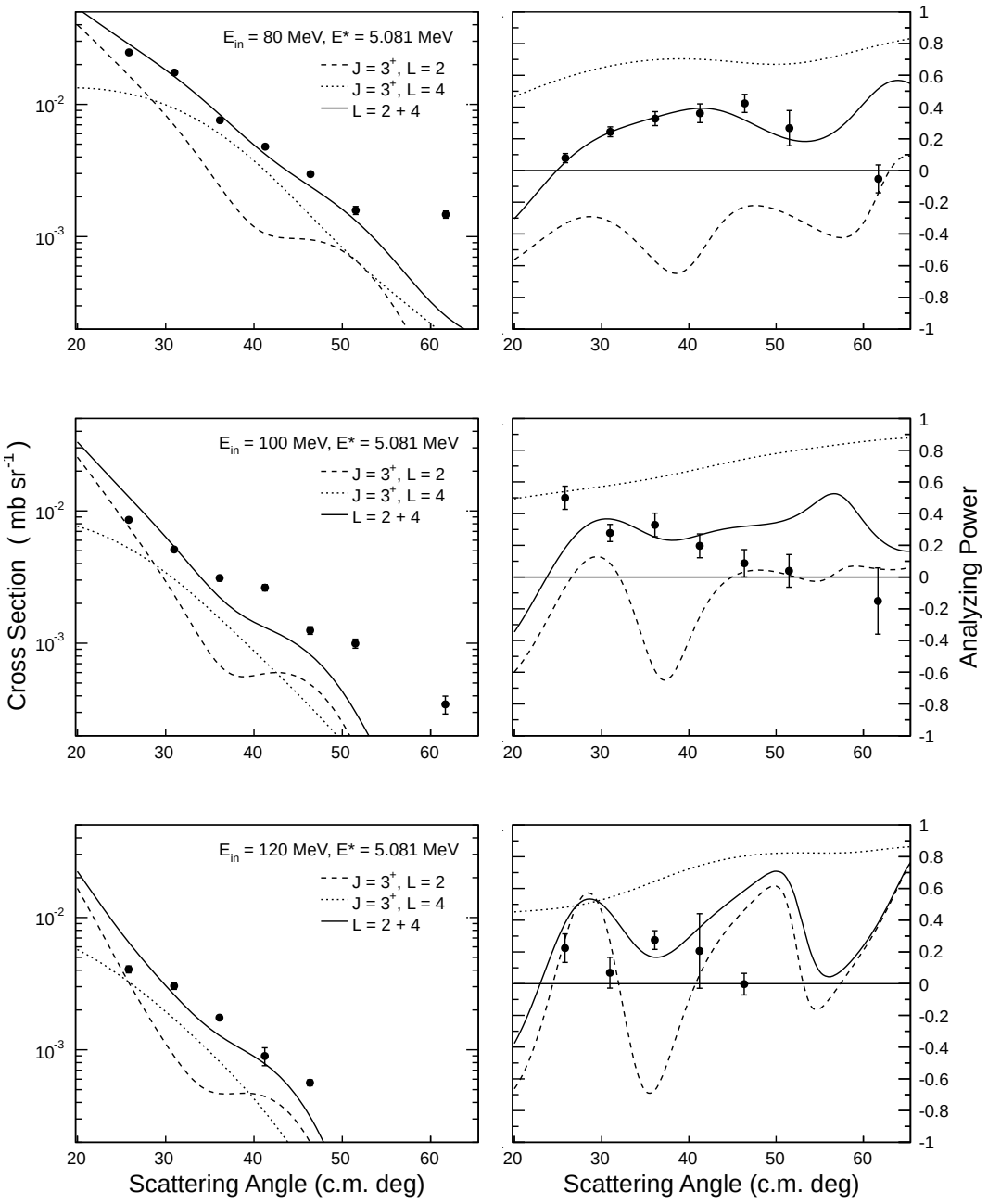

Figure 5.15: Differential cross sections (left) and analyzing powers (right) for the excited state at 5.081 MeV in ^{56}Co. DWBA calculations for the J = 3$^+$, L = 2 + 4 spin assignment are included for 80 MeV (top), 100 MeV (middle) and 120 MeV (bottom) incident energies. The real central potential strength of the bound state, $V_d \approx$ -80 MeV, which satisfies the well-matching condition mentioned in the text.

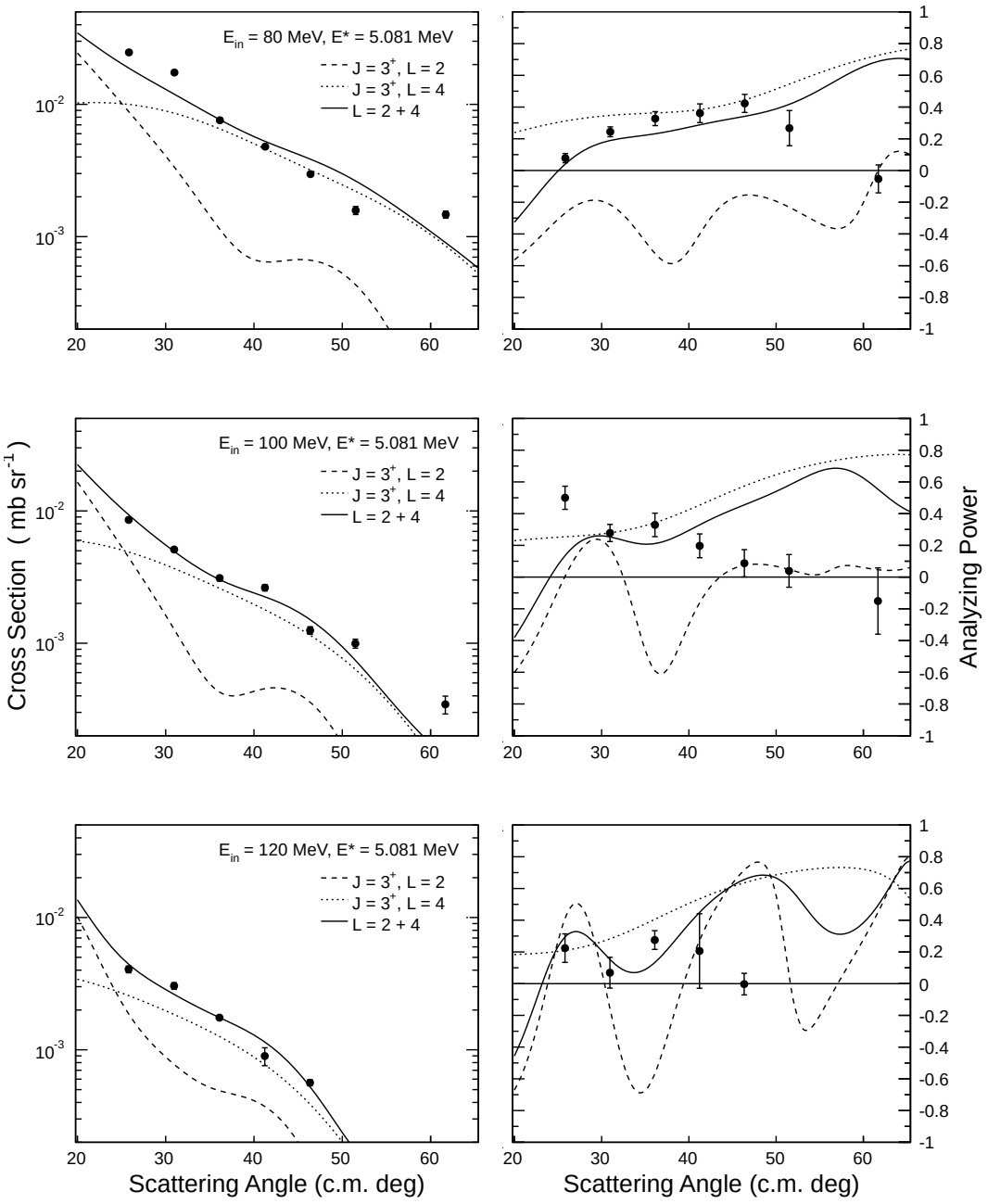

Figure 5.16: Differential cross sections and analyzing powers for the 5.081 MeV excited state with $J = 3^+$, $L = 2 + 4$ spin assignments, similar to Figure 5.15, but with the spin-orbit potential strength of the bound state adjusted to give a real central potential strength of $V_d \approx$ -60 MeV, which is further away from the proper well-matching condition of $V_d \approx$ -80 MeV.

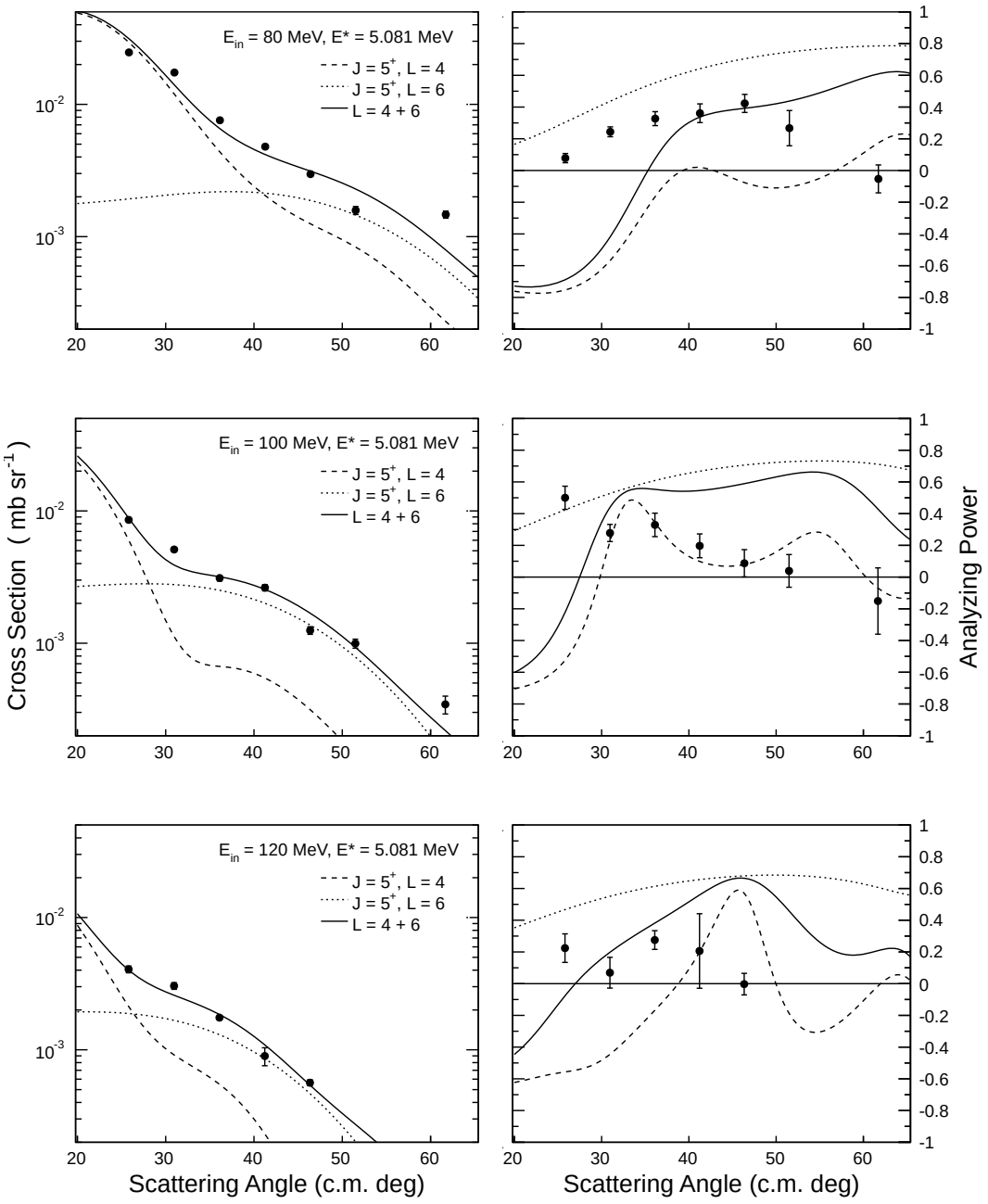

Figure 5.17: Differential cross sections (top) and analyzing powers (bottom) for the excited state at 5.081 MeV in ^{56}Co. DWBA calculations for the $J = 5^+$, $L = 4 + 6$ spin assignment are included for 80 MeV (left), 100 MeV (middle) and 120 MeV (right) incident energies with a bound state potential depth of approximately -60 MeV.

5.3 Incident Energy Dependence

Macroscopic DWUCK calculations for the 2.283 and 3.544 MeV states were made for a 45 MeV incident energy using the optical potential sets of Bruge and Leonard [Bru70], and compared to similar calculations for the 80, 100 and 120 MeV beams in this work. This was done to see how the present results at the higher incident energy compare with the results of studies at a lower 45 MeV.

Results for the different incident energies are shown in Figure 5.18 for the 2.283 MeV state (left panel) and 3.544 MeV state (right panel). Apart from a noteworthy difference in the normalization factors, the present macroscopic calculations for the 45 MeV beam give similar results to the microscopic calculations of Bruge and Leonard. Our present result at 45 MeV finds, for the 2.283 MeV calculations, a normalization factor C of 21.5 between the data and the theory, while Bruge and Leonard quote a factor of 40 to match the magnitude of their data. This difference is probably not very significant.

The 2.283 MeV calculations assumed $J = 7^+$, as did Bruge and Leonard. However, these authors found the peak around 3.544 MeV to be fitted by $J = 0^+$ at the 45 MeV beam energy, and in fact the present study agrees. This is not the case for the higher incident energies. Here calculations done in the present study show better agreement with a $J = 7^+$ choice as can be seen in Figure 5.14. Clearly the unresolved, closely spaced states at 3.544 and 3.599 MeV, with $J = 7^+$ and 0^+ respectively, are being populated with different strengths at the different incident energies, the 7^+ state dominating at the higher 80 - 120 MeV energies, while the 0^+ state at 3.599 MeV is more prominent at lower incident energies.

The calculations seem to show that states with the same spin assignment have similar angular distributions, irrespective of incident energy or excitation energy. For example, the 0^+ state, suggested by Bruge and Leonard, shows a strong oscillatory shape even at the higher incident energies, while the 7^+ calculations do not. This feature is useful for identifying the prominence of states as a function of incident energy.

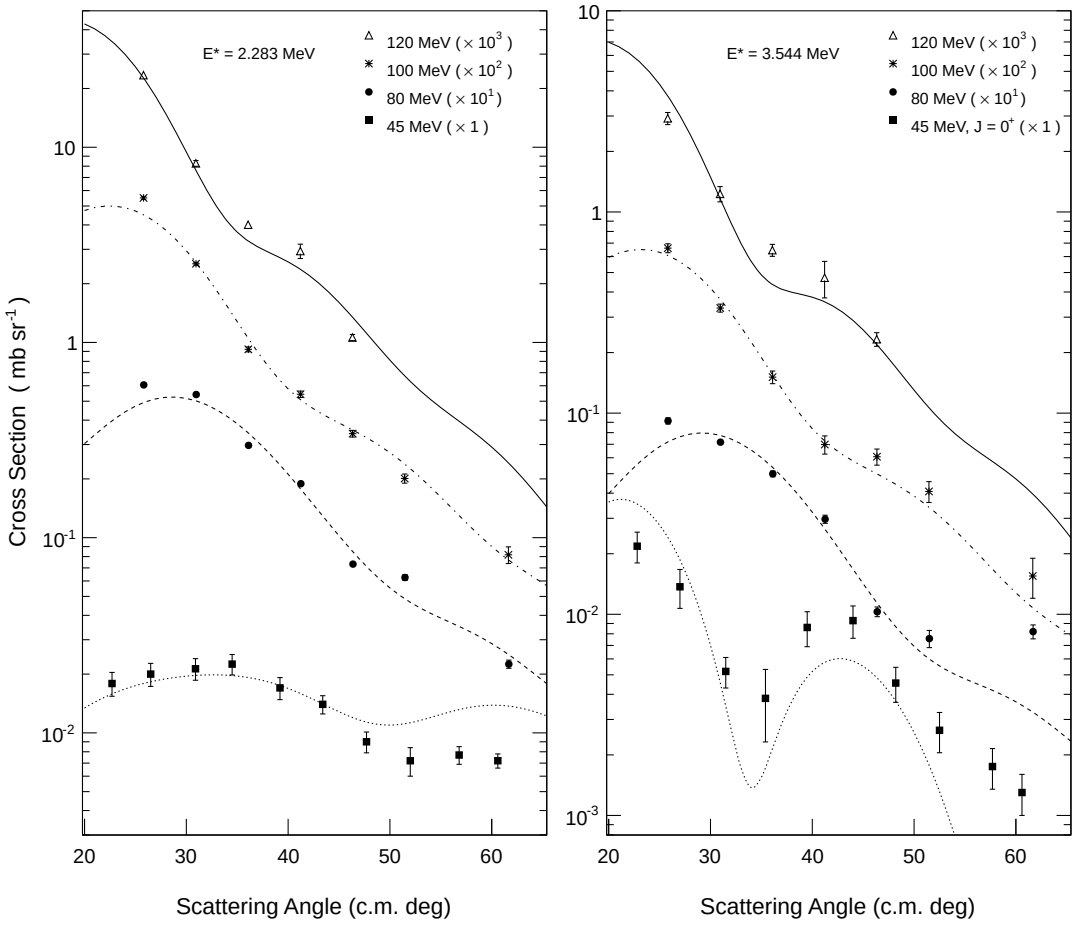

Figure 5.18: Differential cross section calculations for the $J = 7^+$ states at 2.283 MeV (left) and 3.544 MeV (right) at incident energies of 45, 80, 100 and 120 MeV. Data at 45 MeV are from Bruge and Leonard [Bru70], with our macroscopic recalculation. At 45 MeV we assume $J = 7^+$ for the 2.283 MeV state and $J = 0^+$ for the 3.544 MeV state, in accordance with Bruge and Leonard.

The combined differential cross sections and analyzing powers for the five excited states investigated were calculated for each of the incident beam energies. This is displayed in Figure 5.19. The summed angular distributions are clearly dominated by the prominent state at 2.283 MeV. Note that the combined cross section is a simple sum of the cross sections of each state, while the combined analyzing power is the ”weighted” sum of (4.34) or (A.24). It is not immediately obvious whether the analyzing power decreases at increasing incident energies. However, the large absolute values seen at the

forward angles tend to shift further towards even smaller scattering angles, leaving average analyzing power distributions close to zero. This result is consistent with the nature of direct reactions which become more forward peaked as the bombarding energy increases. This does not completely rule out the possibility of fortuitous summation effects of the contributions from different discrete states.

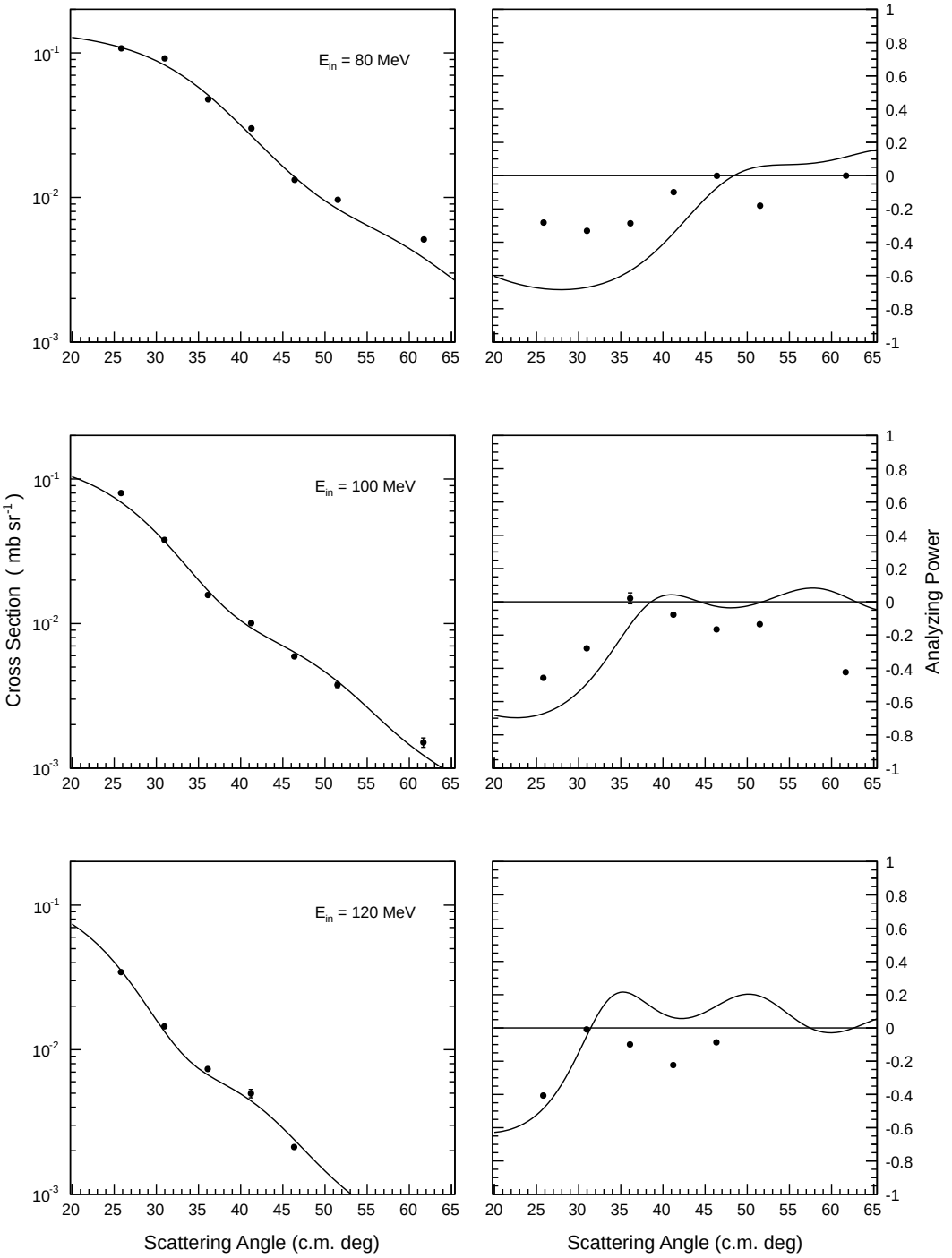

Figure 5.19: Differential cross section and analyzing power angular distributions for a summed combination of the five excited states investigated.

Chapter 6

Final Results

This section summarizes the DWBA calculation results for the measured states of ^{56}Co at 0.577, 1.009, 2.283, 3.544 and 5.081 MeV, and in some cases the ”best guess” spin assignments as has been discussed in Chapter 5. Figure 6.1 presents the differential cross section and analyzing power angular distributions for the 80 MeV incident energy, while the results for the 100 and 120 MeV experiments are presented in Figures 6.2 and 6.3.

The normalization values and the relative contributions of the different L-transfers are listed in Table 6.1. All the cross sections have been normalized based on the prominent state at 2.283 MeV excitation. The overall normalization factors C are 3.58, 6.90 and 6.38 for the three incident energies, 80, 100 and 120 MeV respectively.

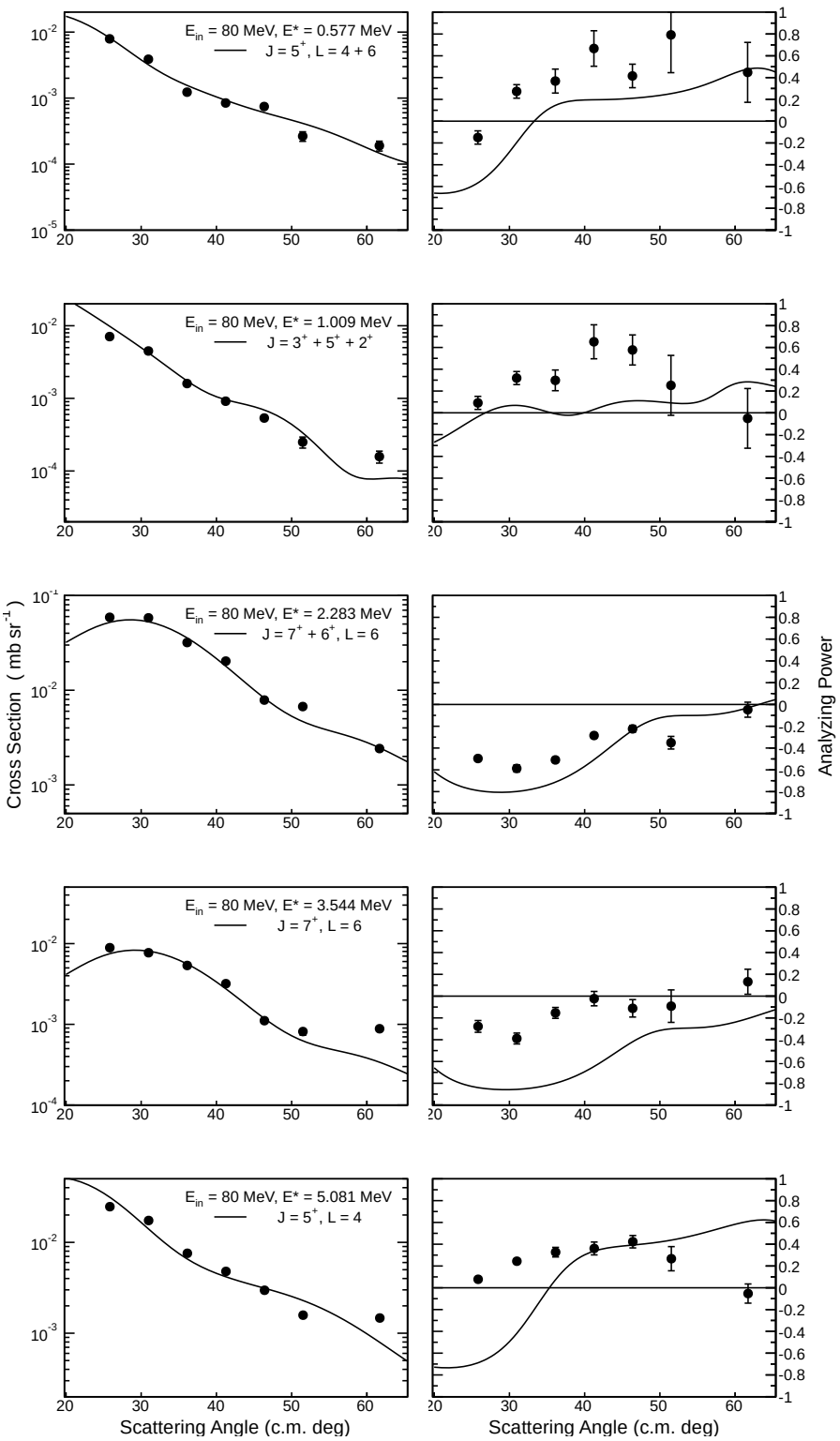

Figure 6.1: Final results for the differential cross section (left) and analyzing power (right) angular distributions for the 80 MeV incident energy experiment. The different excited states are indicated.

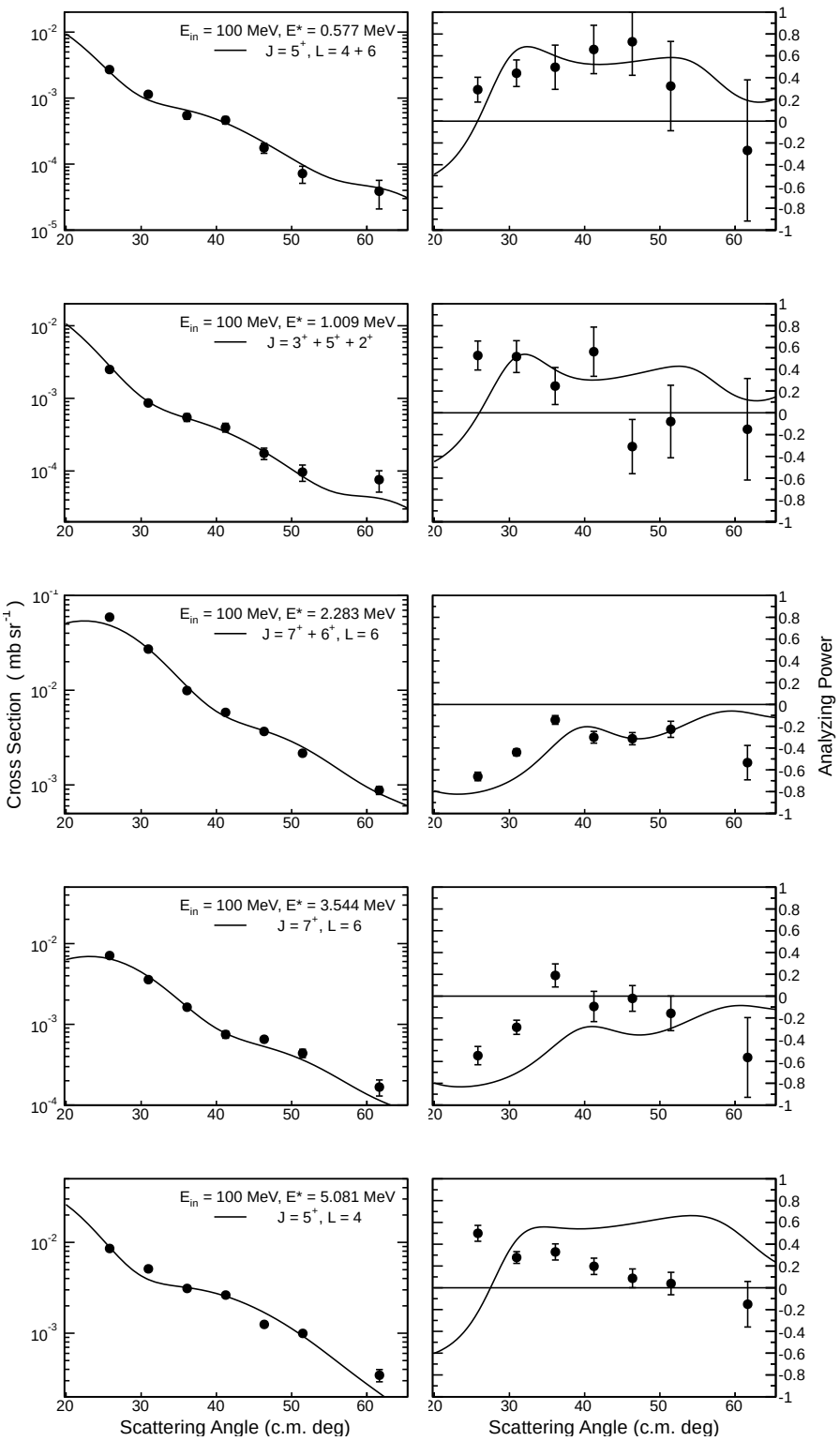

Figure 6.2: Final results for the differential cross section (left) and analyzing power (right) angular distributions for the 100 MeV incident energy experiment. The different excited states are indicated.

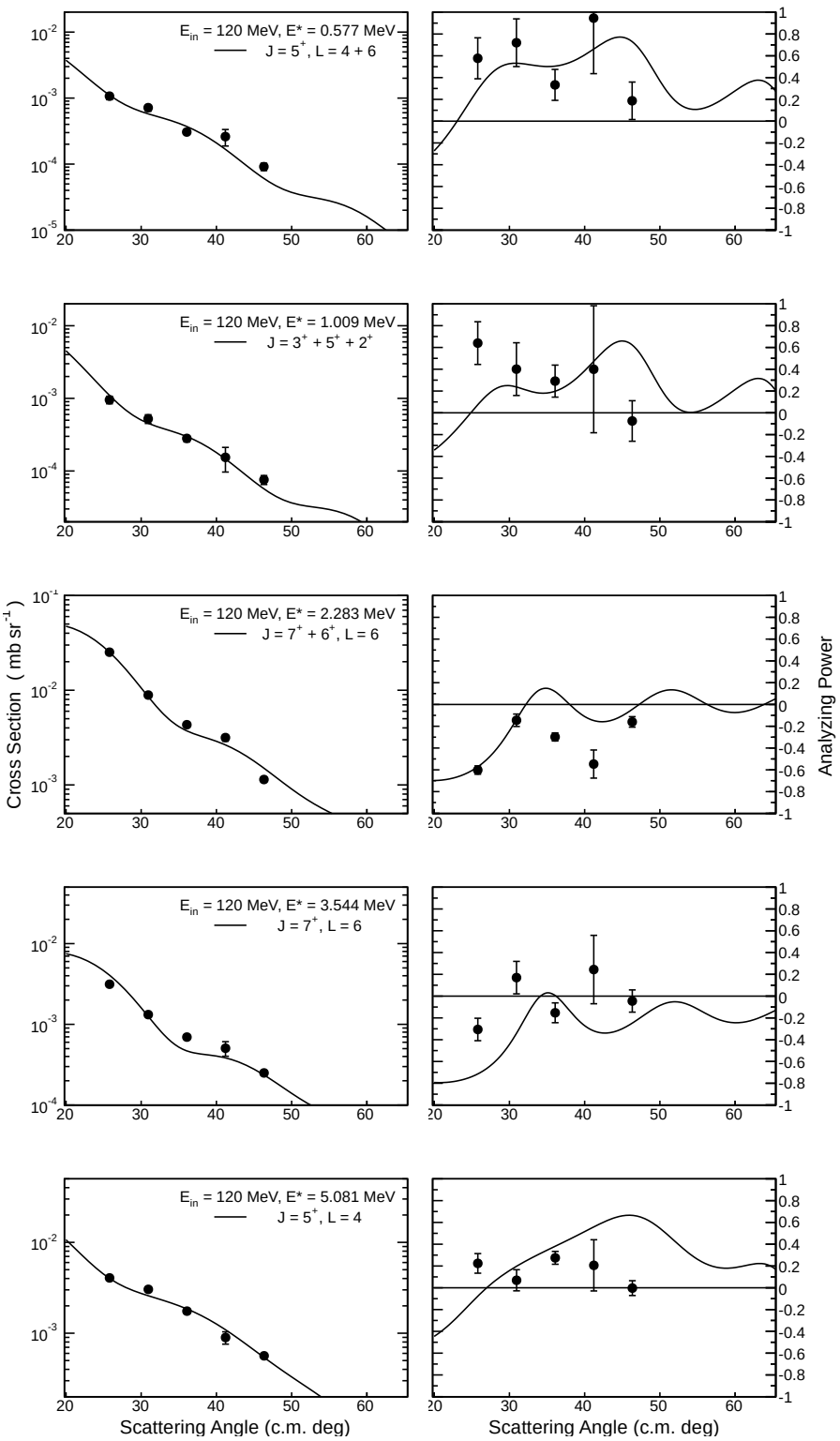

Figure 6.3: Final results for the differential cross section (left) and analyzing power (right) angular distributions for the 120 MeV incident energy experiment. The different excited states are indicated.

Ref. [Fir99]	This work:				80 MeV		100 MeV		120 MeV			Ref.[Bru70]				Ref.[Nan82]			
E^* (MeV)	E^* (MeV)	L	J^π	S	A_L^2	A_{L+2}^2	A_L^2	A_{L+2}^2	A_L^2	A_{L+2}^2		E^* (MeV)	L	J^π		E^* (MeV)	L	J^π	
0.577	0.55 ± 0.04	4 + 6	5^+	1		0.15	0.0	0.11	0.0	0.11	0.0		0.578	4 + 6	5^+		0.58	4	5^+
1.009	0.99 ± 0.04	4 + 6	5^+	1		0.02	0.0	0.11	0.0	0.13	0.0		1.001	2	2^+		1.01	4	5^+
2.283	2.24 ± 0.04	6	7^+	1		=1	-	=1	-	=1	-		2.271	6	7^+		2.28	6	7^+
3.544	3.50 ± 0.04	6	7^+	1		0.14	-	0.12	-	0.16	-		-				3.54	6	7^+
5.081	5.09 ± 0.04	2 + 4	3^+	1		0.16	0.13	0.18	0.04	0.33	0.02		5.090	2 + 4	3^+		-		
5.081	5.09 ± 0.04	4 + 6	5^+	1		0.27	0.04	0.15	0.02	0.14	0.02						-		

Table 6.1: Experimental results for the ^{56}Co levels compared to the references. The relative two-nucleon spectroscopic factors A_L^2 and A_{L+2}^2 are given, normalized to unity for the 2.283 MeV, $J = 7^+$ transition. The overall normalization factors C are 3.58, 6.90 and 6.38 for the 80, 100 and 120 MeV beam energies respectively.

Chapter 7

Summary and Conclusion

Through this study the angular distributions of the differential cross sections and analyzing powers of the ^{58}Ni(p,^{3}He) reaction to a few discrete states in ^{56}Co have been investigated as a function of incident energy between 80 and 120 MeV. The experimental angular distributions have been compared with results from macroscopic, zero-range distorted-wave Born approximation (DWBA) calculations, assuming a simple one-step, direct two-nucleon pickup reaction mechanism. This was done to confirm the validity of the DWBA formalism for the description of the final step in inclusive multistep reaction studies.

The (p,^{3}He) reaction is an ideal probe to study the contributions of states not excited with single particle transfer reactions. The large momentum mismatch for the ^{58}Ni(p,^{3}He) reaction at the relatively high incident energy helps to select predominantly large angular momentum transfers, and especially the observed L = 6 transition stood out as a result of this.

The nucleon-nucleus interactions in the entrance and exit channels were determined from global optical model potentials which give adequate descriptions for the relevant interactions. The bound state wave function was determined from a similar Woods-Saxon type potential with the choice of parameters given by a well-depth procedure. It was found that the resulting cross section and analyzing power angular distributions are quite

sensitive to the choice of optical potential parameters. Not only does the bound state potential affect the angular distributions strongly, but so also does the exact ^{3}He potentials.

Nevertheless, within the uncertainties in the optical potentials mentioned, it is evident that the simple, direct two-nucleon pickup mechanism is quite capable of describing the (p,^{3}He) reaction consistently over the 80 - 120 MeV energy range. Not only is the strong L-dependence of the cross section angular distributions reproduced in the calculations, but also the analyzing power angular distributions can, even with substantial statistical errors, distinguish the dominant transfer where the cross sections are ambivalent. This is a very promising result and confirms that the complex (p,^{3}He) reaction to discrete low lying states can in principle be interpreted by a simple one-step pickup process. This also emphasizes the virtue of including analyzing powers as a spectroscopic tool.

Based on the satisfactory results of the present study it would seem that higher-order processes such as sequential pickup do not contribute significantly to the angular distributions. A much more serious concern would be the prevailing ambiguities in the interacting wave functions of especially the bound state. There also remains some uncertainty about the exact optical potential parameters used for ^{3}He. A first order improvement would be to use a more realistic ^{3}He potential obtained by a *double folding* model as suggested by Hodgson and Běták [Hod03]. Such an approach has been successfully employed in inclusive (p, α) and (p,^{3}He) reaction studies in the past.

The results of the present study strongly support the use of a direct two-nucleon pickup description in terms of the DWBA for the interpretation of continuum multistep reactions.

This work, in conclusion, (i) provides much needed analyzing power angular distributions for medium energy (p,^{3}He) reactions, which will be useful for, amongst many others, evaluation of global optical potentials, (ii) gives confidence that the direct pickup process in the final step of more complex cluster emission reactions should in fact be a valid assumption, and (iii) confirms the sensitivity of the analyzing power as an indicator of the reaction mechanism involved.

Appendix A

Derivations

Appendix A contains a few derivations related to the unpolarized differential cross section, the total cross section and analyzing power, as well as the total statistical errors.

A.1 Derivation of the Analyzing Power and Unpolarized Cross Section

Defining the polarization $\vec{P}$ of the incident beam of spin-1/2 particles as a normalized ensemble average [Hil90], the scattering cross section is written as

$$\sigma(\theta) = \sigma_0(\theta)\left[1 + \vec{P}\cdot\vec{a}\right] \tag{A.1}$$

where $\vec{a}$ is called the asymmetry parameter. If we consider only polarization in the positive ($\uparrow$) or negative ($\downarrow$) $\hat{n}$-direction, as defined in Section 2.2.1, then $\hat{n}\cdot\vec{a} = A_y$ and the above expression becomes

$$\sigma^{\uparrow}(\theta) = \sigma_0(\theta)\left[1 + p^{\uparrow}A_y\right] \tag{A.2}$$

and

$$\sigma^{\downarrow}(\theta) = \sigma_0(\theta)\left[1 - p^{\downarrow}A_y\right] . \tag{A.3}$$

where the $\hat{n}$-component of the asymmetry parameter, A_y, is referred to as the *analyzing power*.

Combining (A.2) and (A.3), we can find an expression for the analyzing power as

$$\frac{\sigma^{\uparrow} - \sigma^{\downarrow}}{\sigma^{\uparrow} + \sigma^{\downarrow}} = \frac{A_y(p^{\uparrow} + p^{\downarrow})}{2 + A_y(p^{\uparrow} - p^{\downarrow})} ,$$

which gives

$$A_y = \frac{\sigma^{\uparrow} - \sigma^{\downarrow}}{\sigma^{\uparrow}p^{\downarrow} + \sigma^{\downarrow}p^{\uparrow}} . \tag{A.4}$$

An expression for the unpolarized cross section σ_0 can be derived in a similar way from (A.2), (A.3) and (A.4)

$$\begin{aligned}\sigma^{\uparrow} + \sigma^{\downarrow} &= \sigma_0\left[2 + A_y(p^{\uparrow} - p^{\downarrow})\right] \\ &= \sigma_0\left[2 + \left(\frac{\sigma^{\uparrow} - \sigma^{\downarrow}}{\sigma^{\uparrow}p^{\downarrow} + \sigma^{\downarrow}p^{\uparrow}}\right)(p^{\uparrow} - p^{\downarrow})\right] ,\end{aligned}$$

which gives

$$\sigma_0 = \frac{\sigma^{\uparrow}p^{\downarrow} + \sigma^{\downarrow}p^{\uparrow}}{p^{\uparrow} + p^{\downarrow}} . \tag{A.5}$$

In the case where $p^{\uparrow} \approx p^{\downarrow} = p$, (A.5) and (A.4) simplifies to

$$\sigma_0(\theta) \approx \frac{\sigma^{\uparrow} + \sigma^{\downarrow}}{2} \tag{A.6}$$

and

$$A_y \approx \frac{1}{p}\frac{(\sigma^{\uparrow} - \sigma^{\downarrow})}{(\sigma^{\uparrow} + \sigma^{\downarrow})} . \tag{A.7}$$

The expression for the cross section in (A.6) is just the familiar sum over the possible spin orientations of particle a, i.e.

$$\frac{d\sigma}{d\Omega} = \frac{1}{(2s_a + 1)}\sum_{s_a}\left(\frac{d\sigma}{d\Omega}\right)_{s_a} . \tag{A.8}$$

A.2 Combined Runs

The total differential cross section $\sigma(\theta)$ for a combination of runs for the same excited state is written as

$$\sigma(\theta) = k\frac{\sum_i N_i B_i}{\sum_i N_0^i} \tag{A.9}$$

where i refers to different experimental runs and B_i represents all the factors that are unique to that particular run, like the target thickness n_i or the target angle θ_i. The different CI range values R_i for each run are contained within N_0^i. The value k includes all the parameters that are common for all the chained runs, like the collimator solid angle $\Delta\Omega$ and some constants. Equation (A.9) serves to indicate the correct method used when *chaining* or combining different runs on the same target.

The combined *unpolarized* cross section in terms of (A.9) is then

$$\sigma_0 = \frac{k\left(\frac{\sum_i N_i^{\uparrow} B_i}{\sum_i N_{0i}^{\uparrow}} \cdot p^{\downarrow} + \frac{\sum_i N_i^{\downarrow} B_i}{\sum_i N_{0i}^{\downarrow}} \cdot p^{\uparrow}\right)}{p^{\uparrow} + p^{\downarrow}}\,. \tag{A.10}$$

As the polarization direction is flipped at regular 10 s intervals during the experiment, the number of incident particles with polarization up is about the same as those with polarization down, differing by at most 0.5%, and so we can make the assumption

$$N_0^{\uparrow} \approx N_0^{\downarrow} = N_0/2\,. \tag{A.11}$$

Using this assumption, the unpolarized cross section becomes

$$\sigma_0(\theta) = 2k\left(\frac{p^{\downarrow}\sum_i N_i^{\uparrow} B_i + p^{\uparrow}\sum_i N_i^{\downarrow} B_i}{N_0(p^{\uparrow} + p^{\downarrow})}\right)\,. \tag{A.12}$$

In more simple cases where the B_i's are common to all the combined runs, Equation (A.12) reduces to

$$\sigma_0(\theta) \approx 2kB\left(\frac{p^{\downarrow}N^{\uparrow} + p^{\uparrow}N^{\downarrow}}{N_0(p^{\uparrow} + p^{\downarrow})}\right)\,. \tag{A.13}$$

In a similar way, the analyzing power A_y of (A.4), written in terms of the format for the cross section as in (A.9), becomes

$$A_y(\theta) = \frac{\frac{\sum_i N_i^{\uparrow} B_i}{\sum_i N_0^{i\uparrow}} - \frac{\sum_i N_i^{\downarrow} B_i}{\sum_i N_0^{i\downarrow}}}{\frac{\sum_i N_i^{\uparrow} p_i^{\downarrow} B_i}{\sum_i N_0^{i\uparrow}} + \frac{\sum_i N_i^{\downarrow} p_i^{\uparrow} B_i}{\sum_i N_0^{i\downarrow}}} \tag{A.14}$$

where the k cancels as a common factor.

The polarization of the beam was generally not measured before or after every single run[1], rather the average value of the polarization measurements during the runs of the same angle was used in the A_y calculations. This, together with (A.11), allows for a further simplification to A_y, namely

$$A_y(\theta) = \frac{\sum_i \left(N_i^{\uparrow} - N_i^{\downarrow} \right) B_i}{\sum_i \left(N_i^{\uparrow} p^{\downarrow} + N_i^{\downarrow} p^{\uparrow} \right) B_i} . \tag{A.15}$$

A.3 Derivation of the Statistical Error

The statistical uncertainties associated with the cross sections and analyzing powers derived above, can be determined from the standard formalism for the propagation of errors [Kno89],

$$\delta_Q^2 = \left(\frac{\partial \sigma}{\partial x_1} \right)^2 \delta_{x_1}^2 + \left(\frac{\partial \sigma}{\partial x_2} \right)^2 \delta_{x_2}^2 + \ldots \tag{A.16}$$

where $x_1, x_2, \ldots$ are the measured variables that contribute independently to the result Q.

The number of incident particles is generally very large, in the order of millions, and so its statistical error is always $< 0.1\%$. We can therefore treat $N_0 = \sum_i N_0^i$ as practically

[1] This is due to time constraints and with that, very low reaction rates at the larger angles.

absolute. We define factors B_i which are different for different individual runs and have a significant error, namely B_{err}.

A.3.1 Cross Section

The cross section of (A.9), where $N_0 = \sum_i N_0^i$, can be written as

$$\sigma(\theta) = k\frac{\sum_i N_i B_i}{N_0}/,, \tag{A.17}$$

where, with this formalism, the measured cross section will have a total uncertainty given by

$$\delta_\sigma = \frac{k}{N_0}\sqrt{\sum_i \left[N_i B_i^2 + (N_i B_{err})^2\right]}\,. \tag{A.18}$$

For runs where the B_i's are common to every run in the chain and only the number of counts differ for different runs of the same state and angle, the error above reduces

$$\delta_\sigma = \sigma\sqrt{\left(\frac{B_{err}^2}{B}\right)^2 + \frac{1}{N}}\,. \tag{A.19}$$

Looking at the exact form of the cross section, equation (3.6), i.e.

$$\frac{d\sigma(\theta)}{d\Omega} = \left(\frac{10^{30} A \cdot q_{e^-}}{\Delta\Omega \cdot N_A \cdot \epsilon}\right)\frac{\sum_i N_i Cos(\theta_i^{tgt})/t_{\rho,i}}{CI_i \cdot R_i}\,, \tag{A.20}$$

we can assign values to k and B_i, where $N_0^i \Rightarrow CI_i \cdot R_i$, namely

- $k \equiv \frac{10^{30} A \cdot q_{e^-}}{\Delta\Omega \cdot N_A \cdot \epsilon}$, and
- $B_i \equiv \frac{Cos(\theta_i^{tgt})}{t_{\rho,i}}$ with error $B_{err}^2 = B_i^2\left[tan^2(\theta_i^{tgt}) \cdot \theta_{err}^2 + \left(\frac{t_{\rho,err}}{t_{\rho,i}}\right)^2\right]$.

A.3.2 Analyzing Power

Similarly, the total error associated with the analyzing power of (A.15), assuming the error in the polarization values have a negligible influence as do B_{err} compared to the effect of the uncertainty in N, is

$$\delta_{A_y} = \frac{1}{\sum_i \left(N_i^{\uparrow} p^{\downarrow} + N_i^{\downarrow} p^{\uparrow}\right) B_i} \times \sqrt{\sum_i (B_i)^2 \left[N_i^{\uparrow} \left(A_y p^{\downarrow} + 1\right)^2 + N_i^{\downarrow} \left(A_y p^{\uparrow} - 1\right)^2\right]} . \quad \text{(A.21)}$$

In cases where B_i is common to all the combined runs, the B_i's cancel and vanishes from (A.21). The reduced form of A_y error is then given by

$$\delta_{A_y} = \frac{\sqrt{N^{\uparrow} \left(A_y p^{\downarrow} + 1\right)^2 + N^{\downarrow} \left(A_y p^{\uparrow} - 1\right)^2}}{\left(N^{\uparrow} p^{\downarrow} + N^{\downarrow} p^{\uparrow}\right)} . \quad \text{(A.22)}$$

A.4 Derivation of the Total Analyzing Power

When different possible L- or S-transfers contribute to a particular excited state, the analyzing powers are summed as follows,

$$(A_y)_{exp} = \frac{\sigma_{tot}^{\uparrow} - \sigma_{tot}^{\downarrow}}{\sigma_{tot}^{\uparrow} + \sigma_{tot}^{\downarrow}} , \quad \text{(A.23)}$$

Thus, writing out the cross sections as sums over different transfers $i = L, S, J$,

$$\begin{aligned}(A_y)_{exp} = \frac{\sum_i \sigma_i^{\uparrow} - \sum_i \sigma_i^{\downarrow}}{\sum_i \sigma_i^{\uparrow} + \sum_i \sigma_i^{\downarrow}} &= \frac{\sum_i \left(\sigma_i^{\uparrow} - \sigma_i^{\downarrow}\right)}{\sum_i \left(\sigma_i^{\uparrow} + \sigma_i^{\downarrow}\right)} \\ &= \frac{\sum_i \frac{\left(\sigma_i^{\uparrow}+\sigma_i^{\downarrow}\right)}{2} \frac{\left(\sigma_i^{\uparrow}-\sigma_i^{\downarrow}\right)}{\left(\sigma_i^{\uparrow}+\sigma_i^{\downarrow}\right)}}{\frac{\left(\sigma_i^{\uparrow}+\sigma_i^{\downarrow}\right)}{2}} \\ &= \frac{\sum_i \sigma_i^{tot} A_y^i}{\sum_i \sigma_i^{tot}} \,. \end{aligned} \tag{A.24}$$

where each A_y^i and σ_i^{tot} is generated by the DWUCK4 code for a specific LSJ.

Appendix B

Clebsch-Gordan Coefficients for Isospin Transfers

This section shows the calculation of the Clebsch-Gordan (CG) coefficients for the isospin transfers in the expression for the theoretical cross section.

The Clebsch-Gordan coefficients in (4.31) for the isospins of the target nucleus T_i, transferred proton-neutron pair T and residual nucleus T_f for a pickup reaction with 3-components T_{iz}, T_z and T_{fz} is written as

$$\langle T_f T_{fz}; T T_z | T_i T_{iz} \rangle \tag{B.1}$$

The 3-component of the isospin of the ^{58}Ni-target nucleus in its ground state with atomic and neutron numbers $Z = 28$ and $N = 30$, can be determined from [Kra88]

$$T_{iz} = \frac{1}{2}(N - Z) = 1 \tag{B.2}$$

and so T_i is taken as 1. The isospin of the transferred proton-neutron pair is either $T = 0$ or 1, depending on the total angular momentum J and spin S as described in Section 4.4.1.

For the case where $T = 0$ and $T_z = 0$, the only non-zero CG coefficient is

$$\langle T_f T_{fz}; T T_z | T_i T_{iz} \rangle^2 = \langle 11; 00 | 11 \rangle^2 = 1 \tag{B.3}$$

When $T = 1$, the possible CG coefficients are

$$\langle 00; 11 | 11 \rangle^2 = 1 \tag{B.4}$$

or

$$\begin{aligned} \langle 22; 1-1 | 11 \rangle^2 &= 3/5 \\ \langle 21; 10 | 11 \rangle^2 &= 3/10 \\ \langle 20; 11 | 11 \rangle^2 &= 1/10 \end{aligned} \tag{B.5}$$

In the calculation of the cross sections, the CG coefficients add incoherently allowing us to combine the coefficients for the cases with $T = 0$ and $T = 1$ separately. The total CG coefficients for $T = 0$ and $T = 1$ is therefore 1 and 2 respectively.

Appendix C

Data Tables

The following tables summarize the experimentally measured differential cross sections ($d\sigma/d\Omega$) and analyzing powers (A_y) for the five states at excitation energies (E^*) of 0.577, 1.009, 2.283, 3.544 and 5.081 MeV, for the three incident beam energies of 80, 100 and 120 MeV, and at scattering angles of 25°, 30°, 35°, 40°, 45°, 50° and 60° (no data at 50° and 60° were obtained for the 120 MeV experiment). The errors quoted are the statistical errors as derived in Section 3.5.3.

C.1 Differential Cross Section and Analyzing Power

Table C.1: Differential cross section and analyzing power angular distribution data for E_{beam} = 80 MeV

E* (MeV)	c.m. angle (deg)	$d\sigma/d\Omega$ (mb sr^{-1})	error	A_y	error
0.577	25.8	7.897×10^{-3}	0.309×10^{-3}	-0.150	0.061
	31.0	3.882×10^{-3}	0.161×10^{-3}	0.273	0.062
	36.1	1.229×10^{-3}	0.084×10^{-3}	0.368	0.110
	41.2	8.430×10^{-4}	0.749×10^{-4}	0.667	0.163
	46.4	7.450×10^{-4}	0.497×10^{-4}	0.415	0.108
	51.5	2.650×10^{-4}	0.437×10^{-4}	0.792	0.347
	61.7	1.900×10^{-4}	0.323×10^{-4}	0.448	0.275
1.009	25.8	7.094×10^{-3}	0.291×10^{-3}	0.091	0.060
	31.0	4.486×10^{-3}	0.173×10^{-3}	0.319	0.060
	36.1	1.598×10^{-3}	0.096×10^{-3}	0.298	0.095
	41.2	9.140×10^{-4}	0.780×10^{-4}	0.652	0.156
	46.4	5.360×10^{-4}	0.420×10^{-4}	0.577	0.138
	51.5	2.500×10^{-4}	0.435×10^{-4}	0.252	0.275
	61.7	1.580×10^{-4}	0.297×10^{-4}	-0.051	0.274
2.283	25.8	5.894×10^{-2}	0.086×10^{-2}	-0.496	0.031
	31.0	5.815×10^{-2}	0.064×10^{-2}	-0.587	0.033
	36.1	3.188×10^{-2}	0.042×10^{-2}	-0.509	0.030
	41.2	2.032×10^{-2}	0.038×10^{-2}	-0.285	0.029
	46.4	7.872×10^{-3}	0.164×10^{-3}	-0.224	0.032
	51.5	6.721×10^{-3}	0.232×10^{-3}	-0.351	0.058
	61.7	2.416×10^{-3}	0.117×10^{-3}	-0.048	0.069
3.544	25.8	8.900×10^{-3}	0.331×10^{-3}	-0.278	0.054
	31.0	7.710×10^{-3}	0.231×10^{-3}	-0.389	0.050
	36.1	5.363×10^{-3}	0.178×10^{-3}	-0.154	0.050
	41.3	3.188×10^{-3}	0.149×10^{-3}	-0.023	0.066
	46.4	1.109×10^{-3}	0.061×10^{-3}	-0.112	0.080
	51.5	8.140×10^{-4}	0.799×10^{-4}	-0.092	0.149
	61.7	8.820×10^{-4}	0.701×10^{-4}	0.132	0.115
5.081	25.8	2.469×10^{-2}	0.054×10^{-2}	0.078	0.029
	31.0	1.745×10^{-2}	0.034×10^{-2}	0.244	0.031
	36.1	7.580×10^{-3}	0.208×10^{-3}	0.327	0.044
	41.3	4.788×10^{-3}	0.180×10^{-3}	0.361	0.059
	46.4	2.972×10^{-3}	0.099×10^{-3}	0.423	0.057
	51.5	1.584×10^{-3}	0.110×10^{-3}	0.267	0.111
	61.7	1.473×10^{-3}	0.091×10^{-3}	-0.053	0.088

Table C.2: Differential cross section and analyzing power angular distribution data for E_{beam} = 100 MeV

E* (MeV)	c.m. angle (deg)	$d\sigma/d\Omega$ (mb sr^{-1})	error	A_y	error
0.577	25.8	2.704×10^{-3}	0.217×10^{-3}	0.289	0.114
	30.9	1.142×10^{-3}	0.092×10^{-3}	0.440	0.122
	36.1	5.470×10^{-4}	0.656×10^{-4}	0.495	0.203
	41.2	4.630×10^{-4}	0.590×10^{-4}	0.658	0.222
	46.3	1.760×10^{-4}	0.303×10^{-4}	0.729	0.308
	51.4	7.200×10^{-5}	2.080×10^{-5}	0.322	0.410
	61.6	3.900×10^{-5}	1.790×10^{-5}	-0.269	0.648
1.009	25.8	2.502×10^{-3}	0.207×10^{-3}	0.526	0.133
	30.9	8.640×10^{-4}	0.796×10^{-4}	0.516	0.146
	36.1	5.470×10^{-4}	0.660×10^{-4}	0.246	0.170
	41.2	3.980×10^{-4}	0.549×10^{-4}	0.561	0.226
	46.3	1.750×10^{-4}	0.313×10^{-4}	-0.310	0.249
	51.4	9.600×10^{-5}	2.440×10^{-5}	-0.080	0.333
	61.6	7.600×10^{-5}	2.480×10^{-5}	-0.151	0.466
2.283	25.8	5.911×10^{-2}	0.105×10^{-2}	-0.661	0.039
	30.9	2.716×10^{-2}	0.045×10^{-2}	-0.439	0.032
	36.1	9.917×10^{-3}	0.281×10^{-3}	-0.142	0.040
	41.2	5.834×10^{-3}	0.219×10^{-3}	-0.301	0.054
	46.3	3.667×10^{-3}	0.144×10^{-3}	-0.314	0.056
	51.5	2.164×10^{-3}	0.116×10^{-3}	-0.228	0.074
	61.6	8.780×10^{-4}	0.861×10^{-4}	-0.534	0.158
3.544	25.8	7.108×10^{-3}	0.364×10^{-3}	-0.546	0.084
	31.0	3.577×10^{-3}	0.164×10^{-3}	-0.286	0.065
	36.1	1.625×10^{-3}	0.117×10^{-3}	0.190	0.106
	41.2	7.500×10^{-4}	0.777×10^{-4}	-0.095	0.139
	46.4	6.530×10^{-4}	0.600×10^{-4}	-0.021	0.118
	51.5	4.390×10^{-4}	0.521×10^{-4}	-0.158	0.159
	61.7	1.670×10^{-4}	0.375×10^{-4}	-0.563	0.366
5.081	25.8	8.557×10^{-3}	0.383×10^{-3}	0.500	0.073
	31.0	5.109×10^{-3}	0.194×10^{-3}	0.278	0.054
	36.1	3.108×10^{-3}	0.158×10^{-3}	0.329	0.074
	41.2	2.629×10^{-3}	0.144×10^{-3}	0.197	0.075
	46.4	1.246×10^{-3}	0.083×10^{-3}	0.087	0.086
	51.5	9.950×10^{-4}	0.780×10^{-4}	0.039	0.103
	61.7	3.450×10^{-4}	0.532×10^{-4}	-0.151	0.209

Table C.3: Differential cross section and analyzing power angular distribution data for E_{beam} = 120 MeV

E* (MeV)	c.m. angle (deg)	$d\sigma/d\Omega$ (mb sr^{-1})	error	A_y	error
0.577	25.8	1.073×10^{-3}	0.123×10^{-3}	0.577	0.188
	30.9	7.160×10^{-4}	0.836×10^{-4}	0.720	0.219
	36.1	3.060×10^{-4}	0.312×10^{-4}	0.333	0.142
	41.2	2.610×10^{-4}	0.732×10^{-4}	0.946	0.510
	46.3	9.100×10^{-5}	1.170×10^{-5}	0.187	0.172
1.009	25.8	9.550×10^{-4}	1.132×10^{-4}	0.640	0.196
	30.9	5.230×10^{-4}	0.719×10^{-4}	0.401	0.242
	36.1	2.810×10^{-4}	0.299×10^{-4}	0.291	0.147
	41.2	1.540×10^{-4}	0.573×10^{-4}	0.400	0.583
	46.3	7.600×10^{-5}	1.070×10^{-5}	-0.075	0.186
2.283	25.8	2.519×10^{-2}	0.062×10^{-2}	-0.602	0.038
	30.9	8.890×10^{-3}	0.300×10^{-3}	-0.145	0.057
	36.1	4.317×10^{-3}	0.119×10^{-3}	-0.298	0.037
	41.2	3.156×10^{-3}	0.267×10^{-3}	-0.547	0.129
	46.3	1.136×10^{-3}	0.042×10^{-3}	-0.160	0.048
3.544	25.8	3.142×10^{-3}	0.217×10^{-3}	-0.306	0.103
	30.9	1.323×10^{-3}	0.115×10^{-3}	0.170	0.149
	36.1	6.950×10^{-4}	0.475×10^{-4}	-0.153	0.091
	41.2	5.060×10^{-4}	1.043×10^{-4}	0.244	0.314
	46.3	2.500×10^{-4}	0.194×10^{-4}	-0.045	0.102
5.081	25.8	4.064×10^{-3}	0.239×10^{-3}	0.224	0.090
	30.9	3.043×10^{-3}	0.175×10^{-3}	0.069	0.097
	36.1	1.748×10^{-3}	0.075×10^{-3}	0.275	0.059
	41.2	8.970×10^{-4}	1.390×10^{-4}	0.206	0.235
	46.3	5.640×10^{-4}	0.291×10^{-4}	-0.003	0.068

Bibliography

[Bar71] H.H. Barschall and W. Haeberli. *Polarisation Phenomena in Nuclear Reactions*. University of Wisconsin Press, Madison, 1971.

[Bel68] T.A. Belote, W.E. Dorenbusch, and J. Rapaport. Excitation of ^{58}Co by Two-Particle Transfer Reactions. *Nuclear Physics*, A109:666–675, 1968.

[Ber77] W. Bertozzi, M.V. Hynes, C.P. Sargent, C. Creswell, P.C. Dunn, A. Hirsch, M. Leitch, B. Norum, F.N. Rad, and T. Sasanuma. Focal Plane Instrumentation: A Very High Resolution MWPC System for Inclined Tracks. *Nuclear Instruments and Methods*, 141:457–476, 1977.

[Bon89] R. Bonetti, F. Crespi, and K.-I. Kubo. The ^{58}Ni(p, α) Reaction Mechanism through a Study of the Analyzing Power. *Nuclear Physics*, A499:381, 1989.

[Bro83] J.D. Brown, W.P. Jones, D.W. Miller, H. Nann, P.M. Lister, F. Khazaie, and J.R. Comfort. Studies of the $(p,^3$He) Reaction on ^{24}Mg and ^{28}Si Initiated by 90-MeV Polarized Protons. Technical report, Indiana University Cyclotron Facility, 1983.

[Bru69] H. Brunnader, J.C Hardy, and Joseph Cerny. ^{34}Ar and $T = 0$ States in ^{34}Cl from Two-Nucleon Pick-up Reactions. *Nuclear Physics*, A137:487–499, 1969.

[Bru70] G. Bruge and R. Leonard. ^{58}Ni$(p,^3$He$)^{56}$Co and $(p, t)^{56}$Ni Reactions at 45 MeV. *Physical Review C*, 2:2200–2217, 1970.

[Car84] T.A. Carey, P.G. Roos, N.S. Chant, A. Nadasen, and H.L. Chen. Alpa Particle Spectroscopic Strengths using the $(p, p\alpha)$ Reaction at 101.5 MeV. *Physical Review C*, 29:1273, 1984.

[Cat05] W.N. Catford. CatKIN ver.2.01, Relativistic Kinematics Spreadsheet, 2005.

[Cok74] W.R. Coker, Takeshi Udagawa, and J.R. Comfort. Successive Pickup Contributions to the ^{98}Mo$(d, \alpha)^{96}$Nb Reaction. *Physical Review C*, 10:1130–1135, 1974.

[Cow96] A.A. Cowley, G.J. Arendse, J.W. Koen, W.A. Richter, J.A. Stander, G.F. Steyn, P.Demetriou, P.E. Hodgson, and Y. Watanabe. Inclusive (p, α) Reactions on ^{27}Al, ^{59}Co, and ^{197}Au at Incident Energies of 120, 160, and 200 MeV. *Physical Review C*, 54:778, 1996.

[Cow97] A.A. Cowley, G.J. Arendse, G.F. Steyn, J.A. Stander, W.A. Richter, S.S. Dimitrova, P. Demetriou, and P.E. Hodgson. Inclusive $(p,^3$He) Reactions on ^{59}Co and ^{197}Au at Incident Energies of 120, 160, and 200 MeV. *Physical Review C*, 5:1843, 1997.

[Cow00] A.A. Cowley, G.F. Steyn, S.S. Dimitrova, P.E. Hodgson, G.J. Arendse, S.V. Förtsch, G.C. Hillhouse, J.J. Lawrie, R. Neveling, W.A. Richter, J.A. Stander, and S.M. Wyngaardt. Multistep Direct Mechanism in the $(\vec{p},^3$He) Inclusive Reaction on ^{59}Co and ^{93}Nb at an Incident Energy of 100 MeV. *Physical Review C*, 62:064605, 2000.

[Cow07a] A.A. Cowley, J. Bezuidenhout, E.Z. Buthelezi, S.S. Dimitrova, S.V. Förtsch, G.C. Hillhouse, P.E. Hodgson, N.M. Jacobs, R. Neveling, F.D. Smit, J.A. Stander, G.F. Steyn, and J.J. van Zyl. Reaction Mechanism for Proton-Induced ^{3}He Emission into the Continuum at Incident Energies between 100 and 200 MeV. In S. Nagamiya, T. Motobayashi, M. Oka, R.S. Hayano, and T. Nagae, editors, *Proceedings of the 23rd International Nuclear Physics Conference INPC2007*, volume 2, page 473. Elsevier, Amsterdam, 2008, 3-8 June 2007.

[Cow07b] A.A. Cowley, J. Bezuidenhout, S.S. Dimitrova, P.E. Hodgson, S.V. Förtsch, G.C. Hillhouse, N.M. Jacobs, R. Neveling, F.D. Smit, J.A. Stander, G.F. Steyn, and J.J. van Zyl. Multistep Direct Mechanism in the (p,^{3}He) Inclusive Reaction on ^{59}Co and ^{93}Nb at Incident Energies between 100 and 160 MeV. *Physical Review C*, 75:054617, 2007.

[Cow10] A.A. Cowley, S.S. Dimitrova, and J.J. van Zyl. Incident-Energy Dependent Quenching of the Analyzing Power in Pre-Equilibrium Composite Particle Emission. In *Proceedings of the 3rd International Conference on Frontiers in Nuclear Structure, Astrophysics, and Reactions - FINUSTAR 3*, 23-27 Aug 2010.

[Cow12] A.A. Cowley, J.J. van Zyl, S.S. Dimitrova, E.V. Zemlyanaya, and K.V. Lukyanov. Mechanism of the ^{93}Nb(p,^{3}He) Inclusive Reaction at an Incident Energy of 160 MeV. *Physical Review C*, 85:054622, 2012.

[Del72] R.M. DelVecchio and W.W. Daehnick. Systematic Distorted-Wave Born-Approximation Predictions for Two-Nucleon Transfers: Applications to (d, α) Experiments. *Physical Review C*, 6:2095–2108, 1972.

[DeM81] R.J. de Meijer, L.W. Put, and J.C. Vermeulen. Two-Nucleon Cluster Spectroscopic Factors: A Search for the Bound-State Parameters. *Physics Letters*, 107B:14–18, 1981.

[DeM82] R.J. de Meijer, L.W. Put, J.J. Akkerman, and J.C. Vermeulen. Microscopic and Macroscopic DWBA Analysis of the Reactions ^{28}Si$(\alpha, d)^{30}$P, $^{32}S(d, \alpha)$ ^{30}P and ^{32}S(α, d) ^{34}Cl Studies at E_α = 50 MeV and E_d = 40 MeV. *Nuclear Physics*, A386:200–244, 1982.

[DeV09] G. de Villiërs. SPEXCIT, iThemba LABS, 2009.

[For91] S.V. Förtsch, A.A. Cowley, J.J. Lawrie, D.M. Whittal, J.V. Filcher, and F.D. Smit. Continuum Protons from Ni(p, p') at Incident Energies between 100 and 200 MeV. *Physical Review C*, 43:691–700, 1991.

[For92] S.V. Förtsch. *Proton Emission in Pre-equilibrium Reactions Induced by Incident Protons of 100 to 200 MeV*. PhD thesis, University of Pretoria, 1992.

[Fen80] Da Hsuan Feng, M.A. Nagarajan, M.R. Strayer, M. Villieres, and W.T. Pinkston. Exact Finite-Range Distorted-Wave Born-Approximation Analyses of the Reactions ^{18}O$(p, t)^{16}$O, ^{48}Ca$(t, p)^{50}$Ca, and ^{90}Zr$(t, p)^{92}$Zr using Realistic Triton and Nuclear Wave Functions. *Physical Review Letters*, 44:1037–1040, 1980.

[Fes80] H. Feshbach, A. Kerman, and S. Koonin. The Statistical Theory of Multi-step Compound and Direct Reactions. *Annals of Physics (NY)*, 125:429, 1980.

[Fir99] R.B. Firestone. Table of Isotopes CD-ROM, 8th Edition, 1999.

[Fis01] K.G. Fissum, W. Bertozzi, J.P. Chen, D. Dale, H.C. Fenker, J. Gao, A. Gavalya, S. Gilad, C.R. Leathers, N. Liyanage, R.O. Michaels, E.A.J.M. Offermann, J. Segal, J.A. Templon, R. Wechsler, B. Wojtsekhowski, and J. Zhao. Vertical Drift Chambers for the Hall A High-resolution Spectrometer at Jefferson Lab. *Nuclear Instruments and Methods in Physics Research A*, 474:108–131, 2001.

[Fou12] D. Fourie, iThemba LABS, South Africa, Private communication, 2012.

[Fuj02] H. Fujita, Y. Fujita, G.P.A. Berg, A.D. Bacher, C.C. Foster, K. Hara, K. Hatanaka, T. Kawabata, T. Noro, H. Sakaguchi, Y. Shimbara, T. Shinada, E.J. Stephenson, H. Ueno, and M. Yosoi. Realization of Matching Conditions for High-resolution Spectrometers. *Nuclear Instruments and Methods in Physics Research A*, 484:1726, 2002.

[Gam80] Y.K. Gambhir. Neutron-Proton Transfer Reactions leading to T = 1 particle-hole States of ^{56}Co. *Pramana*, 14:295–302, 1980.

[Gle65] N. K. Glendenning. Nuclear Spectroscopy with Two-Nucleon Transfer Reactions. *Physical Review*, 137:B102–B113, 1965.

[Gle83] Norman K. Glendenning. *Direct Nuclear Reactions*. Academic Press, 1983.

[Hae74] W. Haeberli. *Nuclear Spectroscopy and Reactions (Part A); Polarisation Experiments; Polarised Beams*. Academic Press, New York, 1974.

[Hal84] M. Haller, W. Kretschmer, R. E. Anderson, B. L. Burks, T. B. Clegg, E. J. Ludwig, R. L. Varner, and J. F. Wilkerson. Investrgation of the Reactions ^{58}Ni$(d,\alpha)^{56}$Co and ^{50}Ti$(d,\alpha)^{48}$Sc with Vector and Tensor Polarized Deuterons. *Nuclear Physics*, A419:45, 1984.

[Har67] J.C. Hardy and I.S. Towner. Effects of a Spin-Dependent Interaction Potential in the DWBA Analysis of Two-Nucleon Transfer Reactions. *Physics Letters*, 25B:98, 1967.

[Hil90] G.C. Hillhouse. Nuclear Reactions with Polarised Spin-1/2 Beams. Master's thesis, Stellenbosch University, 1990.

[Hod03] P.E. Hodgson and E. Běták. Cluster Emission, Transfer and Capture in Nuclear Reactions. *Physics Reports*, 374:1–89, 2003.

[Iga82] Masamichi Igarashi and K.-I. Kubo. Predominance of the Sequential Pickup Mechanism in the ^{208}Pb$(p,t)^{206}$Pb 3^+ Transition. *Physical Review C*, 25:2144–2147, 1982.

[Kno89] G.L. Knoll. *Radiation Detection and Measurement, Second Edition*. John Wiley & Sons, New York, 1989.

[Kon03] A.J. Koning and J.P. Delaroche. Local and Global Nucleon Optical Models from 1 keV to 200 MeV. *Nuclear Physics*, A713:231, 2003.

[Kra88] Kenneth S. Krane. *Introductory Nuclear Physics*. John Wiley & Sons, Inc., 1988.

[Kun81] S. Kunori, Y. Aoki, H. Iida, K. Nagano, Y. Toba, and K. Yagi. Direct Experimental Evidence for Strong, Sequential, Two-Step, Transfer Processes in Allowed (p, t) Reactions. *Physical Review Letters*, 46:810–812, 1981.

[Kun93] P.D. Kunz and E. Rost. *Computational Nuclear Physics 2 - Nuclear Reactions*. Springer-Verslag, New York, 1993.

[Lia09] C-T Liang, X-H Li, and C-H Chai. Global ^{3}He Optical Model Potential Below 270 MeV. *Journal of Physics G: Nucl. Phys.*, 36:085104, 2009.

[Lud90] E.J. Ludwig, C.M. Bhat, T.B. Clegg, E.R. Crosson, H.J. Karwowski, G. Graw, P. Schiemenz, R. Hertenberger, H. Kader, D. Hofer, M. Bisenberger, A.M. Eiro, and F.D. Santos. D-State Parameter Determinations for ^{3}He and ^{4}He. *J. Phys. (Paris)*, Colloque C6:439–442, 1990.

[Mey83] H.O. Meyer, P. Schwandt, W.W. Jacobs, and J.R. Hall. Proton Scattering from ^{12}C between 120 and 200 MeV and the Optical Potential. *Physical Review C*, 27:459, 1983.

[MID09] MIDAS. Data Acquisition System, Paul Sherrer Institute, Switzerland, http://midas.psi.ch, 2009.

[Nan74] H. Nann, W. Benenson, W.A. Lanford, and B.H. Wildenthal. $(p,^3$He) and (p, t) Reactions on ^{29}Si. *Physical Review C*, 10:1001–1012, 1974.

[Nan81] H. Nann, A.D. Bacher, W.W. Jacobs, W.P. Jones, and E.J. Stephenson. High-spin States in ^{56,58}Co with the ^{58,60}Ni$(d, \alpha)^{56,58}$Co Reaction. *Physical Review C*, 24:1984–1991, 1981.

[Nan82] H. Nann, W.W. Jacobs, A.D. Bacher, G. Cravens, W.P. Jones, and E.J. Stephenson. Spin Determinations from the ^{58}Ni$(\vec{d}, \alpha)^{56}$Co Reaction at 80 MeV. *Physics Letters*, 109B:175, 1982.

[Nev01] R. Neveling. *Nuclear Medium effects on Analysing Power Investigated with a Proton Knockout Reaction*. PhD thesis, Stellenbosch University, 2001.

[Nev09] R. Neveling, F.D. Smit, H. Fujita, and R.T. Newman. Guide to the K600 Magnetic Spectrometer, unpublished, 2009.

[Nev11] R. Neveling, H. Fujita, F.D. Smit, T. Adachi, G.P.A. Berg, E.Z. Buthelezi, J. Carter, J.L. Conradie, M. Couder, R.W. Fearick, S.V. Förtsch, D.T. Fourie, Y. Fujita, J. Görres, K. Hatanaka, M. Jingo, A.M. Krumbholz, C.O. Koreba, and J.P. Mira. High Energy-resolution Zero-degree Facility for Light Ion Scattering and Reactions. *Nuclear Instruments and Methods in Physics Research A*, 654:29–39, 2011.

[Pan09] D.Y. Pang, P. Roussel-Chomaz, H. Savajols, R.L. Varner, and R. Wolski. Global Optical Model Potential for A = 3 Projectiles. *Physical Review C*, 79:024615, 2009.

[ROO11] ROOT. Version 5.32/00, http://root.cern.ch, 2011.

[Ros71] E. Rost and P.D. Kunz. Finite-Range Corrections in Two-Nucleon Transfer Reactions. *Nuclear Physics*, A162:376–384, 1971.

[Sar76] D.G. Sarantites, J. Urbon, and Jr. L.L. Rutledge. Transition Rates of High-Spin States in ^{56}Co and ^{56}Fe: Possible Coexistence of Prolate- and Oblate-like Configurations in ^{56}Fe. *Physical Review C*, 14:1412, 1976.

[Sat83] G.R. Satchler. *Direct Nuclear Reactions*. Oxford University Press, 1983.

[Sat90] G.R. Satchler. *Introduction to Nuclear Reactions, 2nd Ed.* Oxford University Press, 1990.

[Sch82] P. Schwandt, H.O. Meyer, W.W. Jacobs, A.D. Bacher, S.E. Vigdor, and M.D. Kaitchuck. Analyzing Power of Proton-nucleus Elastic Scattering between 80 and 180 MeV. *Physical Review C*, 26:55, 1982.

[Sen83] J.C. Sens and R.J. de Meijer. Structure Information on ^{38}K Obtained from a Microscopic and Macroscopic DWBA Analysis of the ^{40}Ca(p,^{3}He)^{38}K Reaction. *Nuclear Physics*, A407:45, 1983.

[Sha84] R. Shang, A.A. Pilt, M.C. Vetterli, A.J. Trudel, and J.A. Kuehner. Energy Levels of ^{56}Co Studied by the ^{58}Ni($\vec{d}, \alpha$)^{56}Co Reaction near 0°. *Nuclear Physics*, A425:411–422, 1984.

[Spa00] K. Spasova, S.S. Dimitrova, and P.E. Hodgson. The Analyzing Powers of (p,^{3}He) Reactions. *Phys. G.*, 26:1489, 2000.

[Sto67] R. Stock, R. Bock, P. David, H.H. Duhm, and T. Tamura. Test of the DWBA in (^{3}He, α) Reactions leading to Configuration and Analogue States. *Nuclear Physics*, A104:136–176, 1967.

[Swa10] J.A. Swartz. A Feasibility Study of the (^{3}He,^{8}He) Reaction with the K600 Magnetic Spectrometer. Master's thesis, Stellenbosch University, 2010.

[Van08] J.J. van Zyl. The Role of a Direct Knock-out Mechanism in the Inclusive (p, α) Reaction. Master's thesis, Stellenbosch University, 2008.

[Woo71] P.B. Woollam and R.J Griffiths. A Comment on the Momentum Mismatch in the ^{144}Sm(τ, α)^{143}Sm Reaction. *Physics Letters*, 37B:13–14, 1971.

[Zie10] J. F. Ziegler, M. D. Ziegler, and J. P. Biersack. SRIM, The Stopping and Range of Ions in Matter, http://www.srim.com, 2010.